Measurement of the Michel Parameter ρ Using the MEGA Positron Spectrometer

Fei-sheng Lee

Dissertation submitted to the Faculty of the

Virginia Polytechnic Institute and State University

in partial fulfillment of the requirements for the degree of

Doctor of Philosophy

in

Physics

Leo Piilonen, Chair

Alexander Abashian

Lay Nam Chang

Kay Kinoshita

John Simonetti

February 20, 2001

Blacksburg, Virginia

Keywords: Muon Decay, Michel Parameter, V-A Theory, Standard Model

Measurement of the Michel Parameter ρ Using MEGA Positron Spectrometer

Fei-sheng Lee

(ABSTRACT)

This experiment attempts to measure the Michel parameter ρ in normal muon decay $\mu^+ \rightarrow e^+\nu_e\bar{\nu}_\mu$ with a precision of 0.001. The Standard Model with pure V-A interaction gives 0.75 for this parameter. The world average value is 0.7518 ± 0.0026. A deviation of the value of ρ from 0.75 will indicate new physics.

The experiment, RHO, was carried out at the Los Alamos Meson Physics Facility (LAMPF) of Los Alamos National Laboratory (LANL) in New Mexico, USA, in 1993. The existing experimental set-up that was built for the MEGA experiment was used for the RHO measurement. The experiment was a collaboration of about 50 physicists from Los Alamos National Laboratory, Stanford University, Fermi National Accelerator Laboratory, Virginia Tech, Texas A&M University, Indiana University, Valparaiso University, University of Houston, University of Chicago and University of Virginia.

The result of the experiment is in agreement with Standard Model. The precision of this measurement was dominated by systematic uncertainties due to the fact that the positron spectrometer used in the measurement was designed for another experiment. Thus, the data analysis here focused mainly on the determination of systematic errors.

Dedication

This dissertation is dedicated to my parents.

Acknowledgments

First I would like to thank my advisor Prof. Leo Piilonen, whose guidance and support made the completion of this dissertation possible. The computing power and the excellent facilities he has provided for this research is incomparable.

I also want to thank Dr. Richard Mischke for the many discussions while I was stationed at Los Alamos National Laboratory from Summer 1996 to Summer 1997. I thank Dr. Martin Cooper of LANL, and I thank Prof. Alexander Abashian of VPI for his encouragement and his interest in this research.

Without Qi's encouragement the outcome of this work would have been very different. Her optimistic views and persistence influenced me far beyond the scope of this dissertation.

It is hard to imagine how one would be able to go through those years without the understanding and belief from friends. I wish the best for my old friends: Dan Mulholland, Dave Stonehouse, Weimin You, Xin Kang, Hendrick Buddenberg, Sven Vogel, Honggou Zhu, Gary Wang, Wayne Wang, E.T.Huang, Captain Kriton, Rob Lockhart, Dave Schmiel, B&B Judge, Jerry Letterman, Xin Qi Li, Julia, Kerstin, Bonnie, Patty, Jen, Amy and many others.

Contents

List of Figures

List of Tables

Chapter 1

Probing New Physics via Normal Muon Decay

1.1 Symmetry and Asymmetry

There is no doubt that in the last few decades of the 20th century **SYMMETRY** has become the most important and fruitful concept in the development of elementary particle physics. The dream of unifying three of the four known fundamental interactions (electromagnetic, strong and weak forces) into one single theory, which was pioneered by Hermann Weyl and Albert Einstein who tried to unify the two long range forces (electromagnetism and gravity), is now being realized in the framework of *gauge theory* in which **gauge symmetry** is believed to be the center of the unification.

Mankind's appreciation of SYMMETRY originated in a simple and intuitive way. Our body is left-right symmetric to a good approximation. Symmetrical objects look balanced and

please our eyes. Ancient civilizations adored SYMMETRY in many different ways and we have seen symmetric patterns that were used for decoration purposes even in prehistoric findings.

The love of SYMMETRY continues until today and intellectuals appreciate it on a deeper level and regard it as one of Nature's basic ingredients. Physicists and mathematicians have extended the idea of symmetry from geometric symmetry to the invariance under *any kind of transformation* performed on an object or a system. Less obvious these symmetries may be, they are equally beautiful to their eyes and their minds. As it turns out, they are not only beautiful, they are powerful tools as well. The power of using these symmetries becomes obvious when complicated situations are encountered. Many times people who had faith in them used them as the torches when they were searching in the dark.

Why are we looking for a unified theory of our Universe? This is a matter of aesthetics. We believe the beauty of the Nature lies in its **SIMPLICITY**. No matter how rich and complex the world may seem to be, the principle that governs it must be **simple**. Everything we see and everything we experience is derived from that mighty first principle. The search for that *theory of everything* has drawn numerous brilliant minds in the past half century.

1.2 From V-A Theory To Standard Model and Beyond

The SYMMETRY this experiment touches upon is left-right symmetry (in the microscopic sense). In 1956 a revolution took place that has profoundly changed our view of Nature. T.D. Lee and C.N. Yang theoretically predicted and C.S. Wu and her co-workers experimentally proved that parity is not conserved in processes involving the weak interaction [**?**] [**?**]. Parity

transformation is in some sense equivalent to left-right transformation in the macroscopic world. They showed that the left-right symmetry, which we took for granted for so long, actually does not hold in processes like nuclear beta decay or normal muon decay, although it is still a good symmetry in the absence of the weak interaction. As a result of this, leptons (e.g. electrons, neutrinos, etc.) emitted in weak decays are always fully polarized along their direction of motion. When created they are always left-handed (spin to the right), while anti-leptons (e.g. positrons, anti-neutrinos, etc) are always created right-handed.

The discovery revealed a surprising feature of Nature and has enriched our picture of SYMMETRIES **and** ASYMMETRIES. Our understanding of weak interaction entered a new era, with the proposal of V-A structure of weak interaction Lagrangian by R.E. Marshak and G.C. Sudarshan [**?**], and also by R. Feynman and M. Gell-Mann [**?**] after the discovery of parity non-conservation.

In the years that followed, the V-A theory served as the theoretical basis in exploring the weak interaction and explaining the related experimental results, until a decade later when it was included in a more general theory: electro-weak theory, or the Standard Model [**?**]. This theory unified weak and electormagnetic interaction on a spontaneously broken $SU(2)_L \times U(1)_Y$ symmetry, and the V-A structure of weak interaction and the masslessness of neutrinos was built into the theory by assigning left-handed fermions to $SU(2)$ doublets and right-handed ones to singlets and requiring lepton number conservation. The theory became so successful that not only the $W_L^{\pm}$ and Z^0 bosons it predicted were found in early 1980's but also all the electroweak processes observed so far have been in agreement with it.

But there are still reasons not to accept the Standard Model as the ultimate theory: it has too many arbitrary parameters (such as mixing angles, masses, coupling constants, etc)

which can not be determined by the theory itself. This is aesthetically in contradiction to the simplicity of an ultimate theory we are seeking for. It leaves the origin of parity violation unanswered, the surprising asymmetry that deserves an explanation in our final picture of the Nature. In addition, the precision of the experiments that agree with the Standard Model has not been sufficient to rule out a deviation from the V-A structure of the weak interaction.

Of all the theories beyond the Standard Model that were proposed to remedy the incompleteness of the Standard Model, we are particularly interested in a model called the **Left-Right Symmetric Model** [**?**]. This is not because the model addresses all of the deficiencies in Standard Model. We chose it because it sets parameters that this experiment can unambiguously measure and set a range. In this model left and right symmetry is restored, but at a higher energy level. The gauge group for this model is $SU(2)_L \times SU(2)_R \times U(1)_{B-L}$, where $B - L$ is the difference between baryon number and lepton number. By including $SU(2)_R$ we will have V+A currents in addition to V-A currents and right-handed gauge boson $W_R{}'s$ in addition to $W_L{}'s$. As the energy is lowered to the levels at which most of the experiments have been carried out, the model reproduces all the features of the $SU(2)_L \times U(1)$ model, and the effects associated with parity asymmetry observed in nature (pure left-handed charged currents, pure left-handed neutrino, etc) are supposed to show up [**?**].

1.3 Normal Muon Decay and Michel Parameterization

This experiment attempts to measure with better precision a fundamental parameter, Michel parameter ρ, that characterizes lepton decays through the weak interaction. The Standard

Model with a pure V-A interaction predicts an exact value for the parameter: 3/4. If the result of the measurement deviates from that prediction, it will be a sign of new physics. A measurement with better accuracy can also be used to set more strict limits on the models beyond the Standard Model, for example, the Left-Right Symmetric Model mentioned in the previous section.

Normal muon decay $\mu^+ \to e^+\nu_e\bar{\nu}_\mu$ provides an excellent way to study weak interactions. It is a clean pure leptonic process which our theory can say much about with great certainty and confidence as opposed to processes such as most hadronic decays that involve the strong interaction.

The Michel parameter ρ this experiment measures is extracted from the energy spectrum of decay positron in $\mu^+ \to e^+\nu_e\bar{\nu}_\mu$. The method used, which will be described in Chapters 4 and 5, takes advantage of the fact that ρ is sensitive to the shape of the spectrum, especially near the high energy end.

The Michel parameter ρ has been measured many times before (see Fig. 1.1). The last measurement, which agrees with the V-A value, was carried out more than 30 years ago [**?**] and has never been improved since.

Normal muon decays (well below $m_{W_L}c^2$) can be described by the most general, local, derivative-free, lepton-number-conserving, four-fermion interaction Hamiltonian [**?**]. While there can be various mathematically equivalent formulations for this interaction, we choose the "helicity projection form" (HPF), in which the fields (μ, e, ν's) have definite handedness [**?**]. The HPF is a convenient way to describe the (charged) weak interaction because we know the latter is dominated by a coupling to **left-handed** fermions. The matrix element

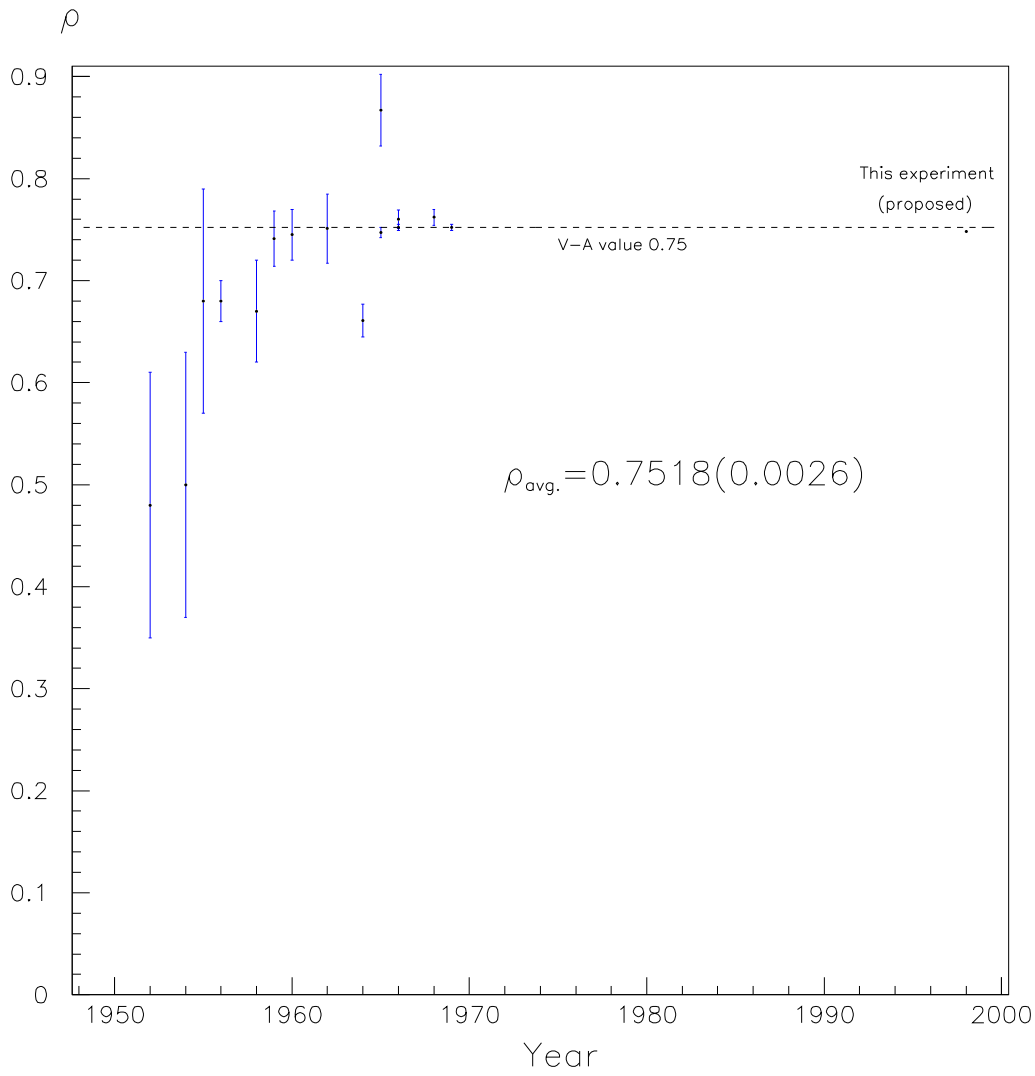

Figure 1.1: A history of the measurement of the Michel parameter ρ

Table 1.1: The chiralities n and m of the ν_e and $\bar{\nu}_\mu$ determined by α, β, and γ.

$\alpha\beta(\gamma)$	nm
LL(S)	RL
(V)	LR
LR(S)	RR
(V)	LL
(T)	RR
RL(S)	LL
(V)	RR
(T)	LL
RR(S)	LR
(V)	RL

for normal muon decays in HPF is [**?**]:

$$M = \frac{4G_F}{\sqrt{2}} \sum_{\substack{\gamma=S,V,T \\ \alpha,\beta=L,R \\ (m,n)}} g^{\gamma}_{\alpha\beta} < \bar{e}_\alpha \mid \Gamma^\alpha \mid (\nu_e)_n >< (\bar{\nu}_\mu)_m \mid \Gamma_\alpha \mid \mu_\beta > \tag{1.1}$$

Here $g^{\gamma}_{\alpha\beta}$'s are the (complex) coupling constants, $\gamma = S, V, T$ stands for a scalar, vector, or tensor interaction; $\alpha, \beta = L, R$ indicate a left- or right-handed chirality of the muon or electron, n and m are the chiralities of the ν_e and $\bar{\nu}_\mu$ and are determined by the values of γ, α and β (Table 1.1). There are 12 combinations for $g^{\gamma}_{\alpha\beta}$, of which two (g^T_{LL} and g^T_{RR}) equal zero. For the remaining 10 complex $g^{\gamma}_{\alpha\beta}$'s, there are 20 real parameters, but since there is an arbitrary common phase and a scale factor, only 18 real parameters are measurable.

Table 1.2: 90% CL experimental constraints on the coupling constants $g^{\gamma}_{\alpha\beta}$ [**?**], except for $|g^{T}_{LL}| = 0$ and $|g^{T}_{RR}| = 0$, which are implied by the theory.

$\|g^{S}_{LL}\| < 0.55$	$\|\mathbf{g^{V}_{LL}}\| > \mathbf{0.96}$	$\|\mathbf{g^{T}_{LL}}\| \equiv \mathbf{0}$
$\|g^{S}_{LR}\| < 0.125$	$\|g^{V}_{LR}\| < 0.060$	$\|g^{T}_{LR}\| < 0.036$
$\|g^{S}_{RL}\| < 0.424$	$\|g^{V}_{RL}\| < 0.110$	$\|g^{T}_{RL}\| < 0.122$
$\|g^{S}_{RR}\| < 0.066$	$\|g^{V}_{RR}\| < 0.033$	$\|\mathbf{g^{T}_{RR}}\| \equiv \mathbf{0}$

Adding the Fermi coupling constant G_F, there are a total of 19 free real parameters in this form of the Hamiltonian. All 19 parameters are determined by muon experiments: G_F is determined by the muon life-time measurement, 16 by other muon-decay measurements, and 2 by inverse muon decay [**?**]. The constraints on the 12 $g^{\gamma}_{\alpha\beta}$'s are shown in Table 1.2. For a **pure V-A** leptonic charged weak interaction, $\mathbf{g^{V}_{LL}} \equiv \mathbf{1}$, and all other $g^{\gamma}_{\alpha\beta}$'s are equal to zero. This experiment looks for possible deviation from V-A structure and therefore helps to set a new lower limit for g^{V}_{LL} and upper limit for the other $g^{\gamma}_{\alpha\beta}$'s.

From the matrix element shown above, the differential decay rate (or positron spectrum) in the rest frame of a polarized muon can be derived as:

$$\frac{d^2\Gamma}{dx d(\cos\theta)} \propto x\sqrt{x^2 - x_o^2}\Big\{6(1-x) + \frac{4}{3}\rho(4x - 3 - \frac{x_o^2}{x}) + 6\eta x_o\frac{1-x}{x} \pm \beta P_\mu \xi \cos\theta\Big[2(1-x) + \frac{4}{3}\delta\Big(4x - 3 - x' x_o\Big)\Big]\Big\}, \tag{1.2}$$

where

$x = E_{e^+}/E_{max}$,

$x_o = m_{e^+}/E_{max}$,

E_{e^+} is the positron energy,

E_{max} is the maximum positron energy ($= (m_\mu^2 + m_{e^+}^2)/2m_\mu = 52.83$ MeV),

m_{e^+} is the positron rest mass (0.511 MeV),

m_μ is the muon rest mass (105.66 MeV),

$\beta = p/E_{e^+}$,

p is the positron momentum,

P_μ is the muon polarization,

θ is the angle between positron momentum and muon polarization,

ρ, η, ξ and δ are decay parameters in the Michel parameterization,or generally, Michel parameters. They are expressed in terms of $g_{\alpha\beta}^{\gamma}$'s as follows [**?**]:

$$\rho = (3b + 6c)/A,$$

$$\eta = (\alpha - 2\beta)/A,$$

$$\xi = (-3a' - 4b' + 14c')/A,$$

$$\delta = (3b' - 6c')/A.$$

where

$A = a + 4b + 6c$,

$a = 16(|g_{RL}^V|^2 + |g_{LR}^V|^2) + |g_{RL}^S + g_{RL}^T|^2 + |g_{LR}^S + g_{LR}^T|^2$,

$b = 4(|g_{RR}^V|^2 + |g_{LL}^V|^2) + |g_{RR}^S|^2 + |g_{RR}^T|^2$,

$c = \frac{1}{2}\left[|g_{RL}^S - 2g_{RL}^T|^2 + |g_{LR}^S - 2g_{LR}^T|^2\right]$,

$a' = 16(|g_{RL}^V|^2 - |g_{LR}^V|^2) + |g_{RL}^S + g_{RL}^T|^2 - |g_{LR}^S + g_{LR}^T|^2$,

$b' = 4(|g_{RR}^V|^2 - |g_{LL}^V|^2) + |g_{RR}^S|^2 - |g_{RR}^T|^2$,

$c' = \frac{1}{2}\left[|g_{RL}^S - 2g_{RL}^T|^2 - |g_{LR}^S - 2g_{LR}^T|^2\right]$,

$\alpha = 8Re\left[g_{RL}^V(g_{LR}^S + 6g_{LR}^T)^* + g_{LR}^V(g_{RL}^S + 6g_{RL}^T)^*\right]$,

$\beta = -4Re\left[g_{RR}^V(g_{LL}^S)^* + g_{LL}^V(g_{RR}^S)^*\right]$,

$\alpha' = 8Im\left[-g_{LR}^V(g_{RL}^S + 6g_{RL}^T)^* - g_{RL}^V(g_{LR}^S + 6g_{LR}^T)^*\right]$,

$\beta' = 4Im\left[g_{RR}^{V}(g_{LL}^{S})^{*} - g_{LL}^{V}(g_{RR}^{S})^{*}\right]$.

The pure V-A structure ($g_{LL}^{V} = 1$, all others zero) prediction of the decay process gives:

$$b = 4,$$

$$b' = -4,$$

$$a = a' = c = c' = \alpha = \alpha^{'} = \beta = \beta^{'} = 0,$$

$$A = 16,$$

and therefore

$$\rho = 3/4,$$

$$\eta = 0,$$

$$\xi = 1,$$

$$\delta = 3/4.$$

If the positron rest mass energy (0.511 MeV) is neglected as compared with its maximum energy (52.8 MeV), and β in Equation (1.2) is approximated as 1, the decay rate simplifies to:

$$\frac{d^2\Gamma}{dxd(\cos\theta)} \propto x^2\left\{6(1-x) + \frac{4}{3}\rho(4x-3) \pm P_\mu\xi\cos\theta\left[2(1-x) + \frac{4}{3}\delta(4x-3)\right]\right\} \qquad (1.3)$$

Radiative corrections should be considered here when comparing the theory with experimental results. They come from the interactions of charged particles (μ^+ or e^+) with the electromagnetic field. See Fig 1.2.

By including the radiative corrections of order α (the fine structure constant) for pure V-A interaction we obtain the radiation corrected differential decay rate:

$$\frac{d^2\Gamma}{dxd(\cos\theta)} \propto x^2\left\{\left[6(1-x)+\frac{4}{3}\rho(4x-3)\right]r_1(x) \pm P_\mu\xi\cos\theta\left[2(1-x)+\frac{4}{3}\delta(4x-3)\right]r_2(x)\right\} \quad (1.4)$$

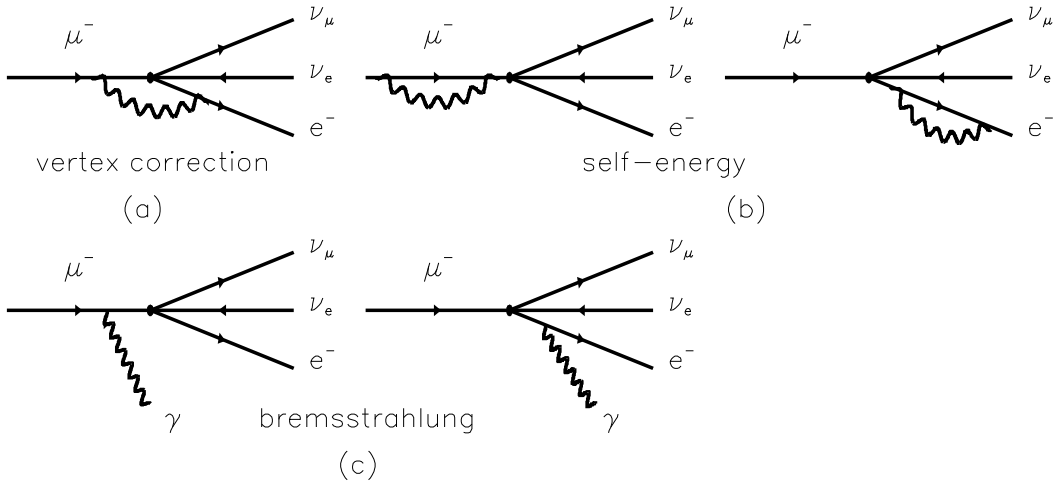

Figure 1.2: Radiative corrections for $\mu^+ \to e^+\nu_e\bar{\nu}_\mu$

where

$$r_1(x) = 1 + \frac{\frac{\alpha}{2\pi}f(x)}{3-2x} + \frac{1}{2}\left[\frac{\frac{\alpha}{2\pi}f(x)}{3-2x}\right]^2 \tag{1.5}$$

$$r_2(x) = 1 + \frac{\frac{\alpha}{2\pi}g(x)}{2x-1} + \frac{1}{2}\left[\frac{\frac{\alpha}{2\pi}g(x)}{2x-1}\right]^2. \tag{1.6}$$

Here,

$$f(x) = 2(3-2x)R(x) + 6(1-x)\ln x + \frac{1-x}{3x^2} \times \left[(5+17x-34x^2)(\omega+\ln x) - 22x + 34x^2\right] \tag{1.7}$$

$$g(x) = 2(1-2x)R(x) + 2(1-3x)\ln x - \frac{1-x}{3x^2} \times \left[(1+x+34x^2)(\omega+\ln x) + 3 - 7x - 32x^2 + \frac{4(1-x)^2}{x}\ln(1-x)\right] \tag{1.8}$$

$$R(x) = 2\sum_{n=1}^{\infty}\frac{x^n}{n^2} - \frac{\pi^2}{3} - 2 + \omega\left[\frac{3}{2} + 2\ln\left(\frac{1-x}{x}\right)\right] - (2\ln x - 1)\ln x + \left(3\ln x - 1 - \frac{1}{x}\right)\ln(1-x) \tag{1.9}$$

where ω=ln(m_μ/m_e).

Among the Michel parameters, ρ and η are shape parameters that describe the high and low energy end of positron spectrum respectively and ξ is the angular asymmetry parameter in polarized muon decay. Fig. 1.3 shows how different values of ρ correspond to different shapes (and heights) near the end point of the positron energy spectrum. With $\rho = 3/4$, the tangent at the end point is horizontal. Also, there is a magic point at $x = 0.75$, or a positron energy of 39.6 MeV, where all spectra intersect each other.

We know that the local interaction given by Equation (1.1), and therefore the differential decay rate in Equation (1.2), and Equation (1.4), are the low energy approximation of the more general electro-weak theory. In this limit the intermediate gauge boson W_L propagation is reduced to a contact interaction. In the Standard Model, the differential decay rate and parameter ρ have the following forms:

$$\begin{aligned}\frac{d^2\Gamma}{dxd(\cos\theta)} \propto x^2\Big\{3-2x-\frac{1}{5}(\frac{m_\mu}{m_{W_L}})^2(9-16x+5x^2) \\ \pm P_\mu\cos\theta\Big[1+\frac{3}{5}(\frac{m_\mu}{m_{W_L}}^2)\Big]\Big[2x-1+\frac{1}{5}(\frac{m_\mu}{m_{W_L}})^2(6-12x+5x^2)\Big]\Big\}.\end{aligned} \tag{1.10}$$

and

$$\rho_{SM} = \frac{3}{4}+\frac{1}{3}(\frac{m_\mu}{m_{W_L}})^2 \tag{1.11}$$

The modification due to the inclusion of heavy W_L bosons is of the order $(\frac{m_\mu}{m_{W_L}})^2$. Here m_{W_L} is the mass of W_L boson and is $\sim$ 80 GeV/c^2. For ρ, this correction is 7.7×10^{-7}. The present experimental precision is no better than 10^{-4}, so this correction is negligible.

Neglecting the terms with $(\frac{m_\mu}{m_{W_L}})^2$, Equation (1.10) becomes:

$$\frac{d^2\Gamma}{dxd(\cos\theta)} \propto x^2\Big[3-2x\pm P_\mu\cos\theta(2x-1)\Big], \tag{1.12}$$

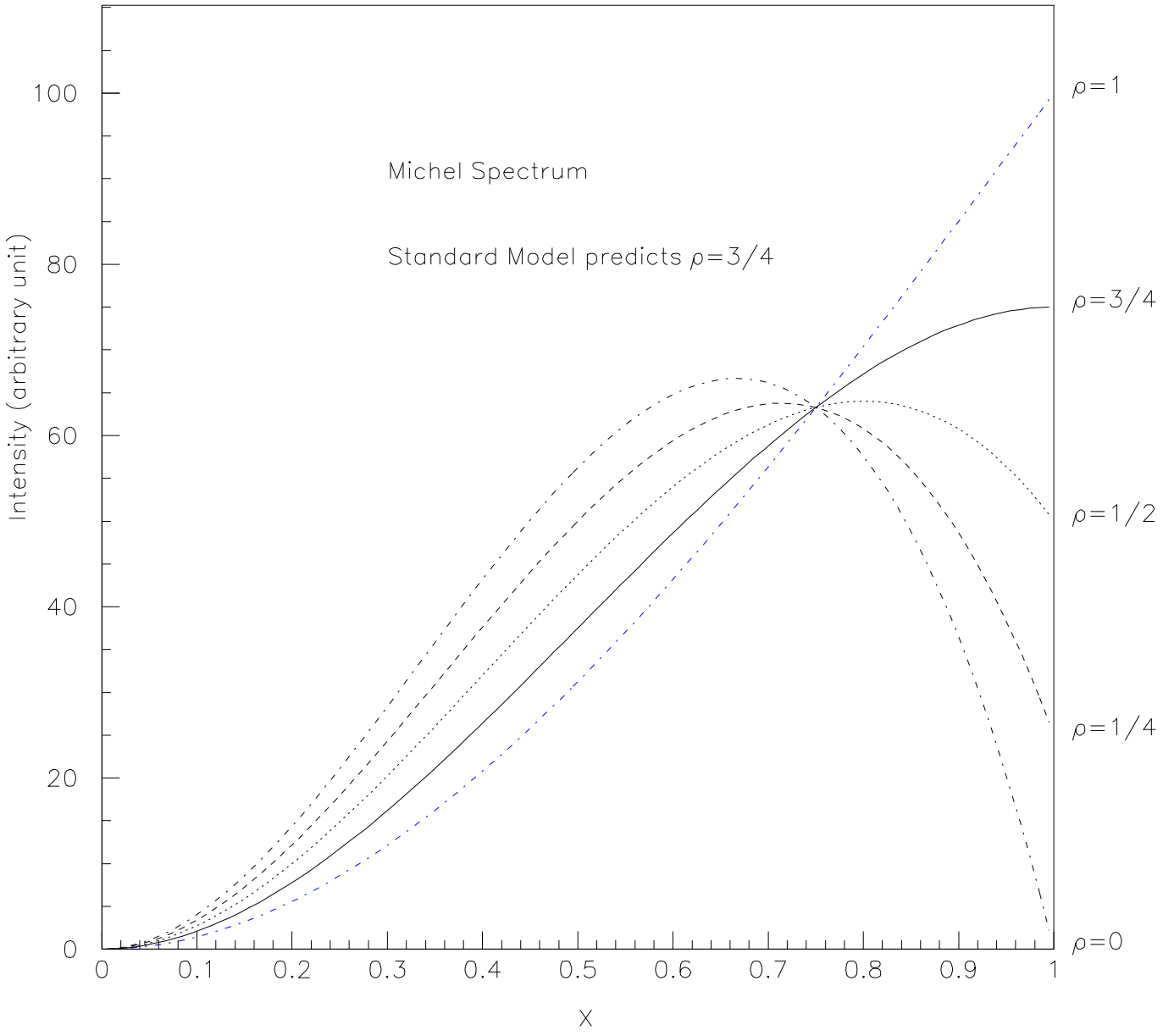

Figure 1.3: Michel spectrum for different values of ρ in the decay $\mu^+ \to e^+\nu_e\bar{\nu}_\mu$

which implies the Michel parameters have the values shown previously.

1.4 A Search for the Right-Handed W Boson W_R

The deviation of the Michel parameter ρ from its Standard Model (with a pure V-A interaction) value of 3/4 is a signal of new physics. It may indicate that the charged weak current is not pure V-A but can have a small fraction of V+A. This corresponds to the existence of right-handed W_R's. The deviation of ρ from 3/4 sets a lower limit on the mass of W_R's, and for this we take as an example the left-right symmetric model mentioned in the section 1.2, or more specifically, the manifest left-right symmetrical model (MLRSM). Here by manifest left-right symmetric we mean that the physical left-handed and right-handed currents have identical transformation properties in flavor space [**?**]. The relevant part of the interaction is

$$L = (g/\sqrt{8}\,[(V-A)_\rho W_L^\rho + (V+A)_\rho W_R^\rho + H.c.] \tag{1.13}$$

Here W_L and W_R are positively charged left-handed and right-handed fields, and they are presumed to derive their masses from the Higgs mechanism. In general there is a mixing between the mass eigenstates $W_{1,2}$ and the chirality eigenstates $W_{L,R}$:

$$W_1 = W_L \cos\zeta - W_R \sin\zeta,$$

$$W_2 = W_L \sin\zeta + W_R \cos\zeta.$$

where ζ is the mixing angle. The Michel parameter ρ, expressed in terms of the two parameters in this model, is:

$$\rho = \frac{3}{4}\Big[1 - \frac{(\epsilon-1)^2}{2(\epsilon^2+1)}\sin^2(2\zeta)\Big]. \tag{1.14}$$

where $\epsilon = m^2(W_1)/m^2(W_2)$ is the ratio of mass squared of W_1 and W_2. Pure V-A corresponds to $\zeta \to 0$, $m_{W_R} \to \infty$ and $\epsilon \to 0$. The deviation from V-A can therefore be translated into a

lower limit on m_{W_R}. The most severe limits on ϵ and ζ have come from the measurement of the Michel parameter ρ in muon decay and the measurement of electron polarization in O^{14} decay [**?**]. The limits set by the best measurements so far in these two experiments are:

$$\sqrt{\epsilon} \leq 0.35,$$

$$\tan\zeta < 0.05.$$

This corresponds to [**?**] $m_{W_R} \geq 200$ GeV/c^2.

Recently there have been interests in measuring ρ in τ decays. Because of the limited statistics, the error on ρ from these experiments is still large. The results from OPAL [**?**], ARGUS Collaboration [**?**], SLD Collaboration [**?**] and CLEO Collaboration [**?**] are shown in Fig. 1.4.

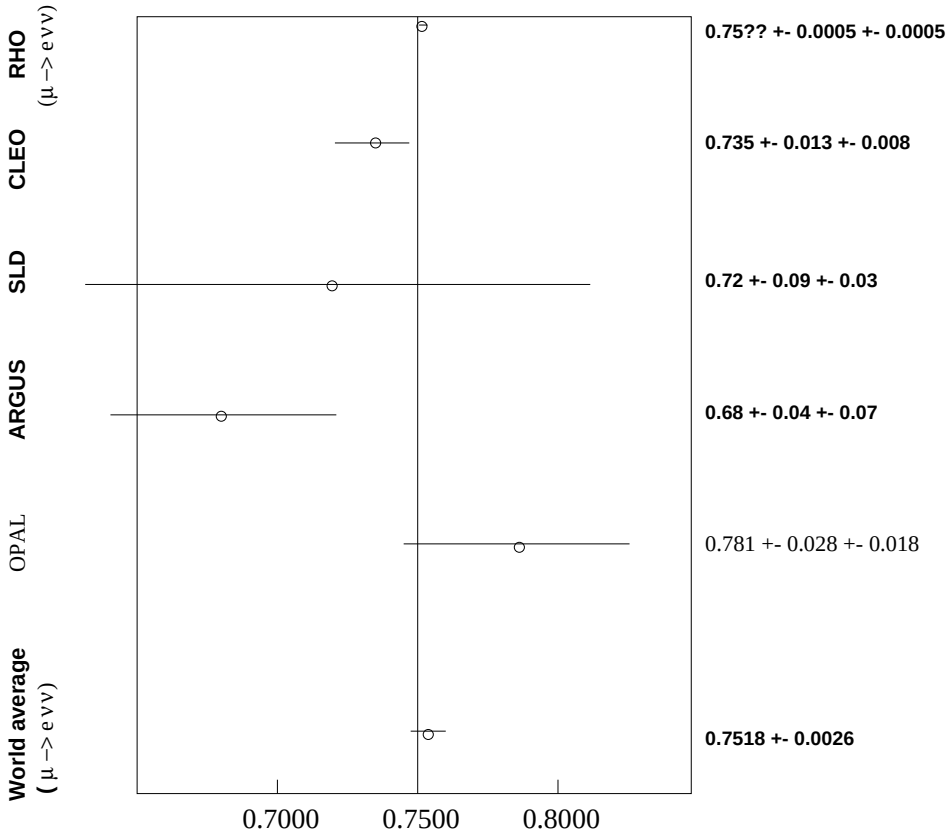

Figure 1.4: Some recent measurements of ρ and its world average

Chapter 2

Experimental Set-up

The RHO experiment was carried out at the former Los Alamos Meson Physics Facility (LAMPF) within the existing MEGA experimental set-up. Most of the MEGA set-up, including the positron detector system, was used by this exmperiment to measure the positron Michel spectrum [**?**] [**?**]. A cut-away view of the whole apparatus and its endview and sideview are shown in Figs. 2.1, 2.2, and 2.3. The main components are:

- a μ^+ beam
- a plastic target
- 8 cylindrical MWPCs
- 2 plastic scintillator barrels, each having 87 scintillator bars
- a large superconducting solenoid (producing an approximately uniform, 1.500T magnetic field directed along the cylindrical axis)

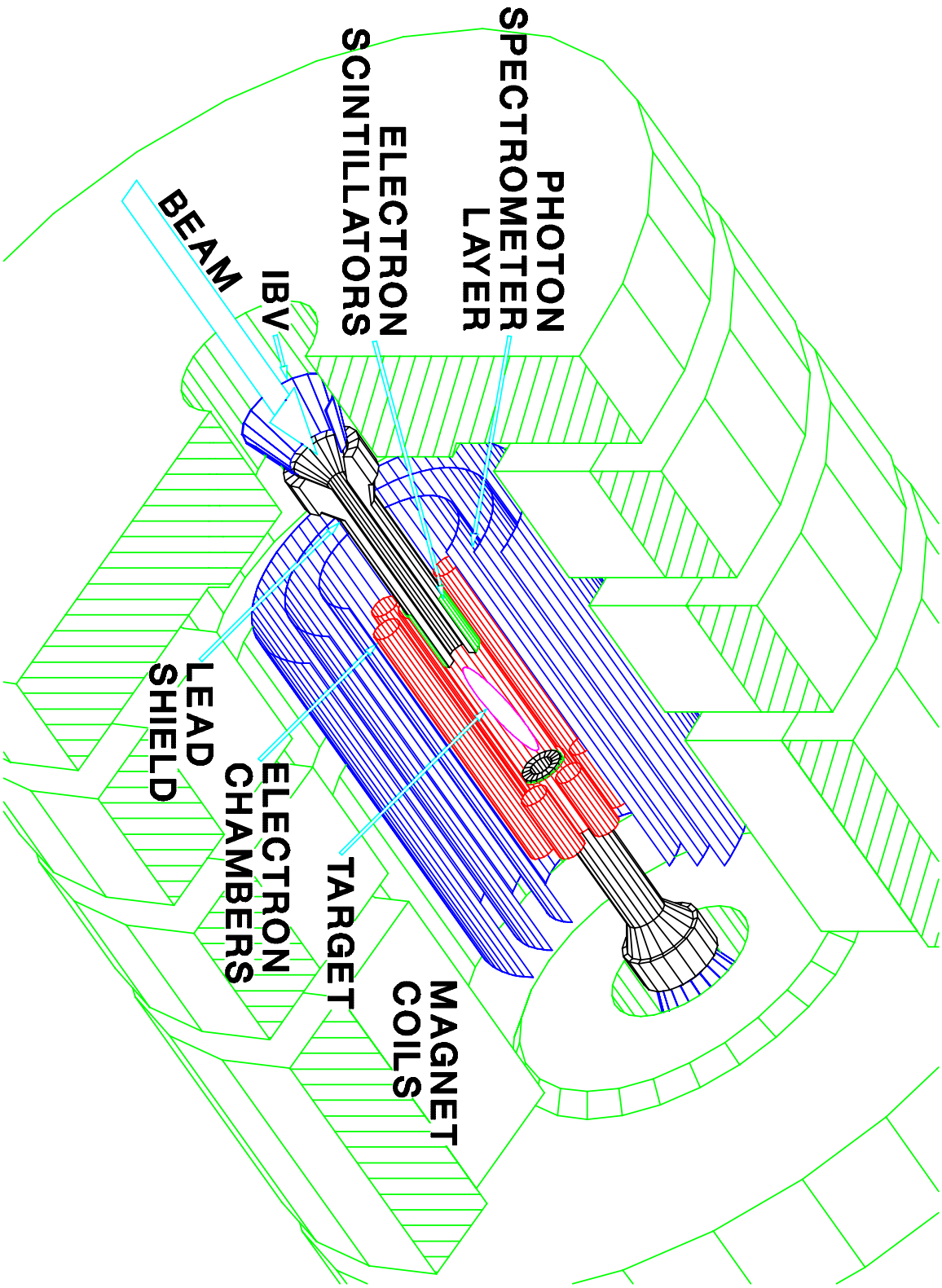

Figure 2.1: Cut-away view of the MEGA detector

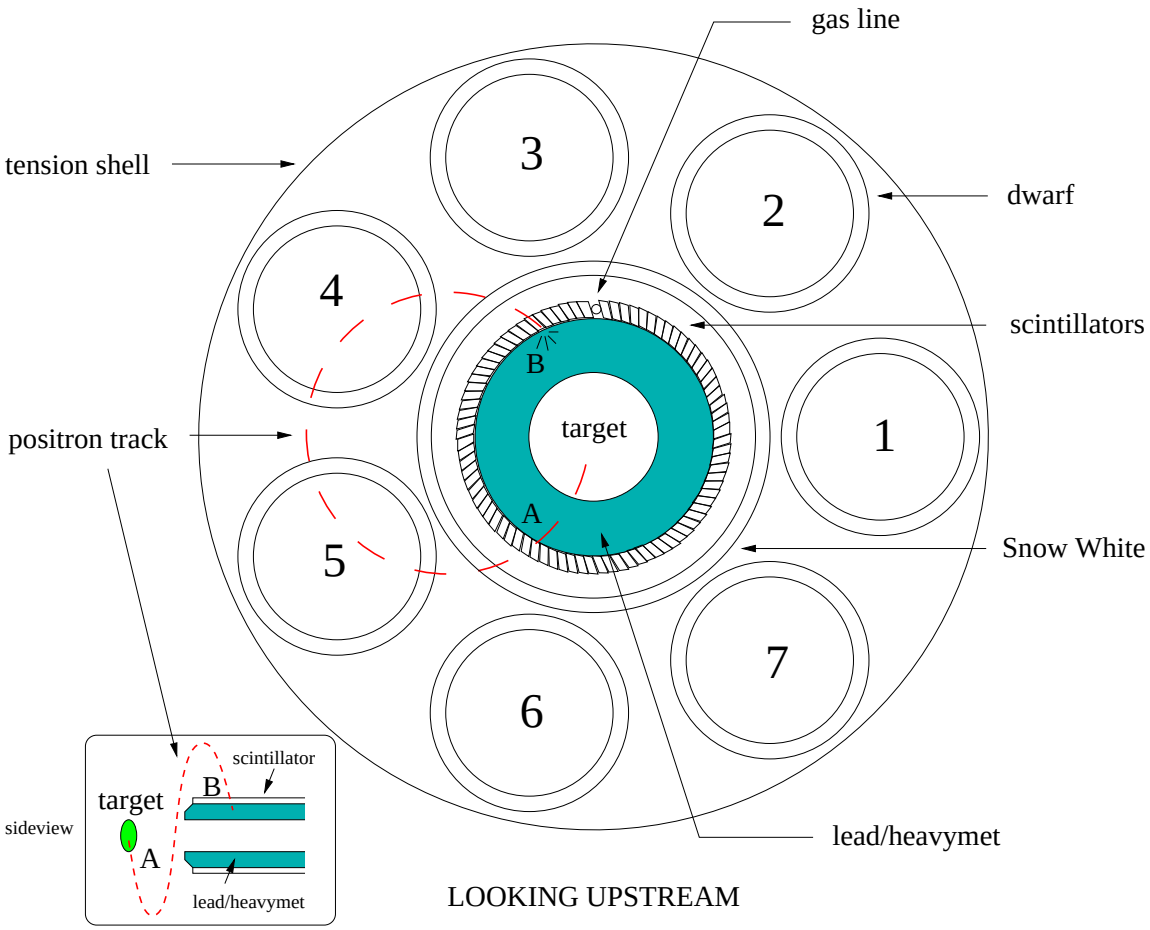

Figure 2.2: End view of the MEGA detector (looking upstream)

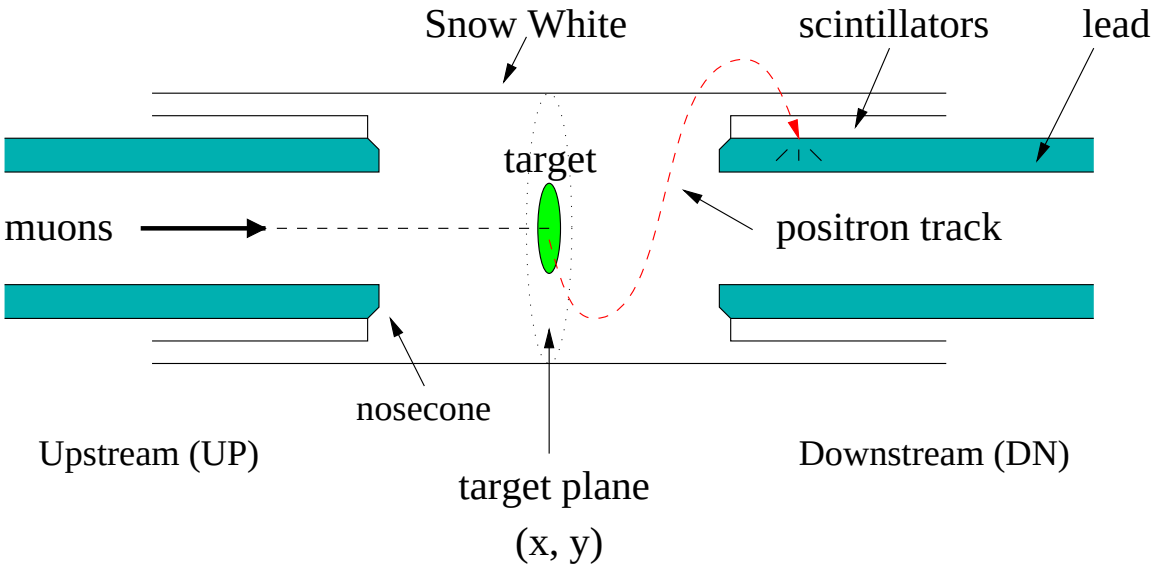

Figure 2.3: Side view of the MEGA detector

- a data acquisition system.

The muon enters along the axis of the solenoid, stops at the target, then decays. This experiment measures the dominant decay mode, $\mu^+ \rightarrow e^+\nu\bar{\nu}$. The outgoing positron spirals along the solenoid axis in the magnetic field, crossing chambers (if it has enough transverse momentum), hitting the scintillator barrel, and finally stopping in the lead. The track of such a positron is a helix, reconstructed by the hits on the chambers. The parameters of the helix give the momentum of the positron. The chambers are made to be low mass and the energy resolution for a positron due to multiple scattering at all the chamber crossings is about 450 keV (FWHM) at its maximum momentum of 52.8 MeV/c. The positron can go either upstream (backward) or downstream (forward) with respect to the beam, with its track reconstructed in that half of the detector system.

The size of the positron spectrometer was designed to be large enough to contain all spiraling positrons from muon decay inside the system. For positrons with energy between 30 MeV

and the maximum energy, 52.8 MeV, (i.e., $0.75 < x < 1.0$, where $x = \frac{E}{E_{max}}$, E is the energy of the positron and $E_{max} = 52.8$ MeV), the detector's acceptance is reasonably good. For positrons with energy less than 30 MeV, their orbits are so small that they do not make it to the chambers and can not be detected. The Michel parameter ρ is sensitive only to the shape of the spectrum at the high energy end, so this acceptance feature inherent in the MEGA design does not affect the measurement of ρ.

Above is a brief description of the components of the whole experimental set-up. In the following each of the components is discussed in more detail.

2.1 Beam

The μ^+ beam is produced by the decay $\pi^+ \rightarrow \mu^+\nu_\mu$ in the Stopped Muon Channel at LAMPF (see Fig. 2.4). Due to maximal parity violation in the decay, the μ^+ beam is fully polarized along its motion when produced. When taking RHO data, two types of beams were used: a "surface beam" which comes from the pion decays at rest on the surface of the primary target, and a "decay tune" which comes from pion decays in flight within the Stopped Muon Channel. In the former, the μ^+ beam has the polarization antiparallel to its motion, while in the latter, the μ^+ beam has the polarization parallel to its motion. See Fig. 2.5. The reason that "decay tune" data were taken in addition to the "surface beam" data is that they provide an excellent check on polarization-dependent systematic errors (see Equation 2 or 3 in Chapter 1).

The surface beam is tuned to have a central momentum of about 27.5 MeV/c with polarization above 90%. With this momentum the distance from the muon production target (A2

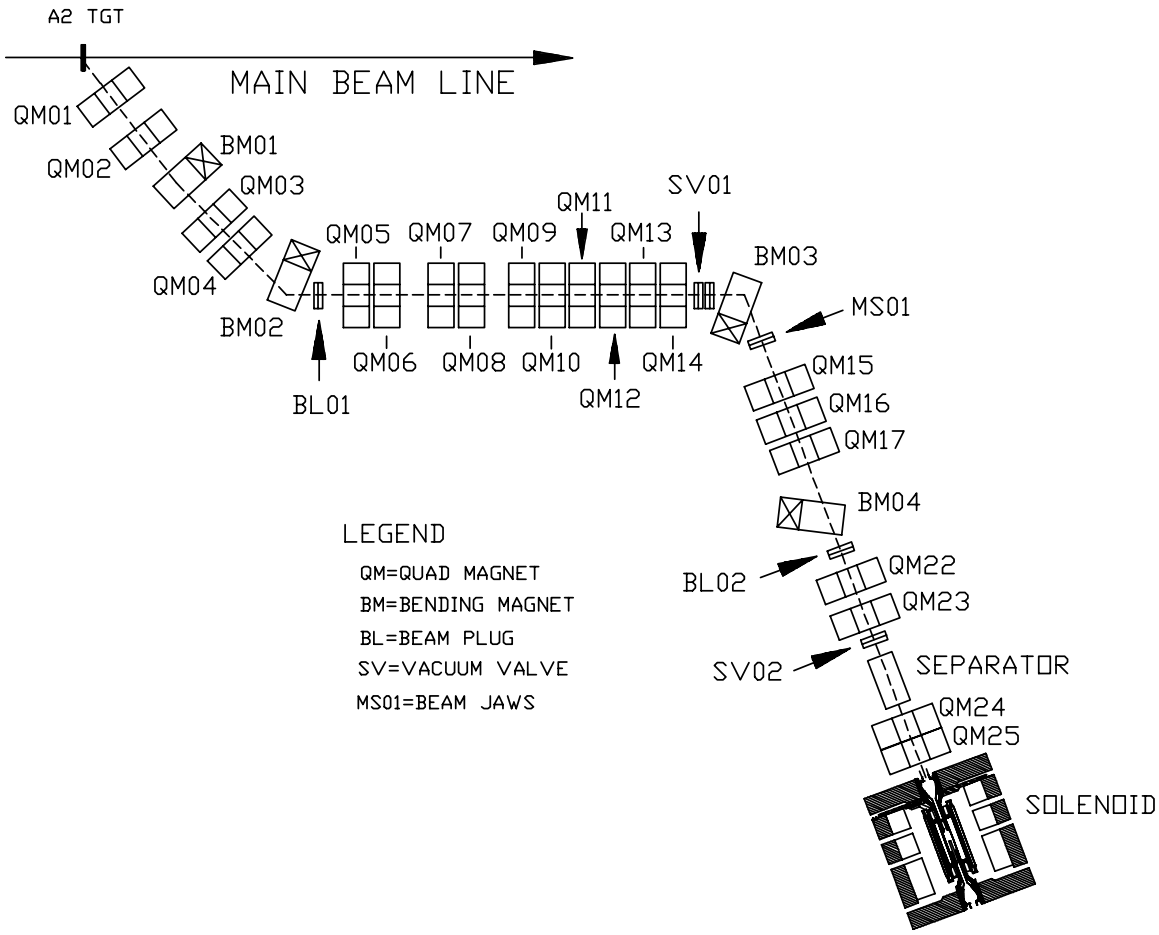

Figure 2.4: Stopped Muon Channel at LAMPF

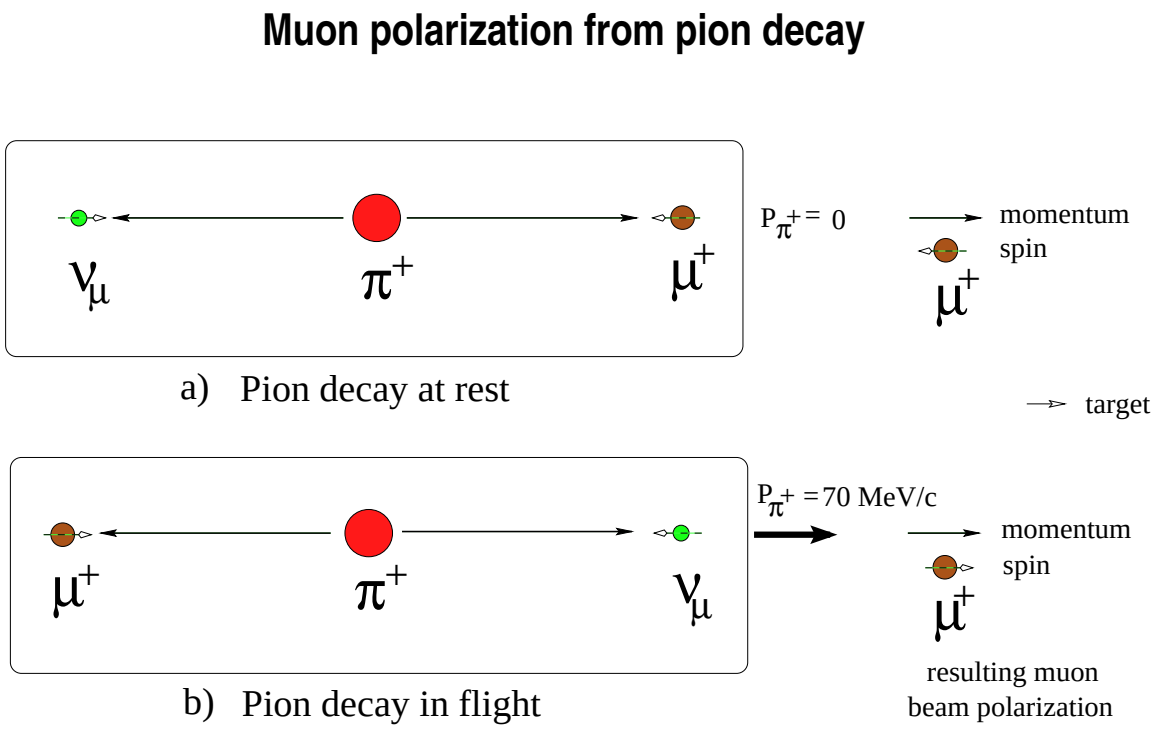

Figure 2.5: Muon spin polarizations for the two cases

target) to the RHO detector system is larger than 20 times the distance traveled by pions in one lifetime, so the pion contamination is negligible. The muon beam from the Stopped Muon Channel (Fig. 2.4) has high intensity but RHO can only use a small portion of it. The excessive beam flux is reduced by installing a collimator on the upstream side of the beam. The overall beam flux is tuned so that there is one muon decay recorded for each trigger.

It is desirable that most of the muons are stopped and decay in the target. This requires that the muon beam have the right momentum. This is obtained by carefully adjusting the thickness of a degrader that is glued to the front window of the target support bag. The relative momentum spread $\Delta p/p$ of muon beam needs to be as small as possible for the same reason. It is about 6% and is achieved by turning off the quadruples QM07 to QM12 of the Stopped Muon Channel (see Fig. 2.4).

The decay tune was produced by extracting muons with a momentum of 28.5 MeV/c from 70 MeV/c π^+s decaying in flight in the decay section, QM05 to QM14 (see Fig. 2.4). As shown in Fig. 2.5, those muons are emitted backwards in the π^+ rest frame so that their spin polarization is parallel to their direction of motion in the laboratory frame. Compared to the surface tune, the muon flux in the decay tune was much lower so the collimator was not necessary and was removed while DY data were being taken. The momentum spread and beam spot size were therefore larger than those of the surface tune.

For the surface tune, two types of data were taken under different magnetic field: S1 data were taken under normal magnetic field (1.500 T), and S2 data were taken with reduced magnetic field (1.425 T). The purpose of this was to check the acceptance of different parts of the chambers. In a reduced magnetic field, the positron helical track of a given momentum has a larger radius and crosses the outer parts of the chambers. By taking some of those

data, information about the outer parts of the chambers can be extracted and used in the analysis of chamber properties.

2.2 Target

At the center of the detector system is the target on which muons are stopped and decay. The target is a circular mylar disk, with a thickness of 0.254 mm and a radius of 5 cm. It is placed normal to the beam and is supported by a cylindrical bag inflated with helium. The thickness of the degrader upstream of the target was carefully chosen so that most of the surface beam would stop in the target. The transverse cross section of the beam was such that it illuminated the entire target.

2.3 Chambers

Of the eight cylindrical MWPCs, seven are of equal size with 12 cm diameter and 126 cm length (called the "Dwarfs"), and one is larger in cross section with 22 cm diameter and the same length as the Dwarfs ("Snow White"). These MWPCs are arranged so that

the "Snow White" is surrounded by the "Seven Dwarfs."

See Fig. 2.2. This special geometry of chambers was chosen to optimize the energy resolution at 52.8 Mev for the MEGA experiment.

The wall of each MWPC is a layer of anode wires sandwiched by two cathode foils ("inner" and "outer" cathodes). The anode layer of each Dwarf (Snow White) is made of 288 (540)

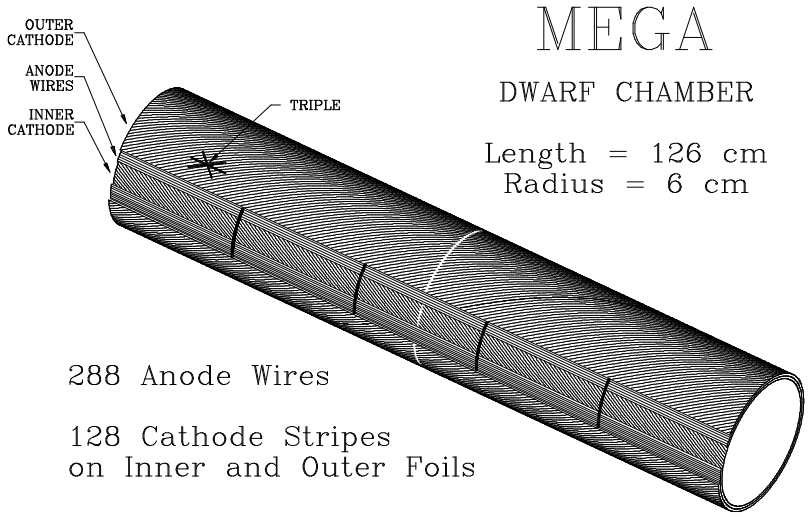

Figure 2.6: A Dwarf chamber

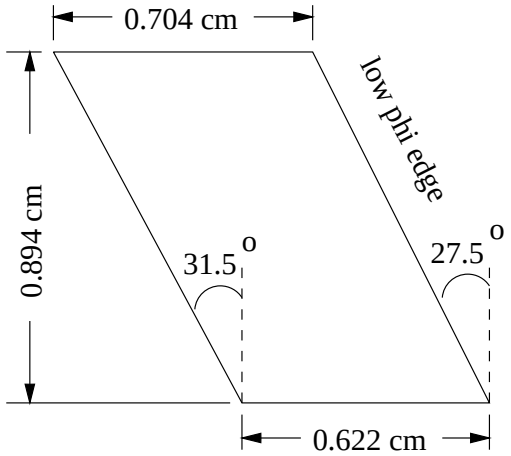

Figure 2.7: Cross section of a scintillator

15 μm diameter gold-plated tungsten wires with a 1.3 mm pitch. See Fig. 2.6. The cathode foils are 25 μm thick Kapton with 200 nm vapor-deposited copper on one side. The copper surface is scribed to form spiral cathode strips of 3 mm width. These strips make a complete revolution over the entire length of the chamber with an opposite sense of rotation on the inner and outer foils.

A thin insulating break is scribed along the circumference of the cathodes at $z = 0$ for Dwarfs and at $z = \pm$ 33 cm for Snow White, dividing the Dwarfs into two isolated sections, and Snow White into three with the middle section unstriped. This design was particularly necessary for the high-rate conditions in MEGA experiment. By doing so, the Dwarf cathode occupancy was reduced and the central region of Snow White (closest to the target) did not register extremely high-rate hits that would have otherwise confused the pattern recongnition. The $z = 0$ breaks the detector into "upstream" ($z < 0$) and "downstream"($z > 0$), and the cathodes efficiencies are determined separately for upstream and downstream.

The cathode foils, which have no support except at the ends, are held in place along their length to within 75 μm by differential gas pressure. When high voltage (about 2000 Volt) is applied, the anode wires tend to be attracted towards the cathode foils due to electrostatics, and the tension of the anode wires (28 g) is not enough to counteract this along the whole length. To solve this problem, restraints called garlands are used. They are 0.66 cm thick stiff glass-fiber rings mounted between the anodes and inner cathode foil with 6 glass beads equally spaced around the circumference of the ring. A band of 100 μm polyester filament constrains the anodes to the garlands. The garlands were designed to have as low mass as possible and they do not deaden a large region of the chambers or create dark currents from corona or surface currents. Four garlands are installed in each dwarf chamber with equal

intervals (25.2 cm) at $z = \pm 12.6$ cm and ± 37.8 cm, and three in Snow White at $z = 0$ and ± 31.5 cm.

The chambers are inserted into a large rigid cylinder called the tension shell. It is made of aluminum and filled with helium gas which has much smaller scattering cross section and energy loss than air. The shell wall is located at a radius outside the orbits of the positrons with the maximum transverse momentum (52.8 MeV/c) from μ^+ decay at rest so that all the positron tracks are well contained in the whole apparatus and can be detected by the chambers. The chamber end assembly is fastened to the ends of the tension shell. The anode wire tension is maintained by the tension shell.

The chambers are operated with a gas mixture of 80% CF_4 and 20% isobutane, with a small amount of water ($\sim$ 0.2%) to quench the dark current. This particular gas mixture was originally adopted in the MEGA experiment for high rate operation. Although in the RHO experiment this was unnecessary, the same gas mixture was used.

When a positron crosses through a chamber wall, the fired anode wire gives the (r, ϕ) coordinate of the crossing and the triple coincidence of the anode and inner and outer cathode strips gives the z location. Because the thin chamber wall is light in mass, the radial thickness is only 3×10^{-4} radiation length for one crossing. In a typical event, the positron makes 6 crossings. The total energy loss from all crossings is therefore about 2×10^{-3} wich is so small that it can be neglected.

The parameters of the MWPCs are summarized in Table 2.1.

Table 2.1: Parameters of MWPCs (Dwarfs and Snow White)

length	126 cm
diameter	12 cm (Dwarfs), 22 cm (Snow White)
anode wires	15 μm diameter gold-plated tungsten,
	1.3 mm spacing
cathode foils	25 μm thick Kapton with 200 nm
	vapor-deposited copper on one side
cathode strips	3 mm wide
gas mixture	80% CF_4 + 20% isobutane + 0.2% water

2.4 Scintillators

There are a total of 174 plastic scintillators installed in the positron spectrometer. They are grouped together to form two cylinders or barrels, one in UP, one in DN, with 87 scintillators in each. The barrels are inserted inside Snow White (SW) with their near ends 33 cm away from the center of SW (where the target is located). The near ends are blackened to absorb the reflected light and the far ends of the scintillators are instrumented.

Each scintillator bar has a trapezoidal cross-section with acute angles of 31.5^o and 27.5^o, designed for two purposes: one to closely pack the scintillators into a cylinder (of 8.963 cm inner radius); the other to match the strike angle of incoming positron tracks in order to reduce scintillator multiplicity; see Fig. 2.2. Data and Monte Carlo multiplicity studies show that with this trapezoidal cross-section, 70% of the time there is only one scintillator fired by a positron. The dimensions of a scintillator are shown in Fig. 2.7. Each scintillator is

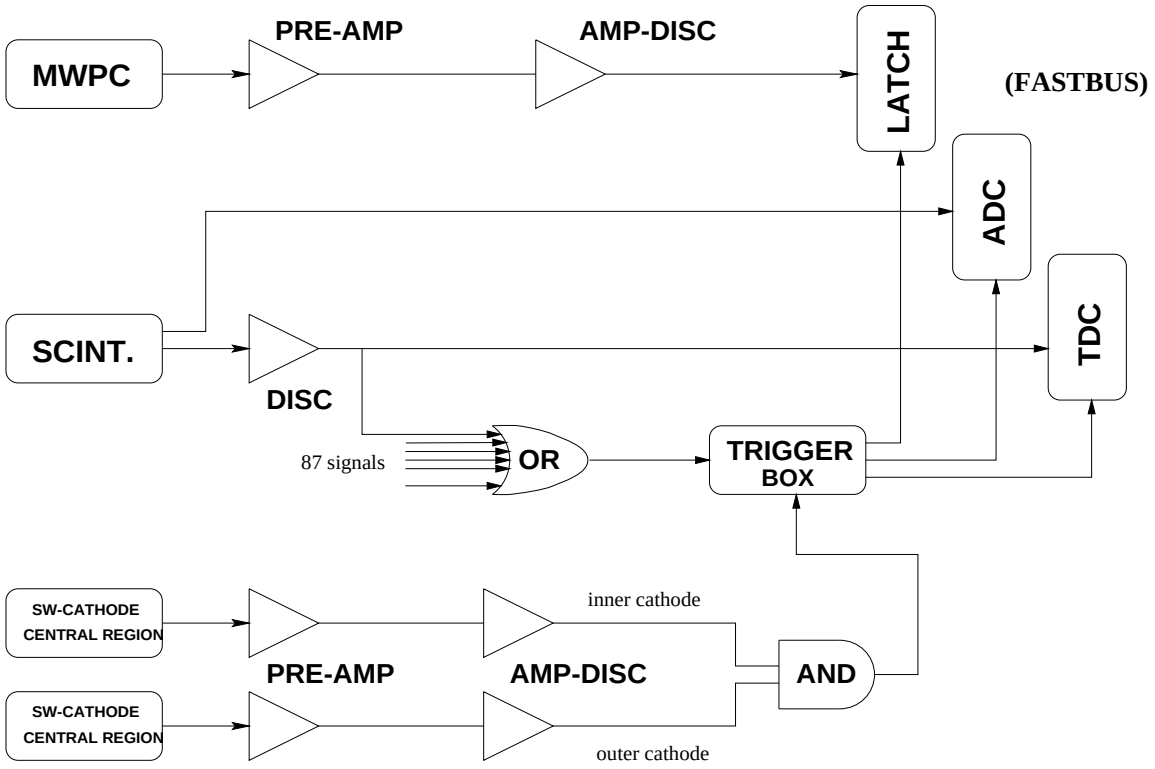

Figure 2.8: Electronic read-out system of RHO

wrapped in aluminum foil to optically isolate it from its neighbors as well as outside light.

2.5 Electronics

A schematic layout of the signal read-out system of RHO experiment is shown in Fig. 2.8.

The signals from individual anode wires are read out from one end, either UP or DN separately in groups of 16 (i.e., in the unit of an anode pre-amp card). The signals from cathode strips (inner and outer) are read out independently from both ends. These signals first go through a pre-amplifier, mounted on the chamber, with a gain of about 40. The output is fed to an amplifier-discriminator near the detector that produces a logic signal if the ampli-

fied signal passes the threshold of the discriminator. The logic signals are then delivered to FASTBUS latches in the counting house.

The signals from the far ends (away from the target) of the scintillators are collected by photomultiplier tubes via 1.8 m optical fiber light guides. To avoid the effect of the strong magnetic field, these phototubes are shielded and placed away from the magnet. The output of each phototubes fans out two ways: one goes directly to a FASTBUS ADC; the other goes through a discriminator, and then fans out two ways again: one directly to a FASTBUS TDC, the other to an 87-way OR logic unit, and then to the trigger box. A trigger of the event is then issued to the FASTBUS from the trigger box. The ADC signal gives the pulse height proportional to the energy deposit in the scintillator. The TDC gives the timing of each scintillator hit in an event so that a comparison between several hits in an event can be made in the analysis.

Scintillator efficiencies can not be measured using the normal data because they are self-triggered. A special type of data was taken from which the scintillator efficiencies can be extracted. The trigger for this kind of data comes from a positron hit on the central unstriped region of Snow White when the positron first leaves the target and begins to spiral inside the detector system, and is therefore called Snow White triggered data. Six sets of such runs were taken (T1, T2, ..., T6). See Fig. 2.9. (Numbers like 4120 etc in the figure are the run numbers, with roughly 2 million triggers each). This Snow White trigger corresponds to the third signal read-out in Fig. 2.8. The signal goes through the same first two stages as that from the cathode strips. The output from the amplifier-discriminator is fed into an AND logic unit (for inner and outer cathodes) whose output is sent to the trigger box.

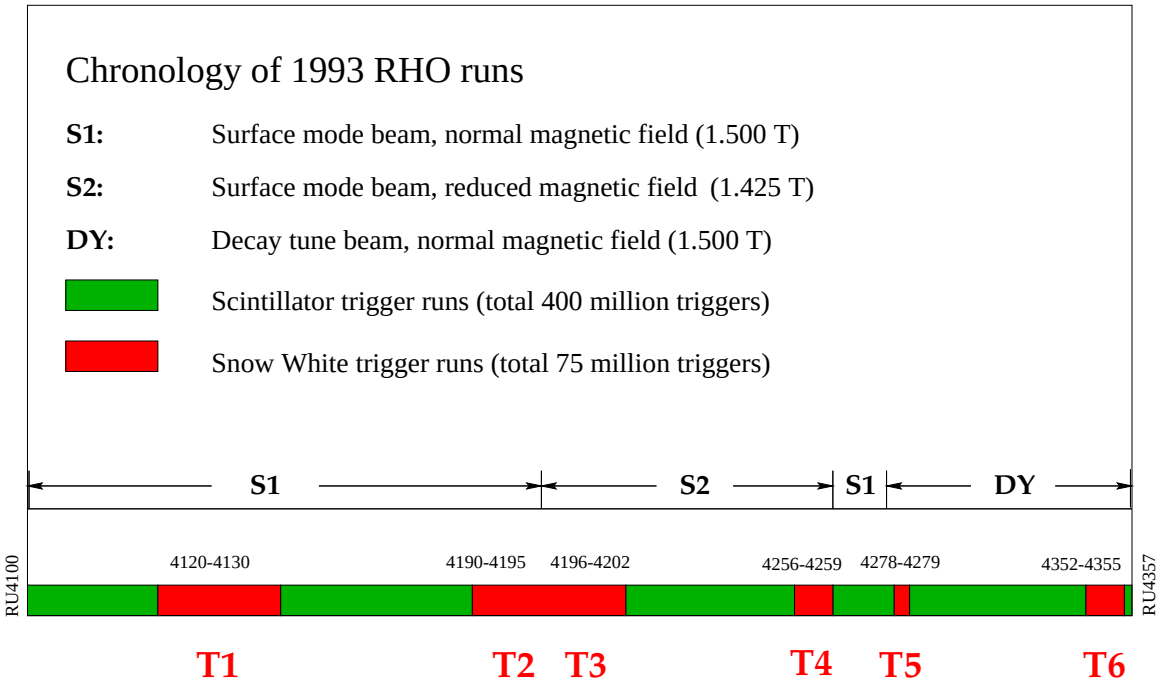

Figure 2.9: Chronology of 1993 RHO runs

2.6 Data Acquisition

The electronic signals from the read-out system that are stored in FASTBUS latches, TDCs and ADCs should be recorded on magnetic tape for off-line analyses. A CERN Host Interface (CHI) reads the raw data and sends it to the online Workstation Farm via the FASTBUS to Branch Bus Connector. The optimized rate of this data transfer is very high, about 2200 KB/sec. The data is unpacked in the computers and copied to the tapes that operate at a maximum data taping rate of only 200 KB/sec. In order to prevent the data flow from being jammed, two things have been done in the Workstation Farm to reduce the size of the data per second written to the tapes: one is to use an on-line filter to reject events that do not meet some basic requirement; the other is to compress the data.

The on-line filter does the following:

First it maps the FASTBUS module channels to detector elements.

Then, it throws out overly noisy events from which no useful information can be retrieved. An event is considered noisy if the number of fired anode wires in any chamber is larger than 150 (half of circumference of a dwarf chamber) or the number of fired cathode strips in each chamber is larger than 100. About 8% of the raw triggers are thrown out this way.

Finally, it throws out events that do not have enough information for track reconstruction: it requires a minimum of 2 chambers with hits, at least one Snow White anode hit and at least one hit in each of the three layers for a dwarf chamber.

Another 40% of the raw triggers are thrown out this way.

The remaining data were compressed by converting from the fixed length data format to the FASTBUS modules sparsified format. This turns out to be extremely efficient. About 86% of the memory space is saved by this compression.

The filtering and compression reduce the required rate for taping from $\sim$ 2200 KB/sec to $\sim 2200 \times 92\% \times 60\% \times 14\% \cong 2200 \times 8\% \cong 170$ KB/sec, which is within the maximum taping rate of 200 KB/sec.

The formal data taking for RHO was completed in the summer of 1993. The apparatus continued to be used for the MEGA measurement until October 1995 when the last data taking for MEGA was finished.

Chapter 3

Some Basics of Data Analysis

In this short chapter, we briefly discuss the positron track reconstruction and some of the basics of our data analysis.

The positron tracks are reconstructed from the hits on the chambers. A typical hit on a chamber is a *triple*, with its (x, y) position determined by the fired anode and z location determined by the crossing of anode and outer/inner cathode wires. See Fig. 3.1 and Fig. 2.6. In reality, a positron hit may cause a number of wires to be fired in the vicinity of the actual crossing point, so we have used the following criteria to select the good hits while filtering out the fake hits caused by random coincidence or electronic noise. We require that 1) the maximum width of a group of fired wires, or a *cluster*, is 15 for anodes and 8 for cathodes; 2) the maximum gap between wires within a cluster is 3 for anodes and 4 for cathodes. The centroids of the clusters are taken as the *effective positions* (x, y, z) of the hit. Quite often the centroids of the anodes and cathodes do not meet at one point, so another criterion is applied: if the difference between the z intersections of the anode cluster and the two

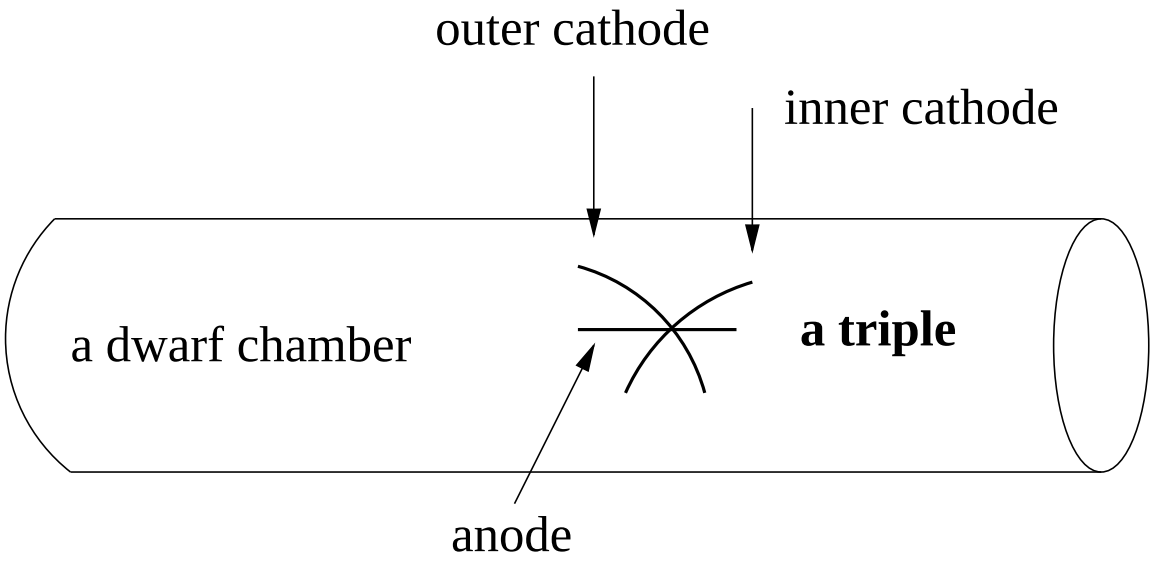

Figure 3.1: A typical triple hit on a chamber

cathode clusters are within 2 cm, then it is a good *triple*, and the average of the two z's is taken as the z for this hit. The anode cluster alone determines x and y.

Depending on the magnitude of the momentum of the decay positrons and the initial direction, the positrons spiral with different loop counts between the target and the scintillator. Generally, the larger the longitudinal momentum, the smaller the number of loops. The most common loop counts are 0, 1 or 2. Fig. 3.2 is a scatter plot of the positron total energy vs. longitudinal momentum. The vertical bands correspond to positron tracks with different loops. Tracks with the largest (absolute) longitudinal momentum (25 MeV/c to 40 MeV/c) correspond to the 0-loop case, while tracks with longitudinal momentum from 11 MeV/c to 22 MeV/c correspond to 1-loop events. Negative longitudinal momentum refers to tracks going upstream. The gaps between the bands correspond to positrons that hit the face of the nosecone without passing through a scintillator. Notice that the 1-loop bands (upstream and downstream) have relatively uniform distribution along relatively longer range in y-axis,

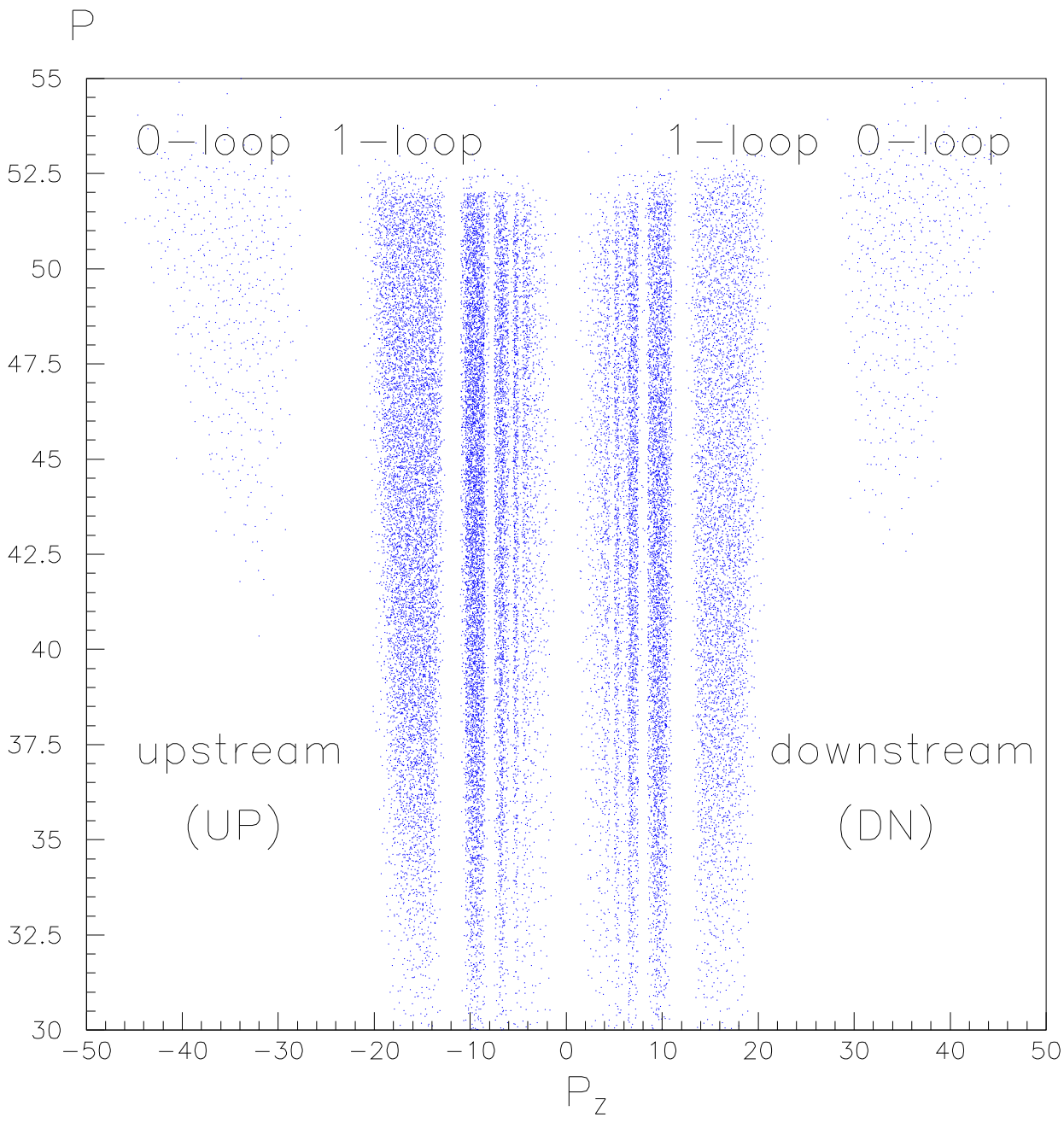

Figure 3.2: Positron momentum P (MeV) vs. longitudinal momentum P_z (MeV/c). Separation by loop numbers is clearly seen.

indicating that the detector system has a fairly uniform acceptance for 1-looper, thus they are most suitable for our measurement. When extracting the Michel parameter ρ, only 1-loop events in the range 40 MeV to 52.8 MeV are used.

Loop numbers are calculated from the reconstructed tracks by using the information provided by all the good hits as follows. Assuming a uniform magnetic field, a helical track can be parameterized by:

$$x = x_h + r_h \cos(\omega) \tag{3.1}$$

$$y = y_h + r_h \sin(\omega) \tag{3.2}$$

$$z = a_h + b_h \omega \tag{3.3}$$

where x_h, y_h and r_h are determined by anode hits, ω is the turning angle, and a_h and b_h are calculated from a least-squares fit of the z positrons of the triples to a linear function of ω. The number of loops N between the first$((x_1, y_1, z_1))$ and the last $((x_n, y_n, z_n))$ triples is determined by an exhaustive search. All the n hits are arranged by z (from near the target to away from the target), and a slope b_h is defined as:

$$b_h = \frac{z_n - z_1}{\omega_n - \omega_1} \tag{3.4}$$

for each tentative loop number (0,1,...,10). The resulting pairs (ω_i, z_i) are then fitted to a straight line and reduced χ^2 is used as the goodness of the fit. The smallest value of reduced χ^2 determines the true loop number N.

The loop counting algorithm can be tested by comparing its result to the result from hand-scanning events using our event display program. 95% of the times they match. Because the same algorithm is used both in analyzing experimental data and Monte Carlo data, the

fact that the algorithm does not have 100% accuracy does not affect the determination of ρ in any significant way.

The momentum of the positron is expressed in terms of the positron's helical track parameters, r_h and b_h described above, and the magnetic field B:

$$\begin{aligned} p_T &= Kqr_hB \\ p_L &= Kqb_hB \end{aligned} \tag{3.5}$$

where p_T and p_L are the positron's transverse and longitudinal momentum in MeV/c, K=300 (MeV/c)/Tm, q is the charge of the positron in units of e, B is the central value of the magnetic field in Tesla, and r_h and b_h are the radii in cm of the helix and the slope of the $z - \phi$ relation, respectively. Note that the helical track with the minimum transverse momentum that crosses the inner part of the chambers has a radius r_h of about 5.5 cm (half of the Snow White radius) and corresponds to $p_T \sim 25$ MeV/c. The maximum r_h is about 12 cm, which is half of the sum of the diameter of the dwarfs (12 cm) and the radius of the Snow White (11 cm) plus a small gap between them; this corrsponds to $p_T \sim 54$ MeV/c. Therefore the detector system has a good acceptance in the range 30 MeV/c - 52.8 MeV/c and positrons with high transverse momentum are well contained in the detector system.

Throughout the analysis in the rest of this thesis work, all experimental data (both normal RHO data and SW trigger data) are analyzed using a set of computer programs developed for MEGA and modified for RHO, and the Monte Carlo data are created using another comprehensive set of programs (MEGASIM [**?**]), in which we simulate the physical processes and all geometrical information, electrical and electronic operations. The analysis code is identical to that for the experimental data. Monte Carlo simulation is used not only for extracting ρ by comparing spectra with experimental data, but also as a tool for studying the properties of the positron spectrometer, for example, the alignment of certain spectrometer

components, beam parameters and determination of various systematic errors. These will be dicsussed extensively in Chapter 4 and 5.

Chapter 4

Systematic Uncertainties

4.1 Overview

For a measurement like RHO, the main purpose of the experiment is to perform a measurement with high precision. This means we need to keep the total error of the measurement (statistical and systematic) as low as possible. We have taken about 400 million triggers during the summer of 1993. This corresponds to a statistical uncertainty on ρ of around 0.0006. In order to keep the total error under our goal of 0.001, the total systematic error has to be controlled within 0.0008.

There are many elements in the detector system that can contribute to the systematic error. Table 4.1 lists the possible sources of systematic uncertainties in our analysis.

Unlike other parts of the analysis, making an accurate estimate of systematic errors is always a difficult task in any experiment because there are no established methods to follow. Every particular problem has to be solved in its own way. During the RHO analysis we have

Table 4.1: Summary of expected systematic error contributions to ρ

Source of systematic error	Expected Uncertainty	Projected error in ρ
scint inefficiency UP/DN	0.001	0.0004
chamber inefficiency	0.001	0.0005
barrel azimuth	0.5 of a bar width	0.00002
barrel center (x or y)	0.10 cm	0.00003
barrel center (radius)	0.14 cm	0.00005
beam stop centroid	0.5 μm	0.00004
chamber location	5 μm	0.00006
δx	0.2 keV	0.00012
δB	0.000004 T	0.00012

developed different new techniques and methods for problems we have met. They will be described in detail in this Chapter.

As previously mentioned in Chapter 2, the positron spectrometer used here was originally designed for the MEGA experiment. Its design was not optimized particularly for the RHO measurement.

There are six steps involved in working on each of the systematic uncertainties. They are:
1) identify the source of a potential disturbance that affects ρ
2) find a suitable parameter that quantifies the size of the disturbance
3) measure or estimate the size of this disturbance
4) apply a correction to ρ based on this measurement or estimate
5) determine the residual uncertainty of the measurement or estimate
6) determine the projected uncertainty in ρ due to this residual uncertainty
Examples are the scintillator barrel azimuthal offsets (for example, -0.014 rad for upstream) or scintillator efficiency upstream/downstream ratio (for example 1.109). The residual uncertainty in 5) is the precision with which we can determine the parameter, for example, it is 0.003 rad for scintillator barrel azimuthal offsets and 0.025 for the scintillator efficiency upstream/downstream ratio. Using the estimated uncertainty on the parameter from 3) we determine how this source affects ρ. It is important to note that it is the uncertainty in determining the parameter from 5) that determines the uncertainty in ρ due to this source, not the parameter itself from 3).

In the first half of this chapter we will discuss 1), 2) and 3). 4), 5) and 6) will be discussed in section 4.7.

Among all the systematic uncertainties, the scintillator and chamber efficiency uncertainties are the dominant ones. Because of their importance they will be discussed first in this chapter. We will also discuss the other possible systematic sources listed in Table 4.1 and describe the procedures to measure them. The results of these studies will be used in the final determination of the scintillator and chamber efficiencies. Because of the strong correlation between all these topics, there will be some forward references throughout this chapter. At the end of the chapter we will describe procedures in sensitivity checks on some of the main systematic sources and the estimation of their projected errors on ρ.

4.2 Scintillator Efficiencies

Most of the 174 scintillators used in the RHO experiment worked well and had high efficiencies. During the RHO data taking, some of them were not functioning properly or unstable due to problems with readout electronics, their phototubes or broken optical couplings. In this section we will discuss how the scintillator efficiencies are measured and how well they can be measured.

4.2.1 How Scintillator Efficiencies are Measured

As explained in Chapter 2, the scintillators trigger efficiencies cannot be determined from the RHO data runs because they are self-triggered. Some special runs were taken for measuring the efficiencies. They are called Snow White trigger runs. These SW trigger runs were taken immediately before and after any set of RHO runs.

The scintillator efficiency is defined in a single event as follows: a scintillator is said to be efficient if the reconstructed track points to this scintillator and the scintillator actually recorded a TDC hit; otherwise it is inefficient. In a particular Snow White triggered run, the efficiency of a scintillator is given by the ratio of the total number of efficient firings (N_a) to the total number of tracks reconstructed that point to the scintillator ($N_a + N_b$, where N_b is the number of tracks without the firings of the scintillator):

$$\epsilon = \frac{N_a}{N_a + N_b} \tag{4.1}$$

with

$$\sigma = \sqrt{\frac{N_a N_b}{(N_a + N_b)^3}} \tag{4.2}$$

as its uncertainty.

The "efficiency" defined above is "window of one" efficiency. We also use "window of 3" or "window of 5" efficiencies or barrel efficiencies. In those cases the struck scintillator is said to be efficient if any of the 3 or 5 or all 87 scintillators (see Fig. 4.1) recorded a TDC hit. The purpose for using this kind of finite window is to account for the cases where scintillators are off there expected positions and neighbouring scintillators recorded a hit instead. At certain stages of the analysis, a trigger efficiency was needed rather than scintillator efficiency, and "barrel efficiency" was used. Note that the same definition of finite window is also used in wire chamber efficiency (e.g., see section 4.3.1).

Once the efficiencies are determined from the SW runs, the efficiencies for the normal RHO runs between any two sets of SW runs can be derived, in principle, by appropriate interpolation. This may not be too difficult if there is no significant time dependence of efficiencies.

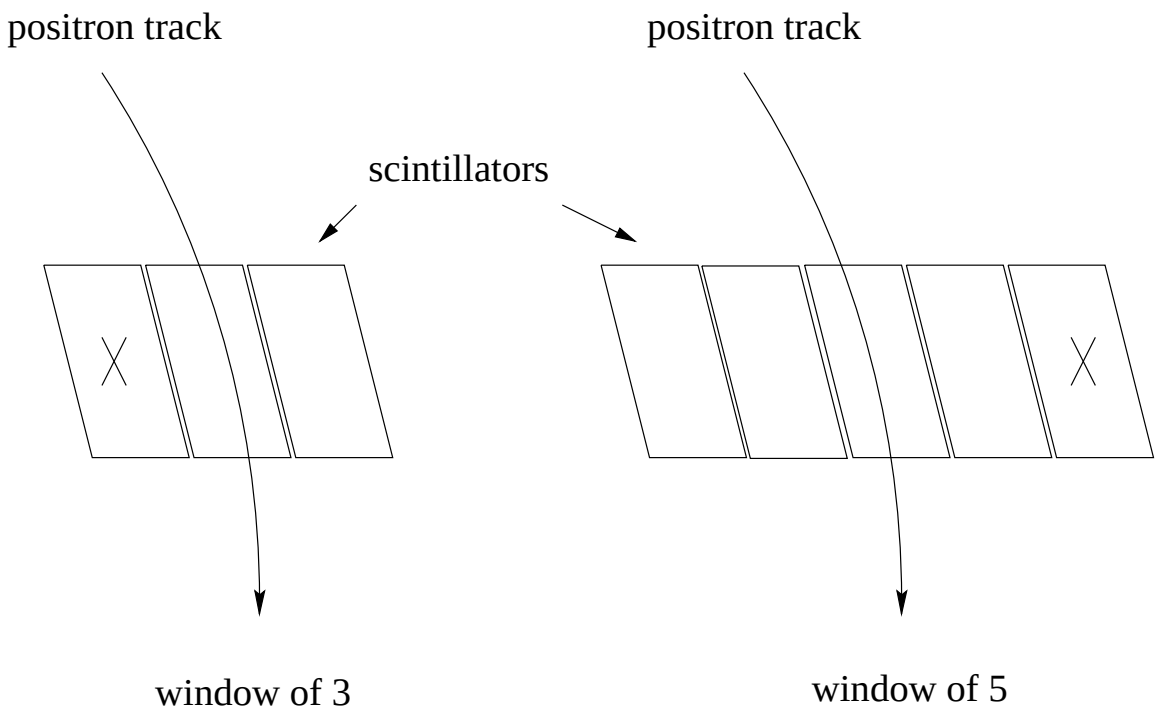

Figure 4.1: "Window of 3" and "window of 5" in efficiency determination

However, we do see time dependence. In section 4.2.3 this will be discussed further.

4.2.2 Upstream/Downstream Efficiency Ratio

As one of the dominant systematic sources, scintillator efficiencies contribute to the uncertainty in ρ through the upstream/downstream ratio. The importance of determining this ratio with a high precision is as follows.

As can be seen in Equation 4, the decay rate of muon is asymmetric between upstream ($90^o < \theta < 0^o$) and downstream ($180^o < \theta < 90^o$) due to the term $P_\mu \xi \cos\theta$:

$$\frac{d^2\Gamma}{dx d(\cos\theta)} \propto x^2 \Big\{ \Big[6(1-x) + \frac{4}{3}\rho(4x-3) \Big] r_1(x) + P_\mu \xi |\cos\theta| \Big[2(1-x) + \frac{4}{3}\delta(4x-3) \Big] r_2(x) \Big\} \quad (4.3)$$

(upstream)

$$\frac{d^2\Gamma}{dxd(\cos\theta)} \propto x^2\Big\{\Big[6(1-x)+\frac{4}{3}\rho(4x-3)\Big]r_1(x)-P_\mu\xi|\cos\theta|\Big[2(1-x)+\frac{4}{3}\delta(4x-3)\Big]r_2(x)\Big\} \quad (4.4)$$

(downstream)

This means that the distribution of decay positrons is asymmetric. There are more positrons going upstream than downstream, and the Michel spectra for upstream and downstream have different shapes.

Although the MEGA positron spectrometer was designed and constructed to be symmetric between upstream and downstream, there may still be a slight difference in the elements such as the performance of scintillators between the upstream and downstream. This difference needs to be estimated from data and put into the Monte Carlo simulation of the detector. Because events are scintillator-triggered, incorrect upstream and downstream scintillator efficiency ratio will slightly favor upstream or downstream Michel spectrum and therefore distort the spectra, which will cause the wrong value of ρ to be extracted. Note that the scintillator efficiencies themselves should also be determined as accurately as possible, but Monte Carlo study shows that it is the upstream/downstream ratio that contributes more to the uncertainty in ρ. This will be discussed further in section 4.7.

4.2.3 Efficiencies for S1,S2,DY and Time Dependence

The RHO data were taken under three different conditions. According to different beam types and different magnetic fields, they are called S1, S2 and DY runs. See Chapter 2. The definitions for these runs can also be found in Fig. 2.9. The purpose of taking these different data was mentioned in Chapter 2.

As shown in Fig. 2.9, we determine scintillator efficiencies for S1 data using SW trigger sets T1 and T2, and for S2 data using SW sets T3 and T4. Between T4 and T5 is a small sample of S1 data again, and for DY data T5 and T6 sets are used. In the figure, the number of events in each SW set and RHO set are approximately proportional to the length of the bars. The scintillator efficiencies are first determined from the bounding SW sets. Then by appropriate interpolation, the efficiencies for the corresponding RHO data are obtained. For example, to get efficiencies for S2 RHO data, efficiencies in T3 and T4 runs are first measured, then we interpolate them to find the efficiencies for S2.

The first four plots in Fig. 4.2 show the efficiencies (window of one) scintillator by scintillator, upstream and downstream, for T3 and T4. The average efficiency is about 95% for upstream or 94% for downstream. There are some scintillators that have low efficiencies, and a few that are dead. The efficiency upstream/downstream ratio for T3 (or T4) is defined as $\langle T3_{UP}/T3_{DN}\rangle$ or $\langle 4_{UP}/T4_{DN}\rangle$, and shown in the last two plots in Fig. 4.2. Comparing these two plots shows that the efficiency upstream/downstream ratio agrees between T3 and T4 within about 1%.

Since this level of disagreement limits our ability to determine ρ at the desired precision, as will be shown later, we need to identify the source of the change in the efficiencies from T3 to T4 so that the intervening data can be corrected for this drift. The performance of all the scintillators may have drifted in the same direction during this time period, or a few very unstable scintillators (for instance, dead in T3(T4)) may have caused the average efficiency to change. Also, for the changes from T2 to T3, or from T4 to T5, we would like to know if the change in magnetic field played a role via its possible effect on the scintillator phototubes.

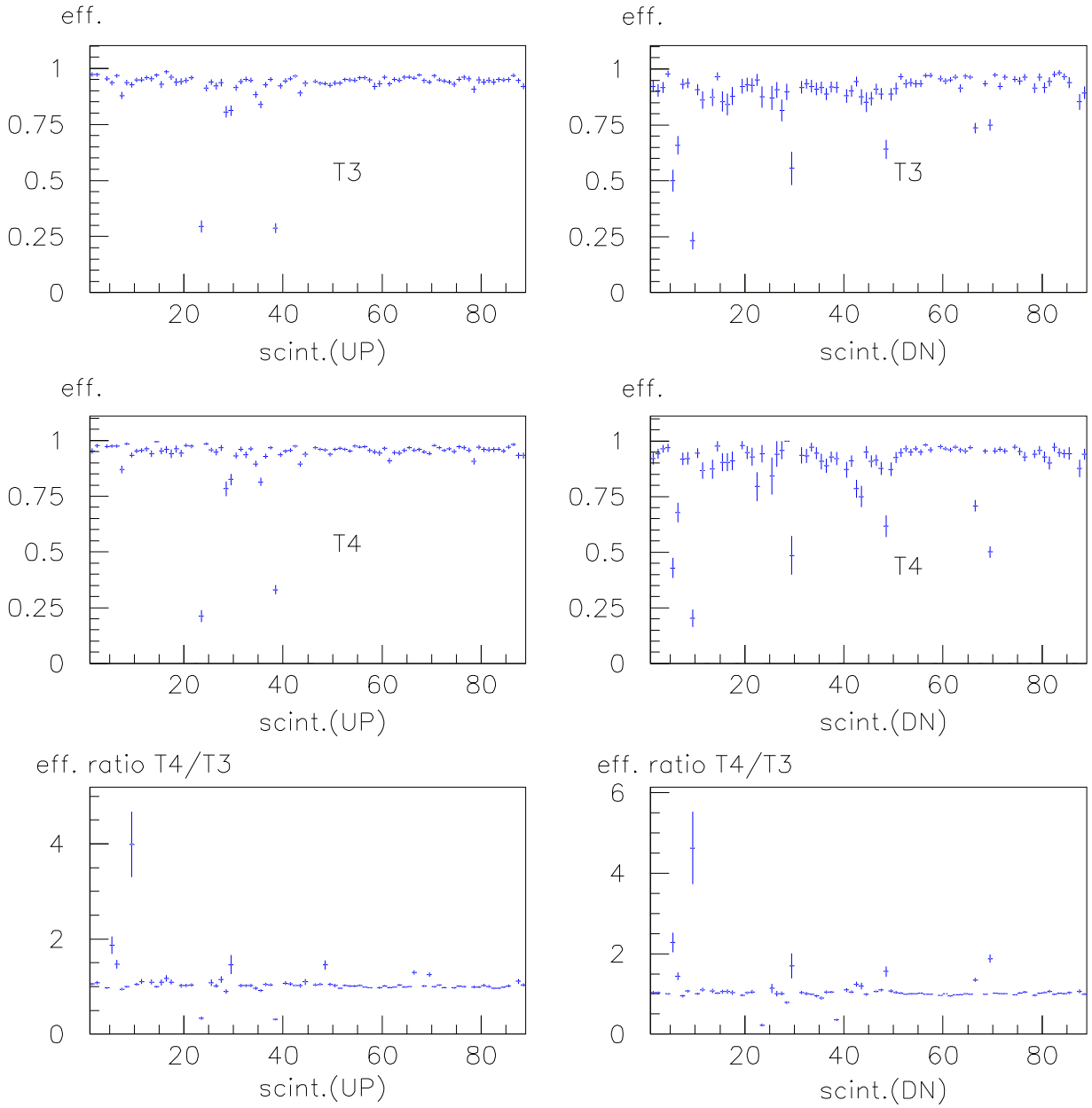

Figure 4.2: An example of scintillator efficiencies for two sets of SW data (T3 and T4). UP/DN efficiency ratio for T3 and T4 are shown in the lowest two plots. UP: upstream, DN: downstream. Horizontal axis is scintillator number (1 - 88).

Although the RHO runs between T3 and T4 (#4212-4242) do not give any information on the scintillator efficiencies, they may be helpful in giving us hints on how the scintillators performed during those runs. A change in hit frequency, whether sudden or gradual, might give us a clue why the efficiencies changed from T3 to T4 - but such raw frequency changes might also be unrelated to efficiency shifts. For example, we have looked at scintillator frequency plots in runs between T3 and T4. We found that scintillators #20-35 had a sudden drop in their frequencies between runs #4229 and #4230. It turns out the cause was not the scintillators themselves, but that Dwarf 4's voltage had tripped at that time. Some of the positron tracks that go through DW4 and hit scintillators in that region (#20-35) did not meet the reconstruction requirement because there were no hits on DW4, hence the drop of frequency on those scintillators.

We also found that the change of magnetic field influenced the performance of some scintillators. Specifically, from T2 to T3 (magnetic field changed from 1.500 T to 1.425 T), efficiencies of scintillators #17,18,23,24 and 30 of the downstream barrel dropped. When the magnetic field was changed back from 1.425 T to 1.500 T (T4 to T5), efficiencies of these scintillators came back up. It is likely that the phototubes were not completely shielded from magnetic field because of their location and orientation. But these five scintillators only account for a fraction of the scintillators whose performance changed. We do not know how to explain the drifts in those other scintillators.

Special note for T1: early study showed unusually high scintillator efficiencies in the first set of SW trigger data T1. It was found that this resulted from the online filtering condition under which that particular set of SW data were taken. The online filter then used "ADC or TDC" as the criteria to keep the event. Later it was changed to "TDC only" and all

the rest of SW data (T2-T6) were taken with "TDC only." The problem caused by using "ADC or TDC" is the following: since the pedestals on some scintillator ADCs shift due to electronic reasons, they may fire on pedestalwise. When this happens, the event passes the online filter and gets registered without a valid TDC hit.

Because of these difficulties, these data were not used.

4.2.4 Scintillator Strike Angle ψ

In this section we describe how scintillator strike angle dependence was characterized as well as the effort made to reduce the previously unknown systematic uncertainty associated with this dependence.

Consider the following: when a postiron strikes a scintillator, it excites the atoms and molecules inside the scintillator, causing scintillation light to be emitted. The longer the path length of the positron inside the scintillator, the more light will be generated and collected, and the higher the probability that the converted pulse height will exceed the threshold in the discriminator to give a signal. It is therefore expected that tracks with longer path length have higher efficiency. Because of the particular geometry of the scintillators, different strike angles (defined in Fig. 4.3) generally correspond to different path lengths. There are two factors that determine the strike angles: where the positrons come out of the target and the radius of the helix circle.

Monte Carlo studies show that strike angle changes when the decay point is moved away from center and/or the radius of the helix is changed. Fig. 4.4 shows that with an exaggerated shift of the beam center, the effect of the change of the strike angle around the azimuth is

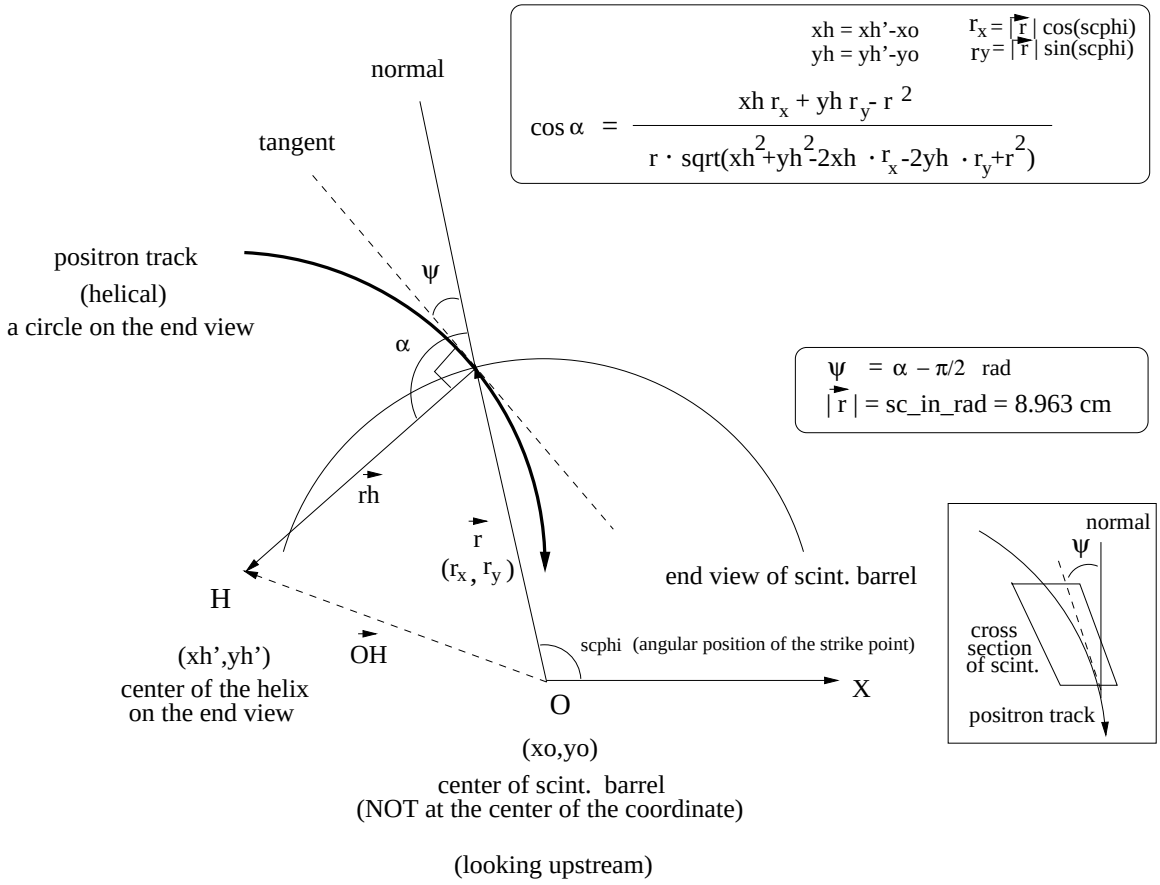

Figure 4.3: Definition of scintillator strike angle ψ

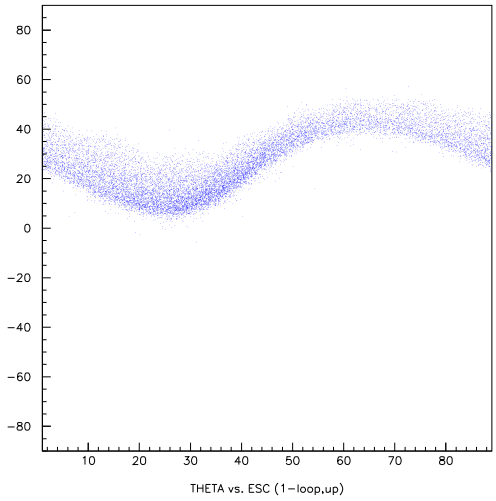

Figure 4.4: Monte Carlo result: ψ vs. scintillator number. To exaggerate the effect, the beam center in the x-y plane was moved towards scintillator #40 about four times the true offset.

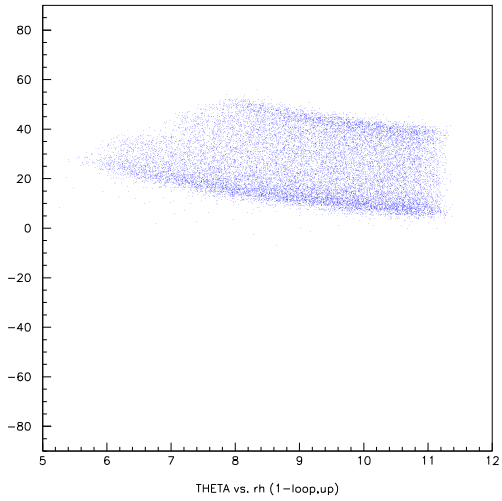

Figure 4.5: Monte Carlo result: ψ vs. radius of helix. Same condition as the previous plot.

apparent. This effect was not seen in experimental data before because in reality the offset of the beam center is still relatively small.

If the muon decays at the center of the target, the positron track will most likely hit only one scintillator, and ψ will be close to but somewhat less than the tilt angles of the two sides of the scintillator. This is in fact the very reason why the cross section of scintillators was designed with a trapezoidal shape. If the muon does not decay at the center of the target, then ψ will be smaller if the positron hits a scintillator which is on the same side as the decay point, larger if on the other side. We know the beam cross section has a nearly uniform distribution around the center (and close to a Gaussian type). Positrons with large

(small) energy have the same probability of making a large (small) ψ. Therefore there's not a biased acceptance of positrons because of this ψ dependence and the shape of the Michel spectrum will not be distorted.

Different decay points on the target correspond to different helix centers (for fixed radius) so if the beam spot is not centered at the origin, different segments around the barrel may get different ψ. That's why a good estimation of the beam spot location and size is important. The determination of beam spot is described in 4.6.

4.2.5 Scintillator Threshold Curve

In our Monte Carlo program it is the threshold of the TDC discriminator (see Chapter 2) that was actually used in recording scintillator hits from $\mu^+ \rightarrow e^+\nu_e\bar{\nu}_\mu$ events. The efficiencies that are put into Monte Carlo program are first converted into thresholds before the event simulation starts.

To create this efficiency-to-threshold curve, the Monte Carlo program is run using a common threshold for all scintillators.

The resulting simulated data are then analyzed and the efficiency of all 174 (2× 87) scintillators is calculated. This average efficiency and the corresponding threshold form a point for the threshold curve. We have used 10 different common thresholds which cover a fairly good range of possible efficiencies and obtained 10 such points to form a smooth threshold curve.

Fig. 4.6 shows Monte Carlo results of a set of scintillator efficiency curves. Each curve in the figure corresponds to a certain common threshold. The curves in the lower (higher) part of

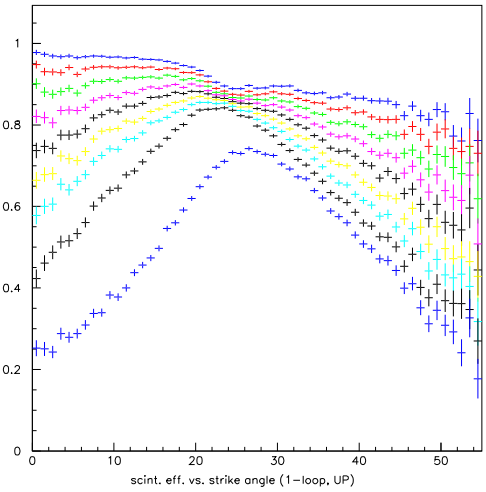

Figure 4.6: Scintillator strike angle (ψ) dependent efficiency curves for different scintillator thresholds. The threshold curve is derived from these efficiency curves.

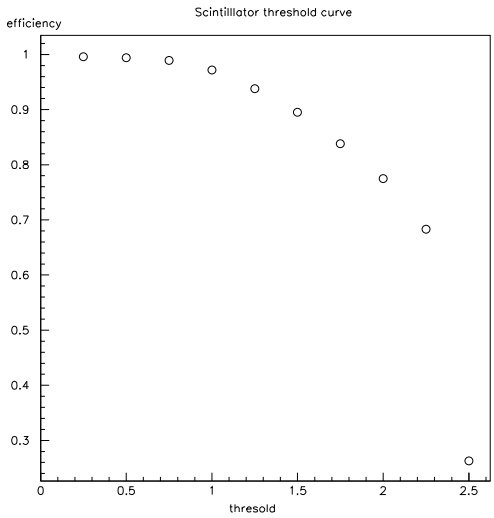

Figure 4.7: Scintillaotr threshold curve.

the figure correspond to high (low) thresholds. When the efficiency is calculated from the efficiency curves, a cut on the high and low ψ was used (15^o and 45^o) to eliminate some of the uncertainties, then the average efficiency is calculated. Fig. 4.7 is our final threshold curve used in our Monte Carlo program.

4.2.6 Cuts in Determining Scintillator Efficiencies

Keeping in mind the strike angle dependence, the scintillator efficiencies measured from experimental and Monte Carlo data are measured with a cut on ψ. Other cuts are also used,

for example, a cut on DPHI of each positron track. The definition of DPHI can be found in § 4.4 when scintillator barrel alignments are studied. All these cuts are applied to reduce the uncertainties in determining scintillator efficiencies. This is part of the effort to reduce the overall systematic errors on ρ. By imposing cuts, some data are thrown away. The loss of statistics is compensated by an improvement of the systematic uncertainties or smaller systematic errors.

- ψ: 15^o - 45^o

  When efficiencies are calcualted, events with strike angle $\psi < 15^o$ and $\psi > 45^o$ are discarded. (30% of the events lost, 20% increase in the statistical error)

- DPHI: 0.2 - 0.7 of a bar width

  We also found that by imposing a cut on DPHI(0.2 - 0.7) (which will be discussed in detail in section 4.4) the measurement of efficiencies can be improved. This is because the confusion near the two sides of a scintillator bar due to uncertainty of track reconstruction is largely eliminated. (30% of data lost, 20% increase in the statistical error).

4.2.7 Scintillator Efficiency Consistency Check

The efficiency consistency check is done to confirm that:
1) the efficiencies used by Monte Carlo program are valid, and
2) the Monte Carlo program does simulate the experiment in generating events and produce the same output (scintillator efficiencies) as seen in data.

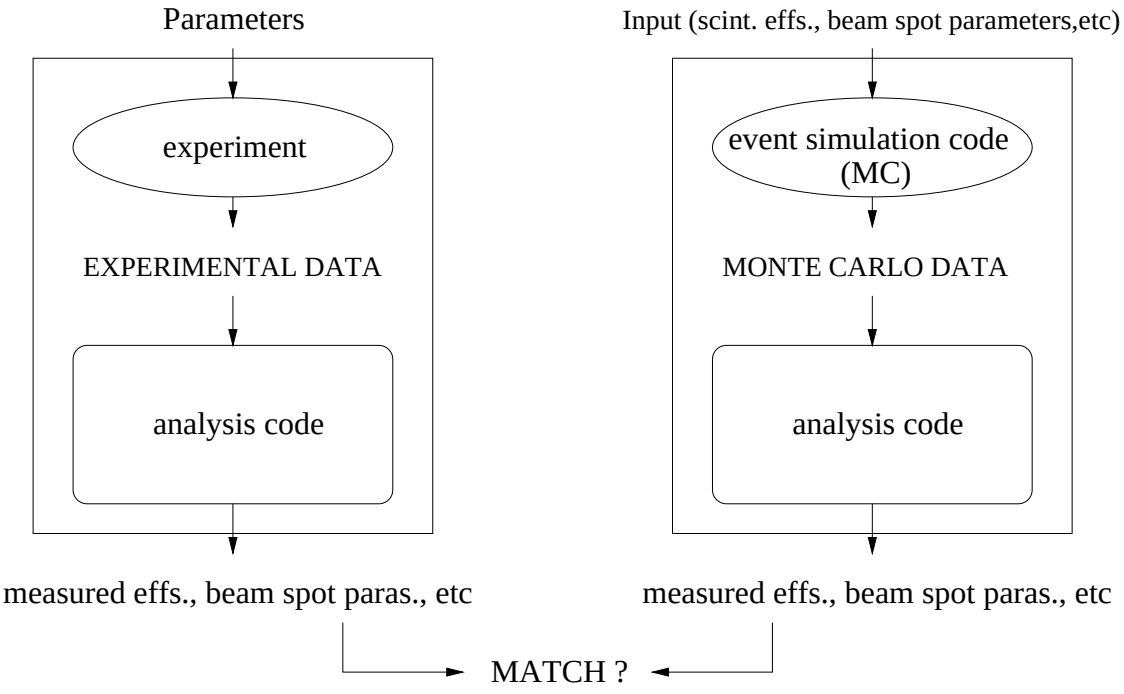

Figure 4.8: A simple diagram of how the measured scintillator efficiencies and other information (beam spot parameters, etc) are used by Monte Carlo program to simulate the experiment and produce results for comparison.

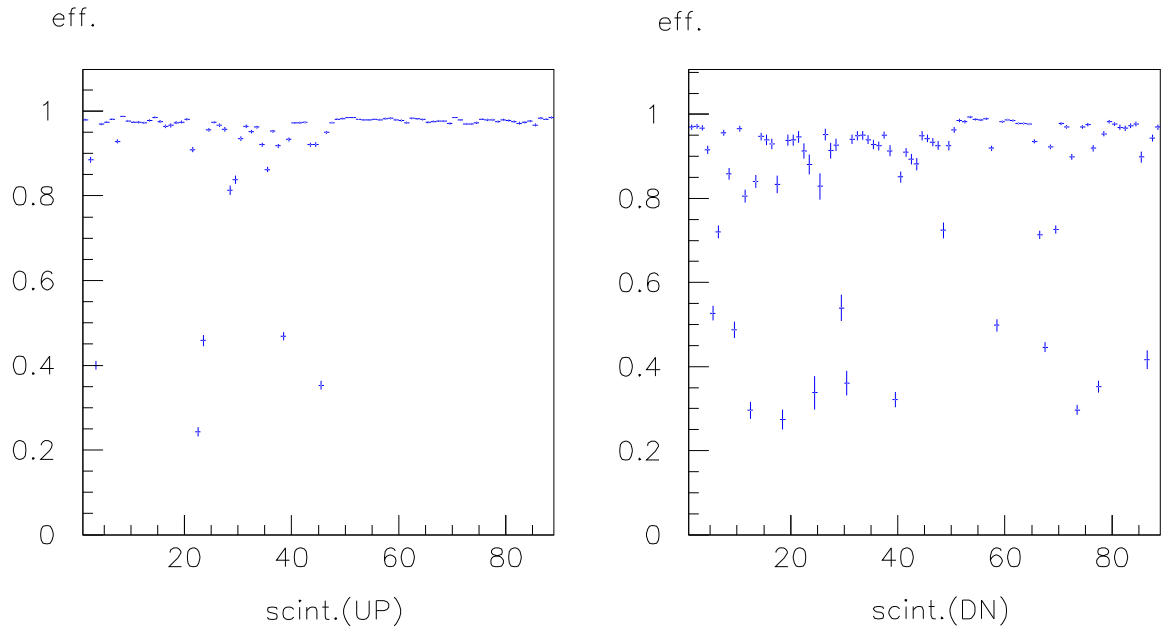

Figure 4.9: The final scintillator efficiencies used in the Monte Carlo program

Originally this check was the comparison between the efficiencies put into Monte Carlo and the measured efficiencies from the generated Monte Carlo data. It was realized later that the more accurate way is to compare the efficiencies measured from Monte Carlo data to that from experimental data. The correct scintillator efficiencies should be those that if used by Monte Carlo these two efficiencies (Monte Carlo and experimental) match.

A more general description of this concept is shown in Fig. 4.8.

This treatment is applied to other measurable parameters of the apparatus that are fed or inputs to the simulation. Each such parameter (scintillator efficiency, beam spot position and profile, etc.) is tuned so that the value in the simulated and real data match.

For some parameters, a converging trial-and-error method is used (e.g., the scintillator efficiencies). For others, special techniques have been developed specifically to derive the

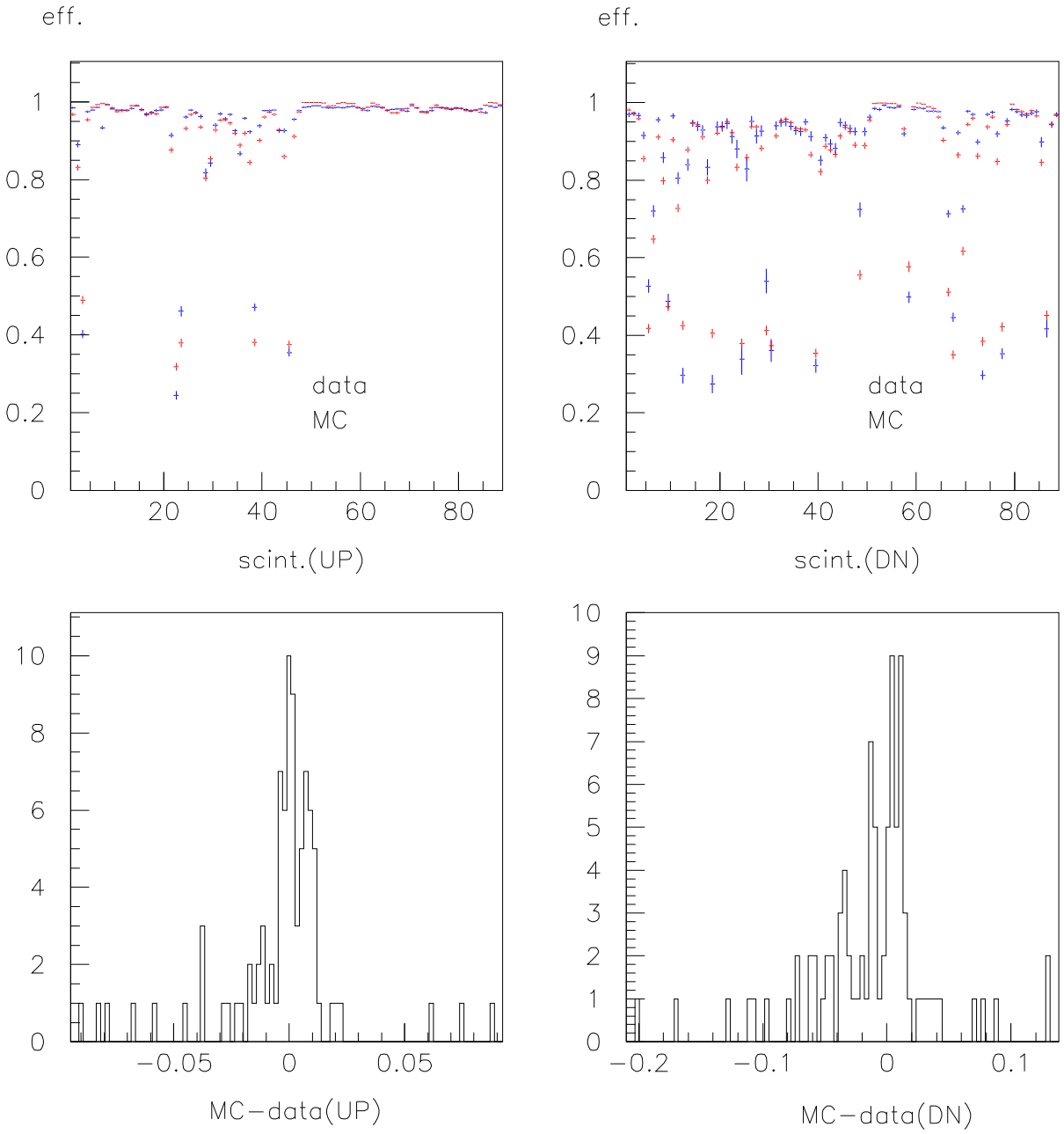

Figure 4.10: Consistency check of the scintillator efficiencies

parameters (e.g., beam spot position and size, chamber cell Lorentz rotation, etc). The discussion of scintillator barrel azimuthal and center alignments in § 4.4 uses a similar approach except that the parameters used by the analysis code to analyze experimental data are adjusted in order to match experimental results to Monte Carlo output.

The results of the final scintillator efficiencies (S2) used in our Monte Carlo program are shown in Fig. 4.9, for upstream and downstream. The consistency check of the efficiencies are shown in Fig. 4.10, in which the upper two plots are the scintillator efficiencies from data superimposed by the efficiencies from Monte Carlo, while the lower two plots show the distribution of the difference. The match is very good.

4.2.8 Efficiency z-dependence

Although each scintillator is 30 cm long along z-axis, the positron tracks mostly populate in the 20 cm range from the target end. A slight z-dependence (non-zero slope of the fitted line in Fig. 4.11) was first found when the averaged efficiency is plotted as a function of DZ, with DZ = 0.0 at the face of the nose cone (or 33 cm from the center of SW coordinate). Note that not all scintillators are aligned at this end, so when efficiency is calculated a fiducial cut at $\pm$34 cm is applied: tracks that strike the barrel within 1 cm from the face of the nose cone are discarded.

We have zeroed in on the z-dependence by a series of divisions of the barrel around the azimuth (Fig. 4.12 and Fig. 4.13) and found that upstream scintillators #34-39 have the largest slope.

In section 4.4.4 we will discuss scintillator z-alignment. Upstream scintillator # 38 is found

to have a very bad z-alignment. This can be the reason why around that region the efficiency is not as uniform along the z-axis as in other regions.

Light attenuation in the scintillator bar may be responsible for this z-dependence. If the positron strikes at target end of a scintillator bar, the scintillation light produced there will have to travel a longer way to get to the light guide, and intensity may be attenuated along the way, and therefore the efficiency near the target end is lower. We have plotted scintillator ADC pulse height vs. DZ in Fig. 4.14. We can see that scintillator #38 (UP) has a very different pulse height distribution, and there is a sudden cut off of the ADC pulse height at around 60.

The conclusion from the above study is that the scintillator z-dependence is localized in a narrow region. Scintillator #38 will be excluded in the final extraction of ρ.

4.3 Chamber Wire Efficiencies

There are 288 anode wires in each of the seven dwarf chambers and 540 in Snow White, a total of 2556 anodes in the overall chamber system. With 128 inner and 128 outer cathode stripes in each of the seven dwarf chambers for both upstream and downstream, and 224 inner and 224 outer cathode stripes in Snow White, upstream and downstream, there are a total of 4480 cathode stripes. Like the scintillator efficiencies, chamber wire efficiencies are directly related to the measurement of the Michel parameter, and the precision with which they are determined affects the overall systematic error of ρ. In this experiment, the requirement on the precision of the measurement forced us to examine the chamber wire performance on a wire by wire basis rather than the average of some sort on a layer or in a

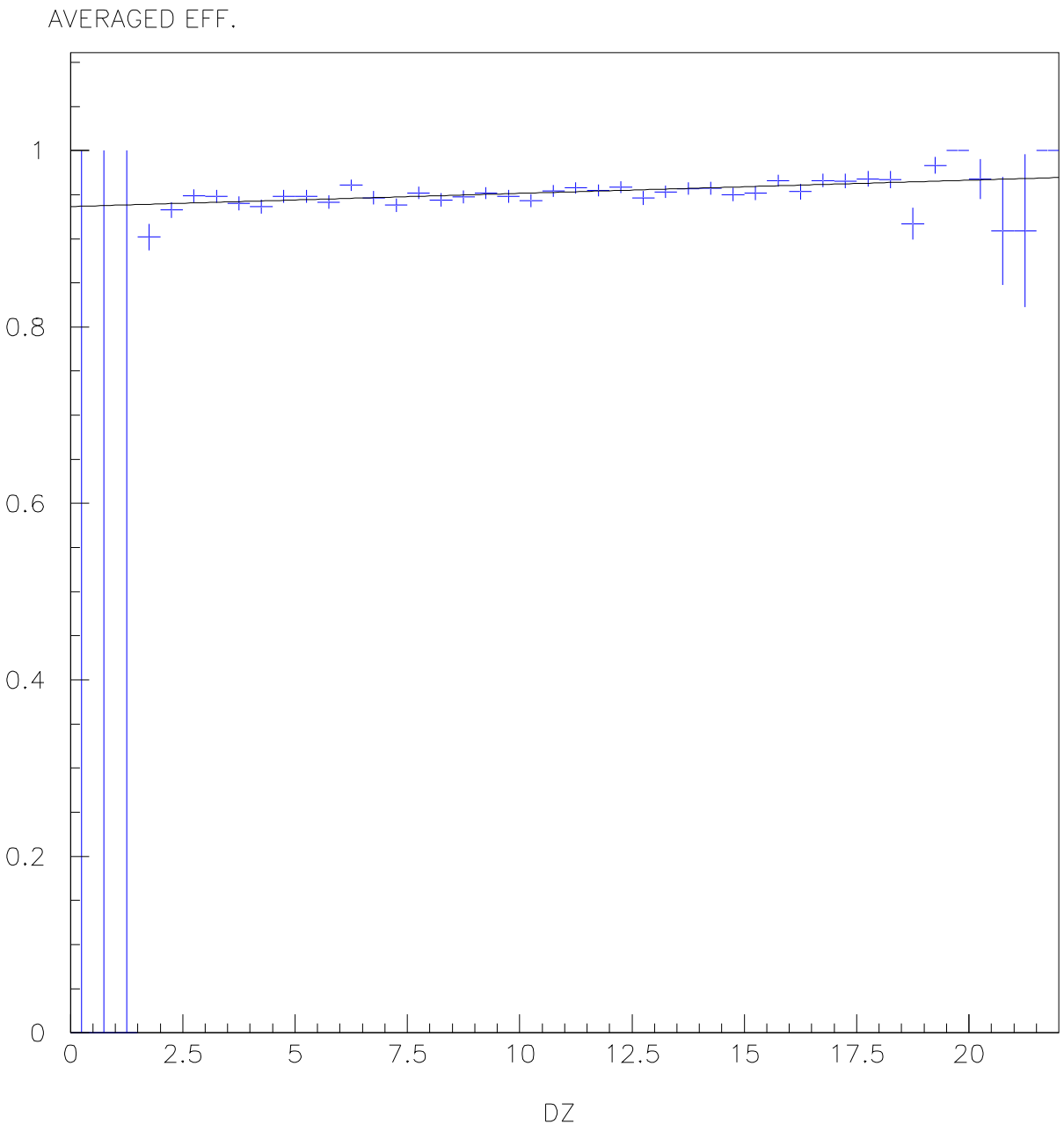

Figure 4.11: Averaged scintillator efficiency (upstream) vs. z

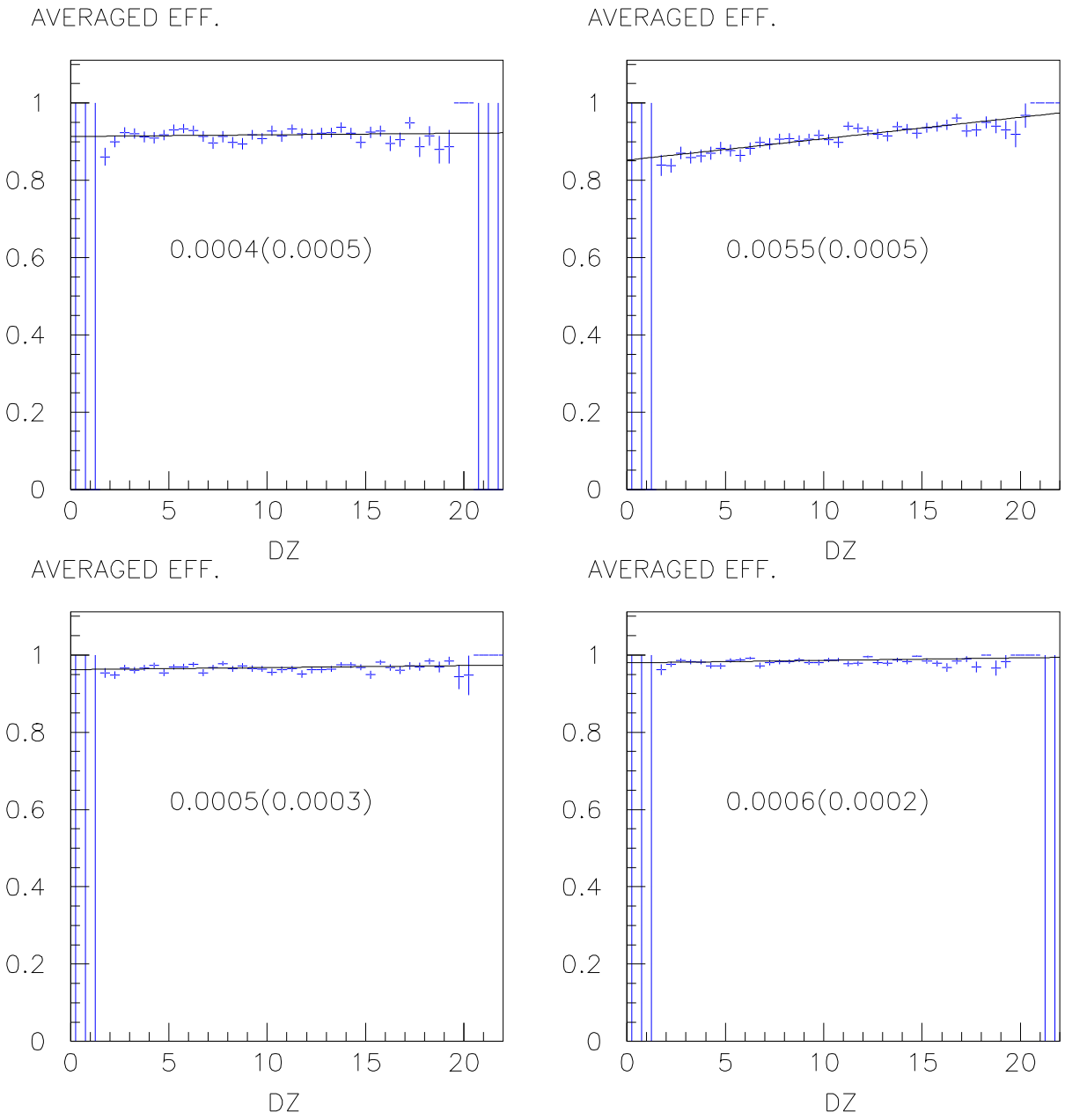

Figure 4.12: Averaged scintillator efficiency vs. DZ in four quadrants on the endview of the barrel. The numbers in each plot are the slope of the fitted straight line and its error. DZ: the z coordinate starting from ±33 cm from the target.

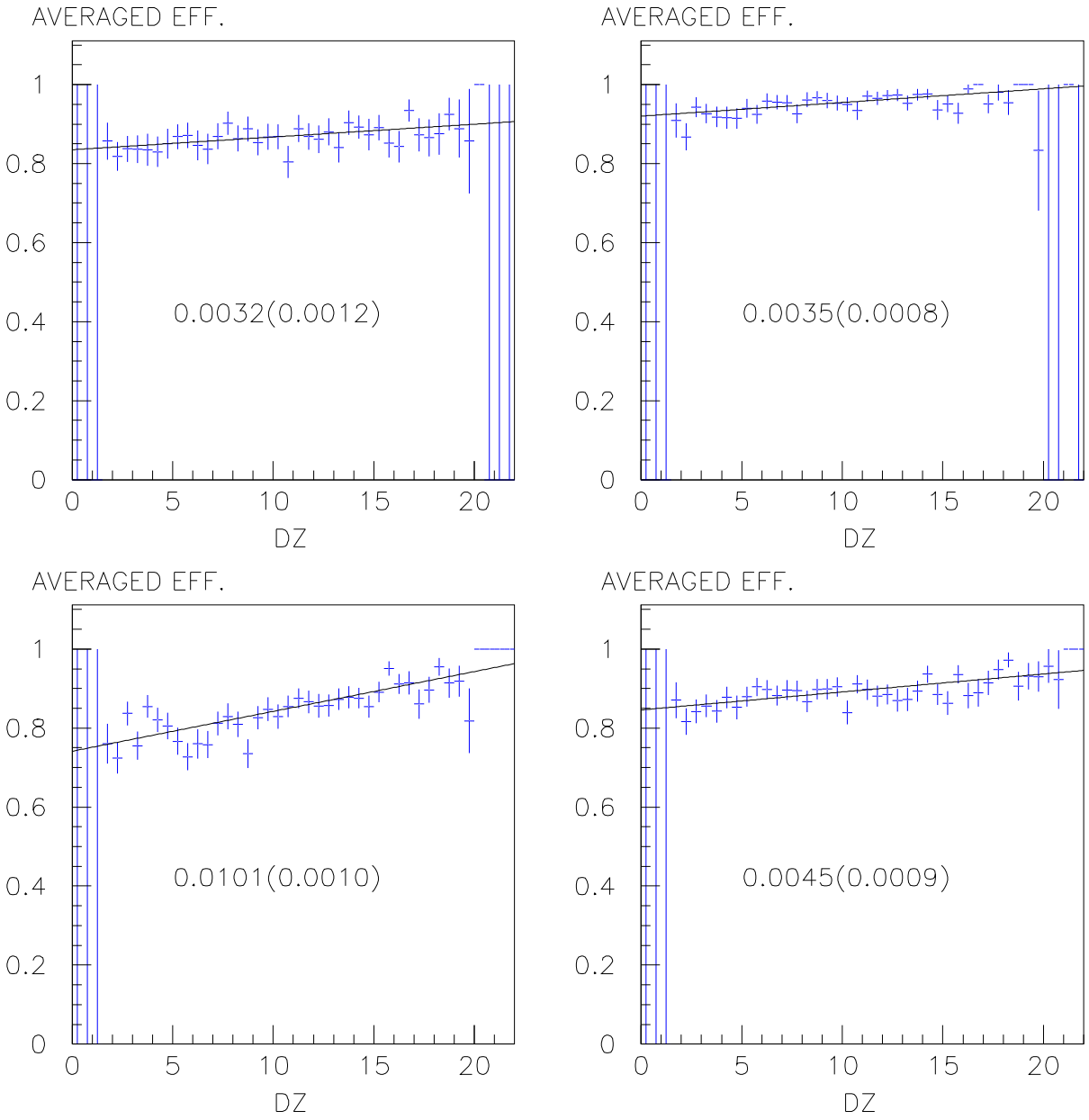

Figure 4.13: Averaged scintillator efficiency vs. DZ in the four evenly divided sections in the second quadrant. Slopes of the fitted straight line and their errors are also shown in each plot.

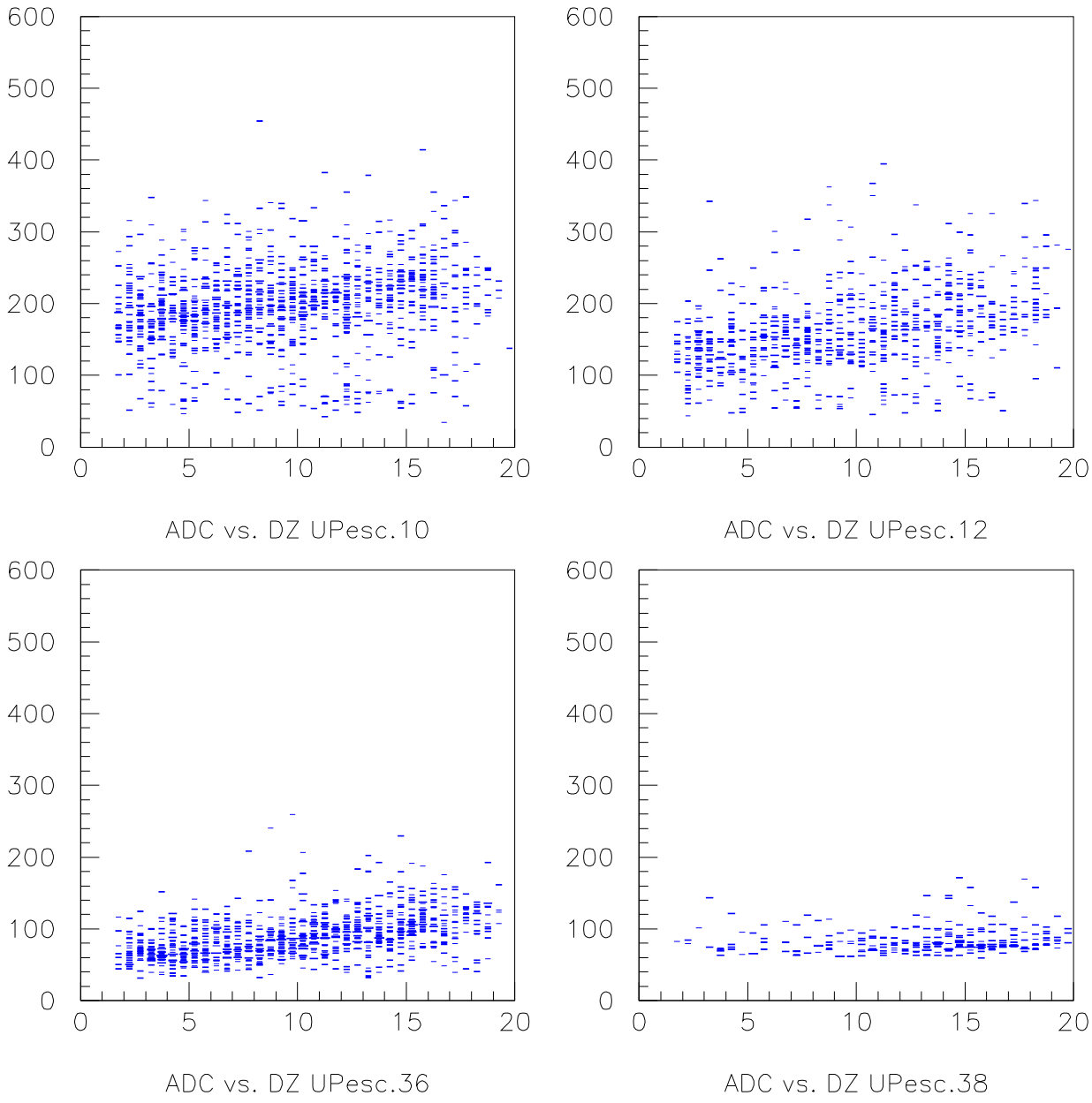

Figure 4.14: Scintillator ADC pulse height vs. DZ for four scintillators.

chamber. These efficiencies are then converted to corresponding thresholds and then used in our Monte Carlo program to re-produce the measured efficiency. In order for the data and Monte Carlo to match, all factors that could affect the gain on the wire should be included in the Monte Carlo. Dealing with 7000 wires is an extremely difficult task. There are various mechanisms, geometrical, physical or operational, that can alter the performance of certain wires or groups of wires, and the wire efficiencies derived by the staightforward way from data in ONE step provided just an estimate of the evaluation. All the differences that were seen in the output of Monte Carlo simulation using the thresholds from previous steps were examined carefully and transformed into additional mechanisms integrated into Monte Carlo in the next step. The task of matching Monte Carlo to data involved years of hard work and numerous trials, twists and turns, failures and successes. The result still has not met our original goal. This difficulty may have its origin in the large amount of degrees of freedom and the unwanted, unexpected correlation between different elements, for example, between anodes and cathodes, between chamber wires and other parts of the detector system, and this has limited our ability to determine the finer details and obtain the precision as desired.

4.3.1 How Chamber Wire Efficiencies are Measured

The chamber wire efficiency is measured in the same way as the scintillator efficiency [**?**]: if the reconstructed positron track (reconstructed by hits in other chambers) crosses a wire and the wire registers a hit, then it is efficient. The efficiency of the wire is then calculated as the ratio of the number of times the wire registered a hit to that of the total number of reconstructed tracks. In reality, however, a more practical way is to use a ± 5 wire window to calculate the efficiency. Any wire in the window registering a hit implies an efficiency of

the wire in the middle of the window. Just as in the scintillator efficiency case, 1-loop events were used in calculating the wire efficiencies because we use the 1-loop spectrum to extract ρ.

In the study of wire efficiencies we realized that we need to break the positron tracks into incoming and outgoing (relative to the chamber) and calculate efficiency for each case separately. Here incoming refers to those tracks that cross the chamber from outside of the cylindrical surface towards the target and outgoing the opposite direction. The usage of the this classification becomes obvious when the Lorentz rotation of chamber cells is examined, as described in the following subsection.

4.3.2 Lorentz Rotation of Chamber Cell Boundaries

When a positron track strikes an anode cell of a chamber, more than one wire can fire. If the track strikes at normal incidence it should fire the least number of anodes, i.e., the anode cluster width should be at minimum. See Fig. 4.15(a). But when we plot cluster width vs. incident angle (for data), we find that this is not the case. The minimum cluster width appears at an angle far from normal (90^0). See the data curves in Fig. 4.16. The magnetic field in which the chambers are placed is responsible for this: the ionization electrons are subject to an $E \times B$ Lorentz force as they drift to the anode wires. This force deflects the tracks of ionization electrons and effectively tilts the cell boundaries. See Fig. 4.15(b). This angle is therefore called Lorentz angle $\eta_{Lorentz}$ and should be extracted from data and put into Monte Carlo in order to correctly simulate the chamber performance. In Fig. 4.16 the Monte Carlo curves are without a Lorentz angle, which is why the data and Monte Carlo curves do not match.

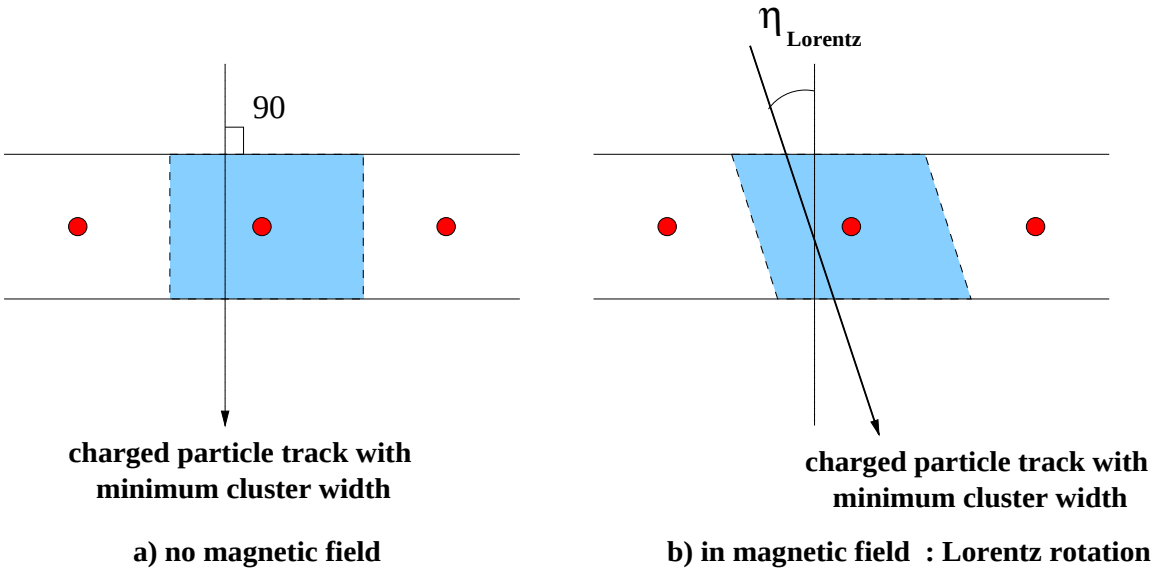

Figure 4.15: Chamber cell orientations: Lorentz rotation in the presence of magnetic field. The rotation is denoted by $\eta_{Lorentz}$, the Lorentz angle. Dots: anode wires; horizontal lines: outer and inner cathode planes

To extract $\eta_{Lorentz}$, we fit the data curves in Fig. 4.16 with a cubic polynomial $y = P_1(x - P_2)^2 + P_3(x - P_4)^3$, where y is the mean cluster width, x is the incident angle, and P_1, P_2, P_3 and P_4 are parameters to be fitted. The angle that corresponds to the minimum cluster width, X_0, is found by taking the derivative $\frac{dy}{dx} = 0$.

We have repeated the same procedure for all seven chambers. The results are in Table 4.2. The conclusion is:

- the average (excluding dwarf 6 because of its operational problem) X_0 is -14.59^o for incoming case and -11.82^o for outgoing case.
- the spread of X_0 among the chambers is about 3^o
- there is no strong correlation between X_0 and high voltage

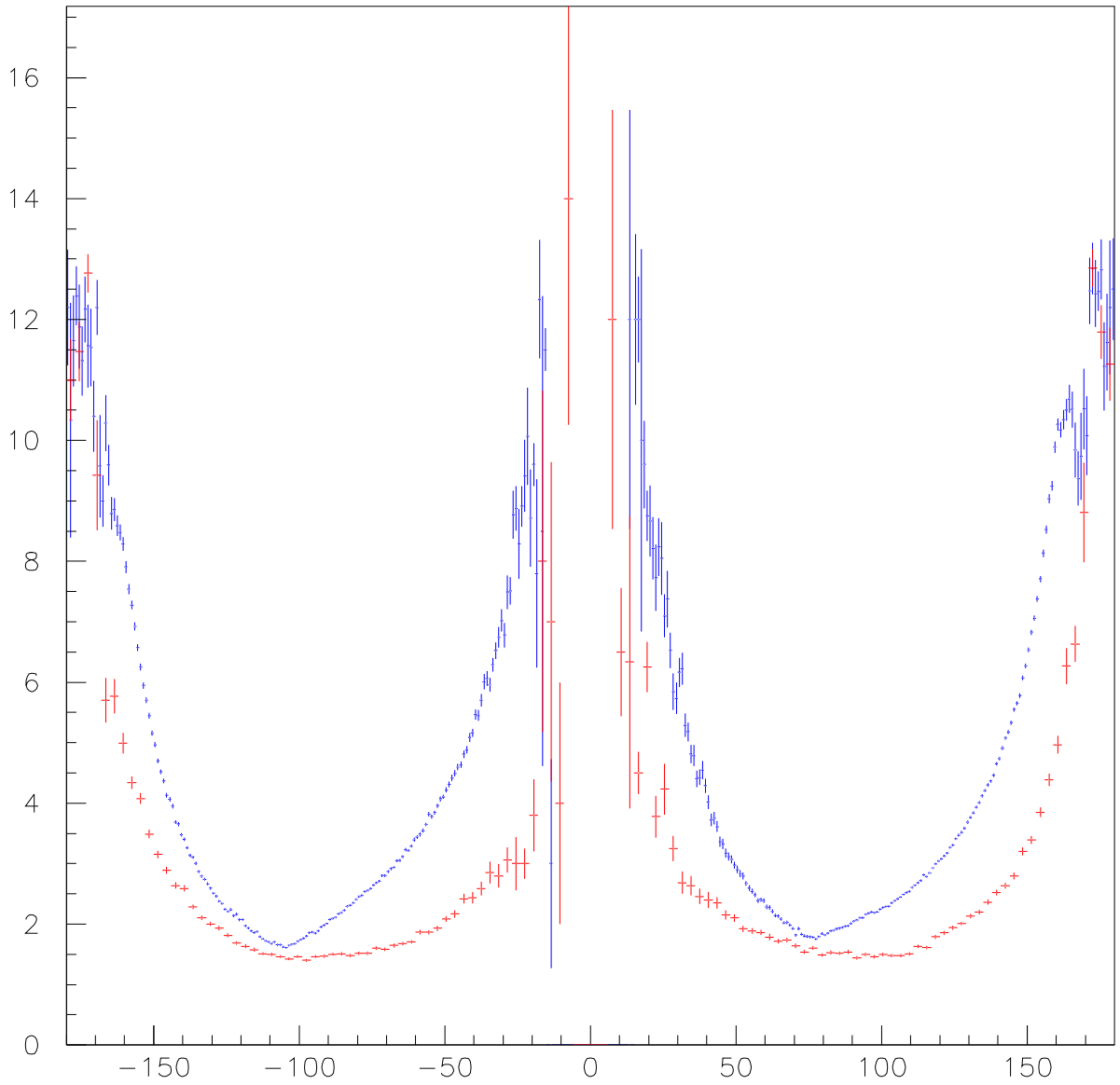

Figure 4.16: Mean anode cluster width vs. chamber strike angle. Data (upper two curves) and Monte Carlo (lower two curves) are compared. The chamber strike angle is defined in such a way that $\pm 90^o$ is for normal incidence. Positive angles correspond to incoming tracks and negative angles correspond to outgoing tracks.

Table 4.2: The angle corresponding to minimum mean cluster width in all seven chambers, from data. Angles are all in degrees. Because of the noise we have seen in Dwarf 6, its X_0 is not included in calculating the average X_0.

chamber	X_0 (incoming)	X_0 (outgoing)	High Voltage(V)
dwarf 1	-13.26	-9.75	2025
dwarf 2	-16.09	-10.92	2250
dwarf 3	-14.02	-13.35	2250
dwarf 4	-14.61	-9.83	2200
dwarf 5	-15.74	-13.66	2250
dwarf 6 *	-6.09	-7.73	(excluded)
dwarf 7	-13.08	-13.44	2200
Average X_0 (without dw6)	-14.59	-11.82	

Table 4.3: Monte Carlo results for three different input angles of cell Lorentz rotation. By interpolation this gives $\eta_{Lorentz} = -16.3$ for $X_0 = -14.59$.

Input angle (degree)	x_0 (degree)
-12.0	-10.3
-16.0	-14.3
-20.0	-18.3
$\eta_{Lorentz} = -16.3$	$X_0 = -14.59$

- the difference between incoming and outgoing X_0 is almost 3^o

It is important to note that $X_0 = -14.59^o$ (for incoming case) is not the Lorentz angle we should put into Monte Carlo. It is $\eta_{Lorentz}$ that should be put into Monte Carlo to get $X_0 = -14.59^o$ by fitting Fig. 4.16 as the outcome. To get the value of $\eta_{Lorentz}$ we have run Monte Carlo simulations with three different input angles (arbitrary), fit corresponding Fig. 4.16 for all chambers the same way and get their corresponding x_0s, the average of the six chambers. (Note that x_0s are the fitting result from the Monte Carlo, while X_0s are from the data, and $\eta_{Lorentz}$ is the parameter that will be used by the Monte Carlo). The results are listed in Table 4.3. It is for incoming case only, which should be sufficient. By linear interpolation we find $\eta_{Lorentz} = -16.3^o$. This is the number we use as the Lorentz angle in our Monte Carlo program. The reason for the difference between $\eta_{Lorentz}$ and X_0s, is due to the combination of all other factors in the apparatus that can affect this rotation angle, and which have already been included implicitly in the Monte Carlo program. After using $\eta_{Lorentz} = -16.3^o$, the mean cluster width distribution of Monte Carlo agrees surprisingly

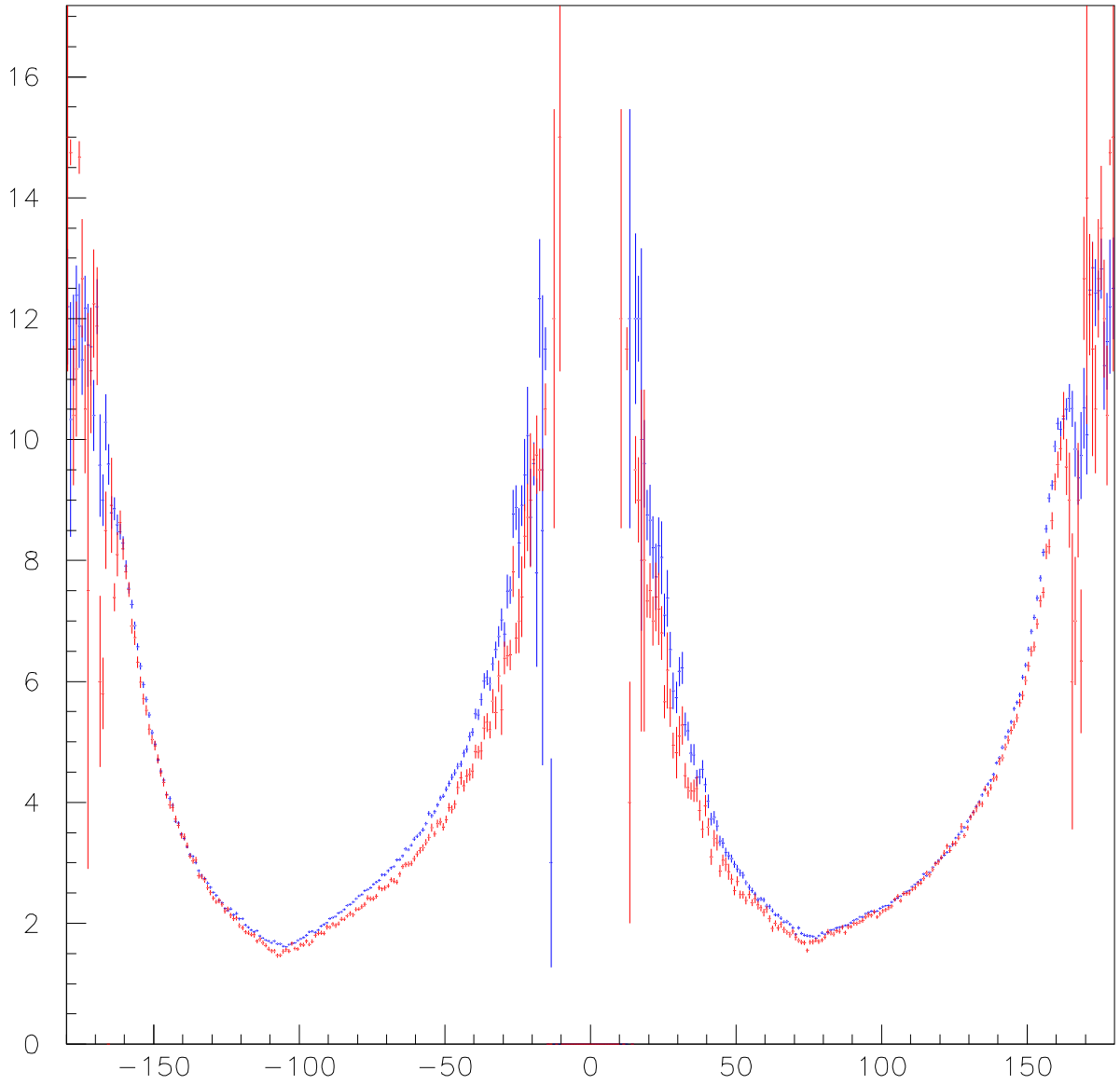

Figure 4.17: With the Lorentz angle $\eta_{Lorentz} = -16.3^o$ put into Monte Carlo, the mean cluster width distribution now agrees better with data.

Table 4.4: The parameters needed to calculate Lorentz angle

Parameter	value
V (drift velocity)	12 cm/μs
l (half gap)	0.1778 cm
s (anode pitch)	0.13 cm
d (anode diameter)	0.0015 cm
B (magnetic field)	15KG
E (electric field)	12.4 KV/cm

well with data. See Fig. 4.17.

A theoretical estimation of the Lorentz angle on our chambers was done as in the following:

It was shown that this angle η_L can be expressed as [**?**]:

$$\tan(\eta_L) = C_B \times V_E \times \frac{B}{E} \tag{4.5}$$

where B and E are the magnetic and electric fields, V the drift velocity of ionization in the chamber gas mixture, and C is the capacitance which is calculated as:

$$C = \frac{2\pi\epsilon}{\frac{\pi\ell}{s} - \log\frac{\pi d}{s}} \tag{4.6}$$

The value (and the units) of those parameters can be found in Table 4.4.

The Lorentz angle calculated from this is about 15^o, in good agreement with the above extraction from the data.

4.4 Scintillator Barrel Alignments

We discuss the scintillator barrel alignments using the Snow White (SW) coordinate frame in which the positron tracks are reconstructed: its axis being z-axis ; the midpoint on its axis the origin (0,0,0); and, in endview plane, from (0,0) to anode wire # 1 being the x-axis. As described in Chapter 2, the scintillators are closely packed into two cylindrical barrels: upstream and downstream. Ideally, the two scintillator barrels should have their centers on the z-axis with scintillator #1 having its low phi edge lined up with the x-axis. However, in the study of track population in the scintillators we found that the barrels are slightly rotated in azimuth and off in their centers. In the next two subsections details of the procedures used to obtain azimuthal angle offsets and barrel center offsets will be described. We will also show when the derived offsets are included in the analysis, data and Monte Carlo agree much better. The residual difference is the indication of another source of misalignment.

A very useful quantity used in the discussions is DPHI, which is defined in Fig. 4.18 and illustrated in Fig. 4.19. DPHI gives a measure of the track population in azimuth in scintillators.

4.4.1 Barrel Azimuthal Alignment

In the first plot in Fig. 4.20, two curves of DPHI distribution are plotted: one is from data, analyzed with no barrel azimuthal offset and with center at (0,0); the other is from Monte Carlo in which the same geometry is used in generating and analyzing events (i.e. there is no offset problem) and should serve as the guidance in deriving the correct offsets in data. The vertical axis is the number of tracks in arbitrary units and the abscissa is DPHI. The

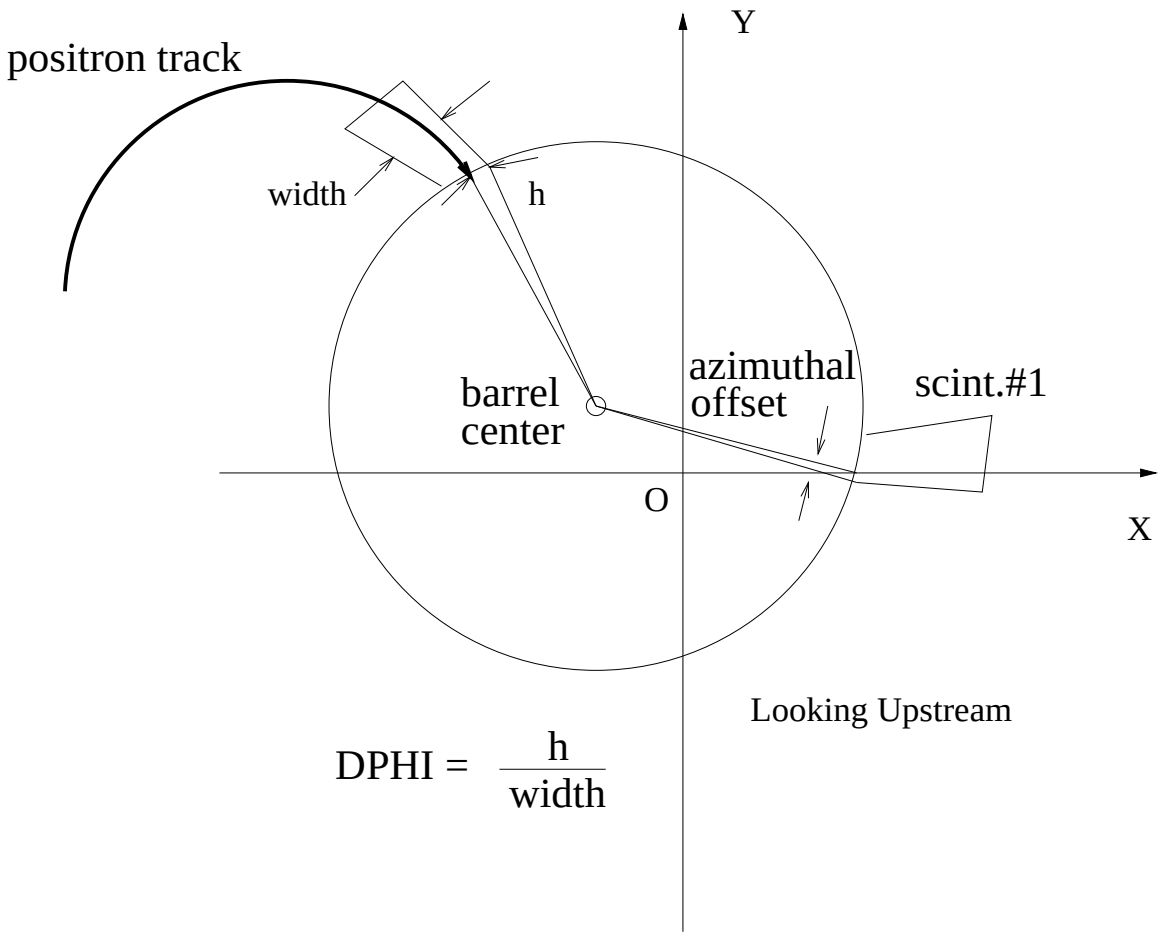

Figure 4.18: Definition of DPHI

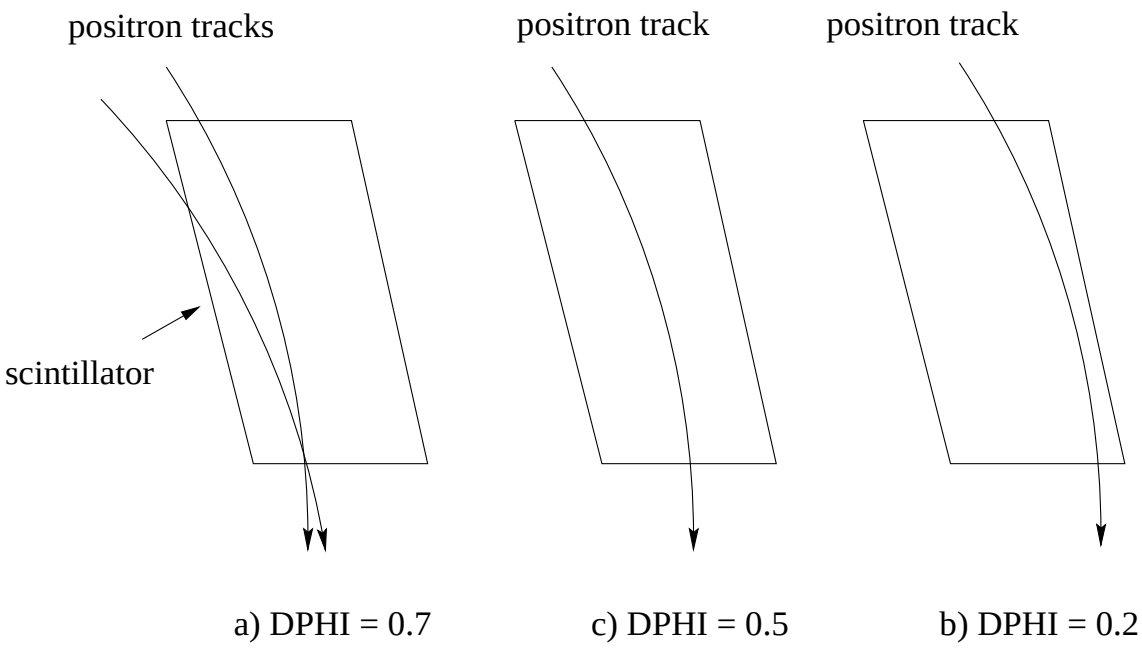

Figure 4.19: Tracks with different DPHI values

shape of the curve shows in general how tracks populate scintillators in azimuth. The shape of the curve and the DPHI value corresponding to the peak of the curve (peak DPHI value) give the distribution of track population in all 87 scintillators.

The particular geometry of the detector system and the positron decays gives the observed shape of the Monte Carlo curve in the first plot of Fig. 4.20. The peak DPHI value of that curve is 0.42 by polynomial fit. This indicates that an analysis of experimental data with the correct azimuthal angle offset (if there is any) should yield peak DPHI = 0.42. Obviously the data curve in Fig. 4.20 which is obtained with default alignment (i.e., no azimuthal angle offset) does not yield 0.42. This tells us that in reality the barrel is not aligned perfectly in azimuth. We should include the correct angle offset in our analysis and only then will we get the curve that resembles the Monte Carlo curve.

The procedure to find the correct angle offsets is the following: the data are analyzed with

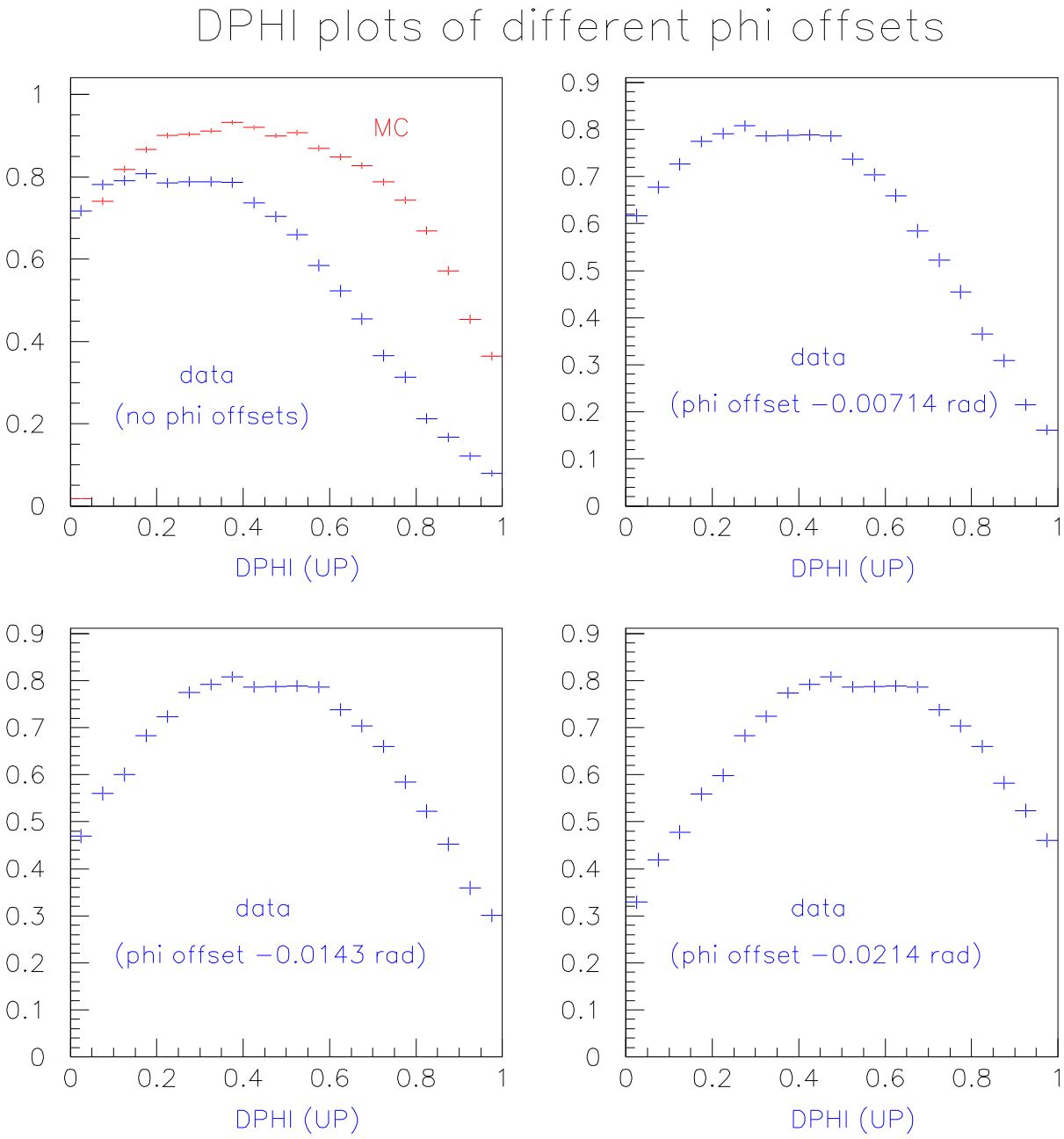

Figure 4.20: DPHI distribution within a scintillator width, averaged over all scintillators. The first plot shows the disagreement between data and MC if no phi offset is assumed in analyzing data.

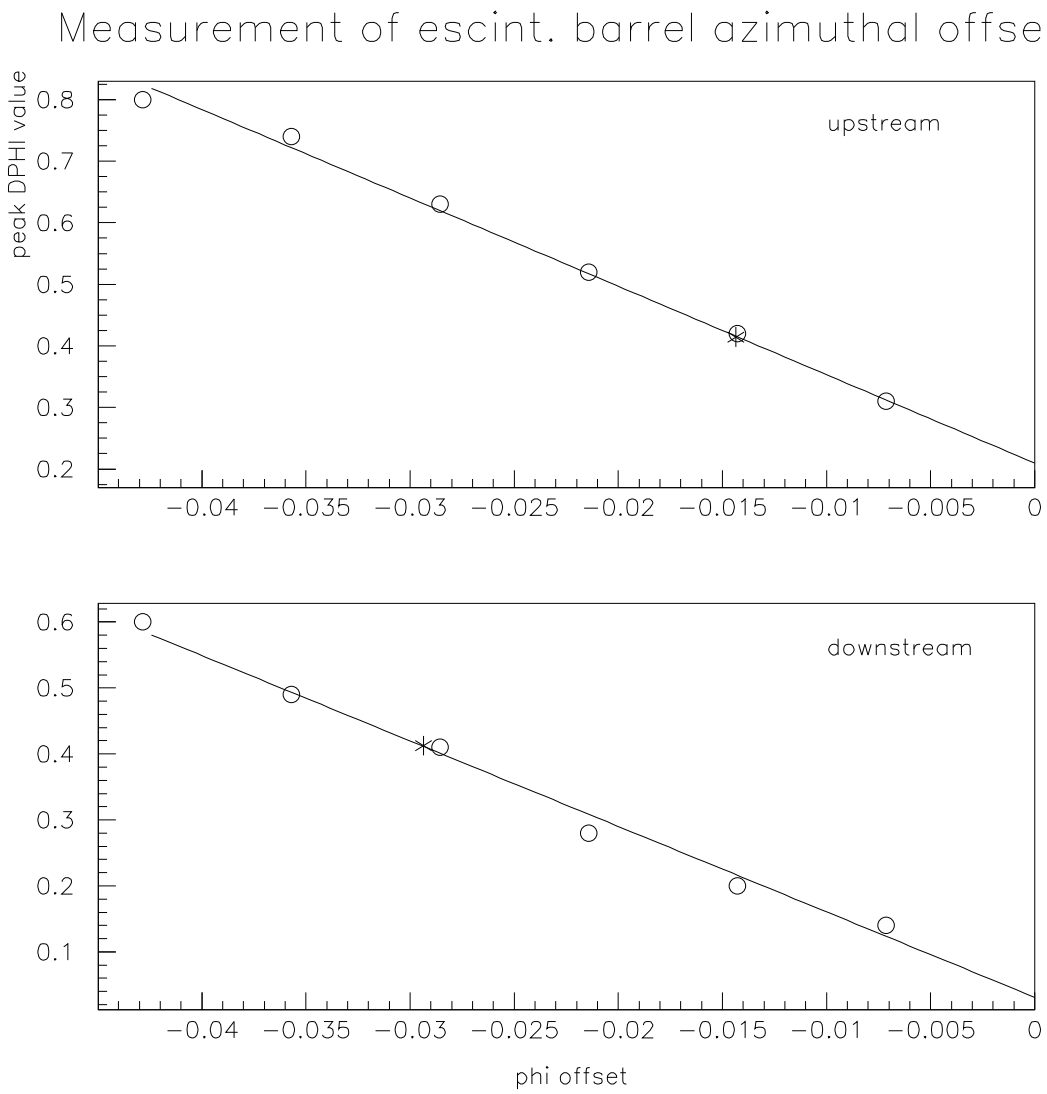

Figure 4.21: Result for barrel azimuthal alignment: by interpolation to MC value the offset is found for upstream and downtream

different (and exaggerated) angle offsets (for upstream and downstream separately), the curve shifts to the left or right due to an overall artificial rotation of coordinate frame around azimuth which shifts the angular track population. Three such cases are shown in the last three plots in Fig. 4.20. Then we take the peak DPHI value for each case and plot it versus the corresponding angle offset used. Six points were taken and they are fitted linearly, shown in Fig. 4.21. The correct angle offset is then the angle that corresponds to DPHI equal to 0.42. It is -0.014 rad for upstream and -0.03 for downstream. Note that each scintillator has a width (bar width) of 0.0714 rad, or 4 degrees. So the angle offsets are between one fifth and two fifths of a bar width.

The final values can be found in the table at the end of the next subsection.

4.4.2 Barrel Center Alignment

Similar to scintillator barrel azimuthal alignemnt, for center offsets we first have plotted two curves, data (with the assumption that center is perfectly aligned) and Monte Carlo, to see if they match or not. These two curves are not the same as the ones used in the previous subsection. They are the weighted average DPHI of the scintillator distributions in each scintillator vs. scintillator number. They show how the weighted average DPHI values change around the azimuth, which is related to the alignment of the center. Obviously the two plots in Fig. 4.22 do not match. This is a sign that the assumption that barrel centers are perfectly aligned along the Snow White z-axis is not correct. A sine wave-like profile of such a plot, as seen for data in Fig. 4.22, is a clear indication that the center is off. Just as in the previous subsection, if we can find the correct center offsets and use them in the analysis of data, we should make the Monte Carlo curve match the data curve.

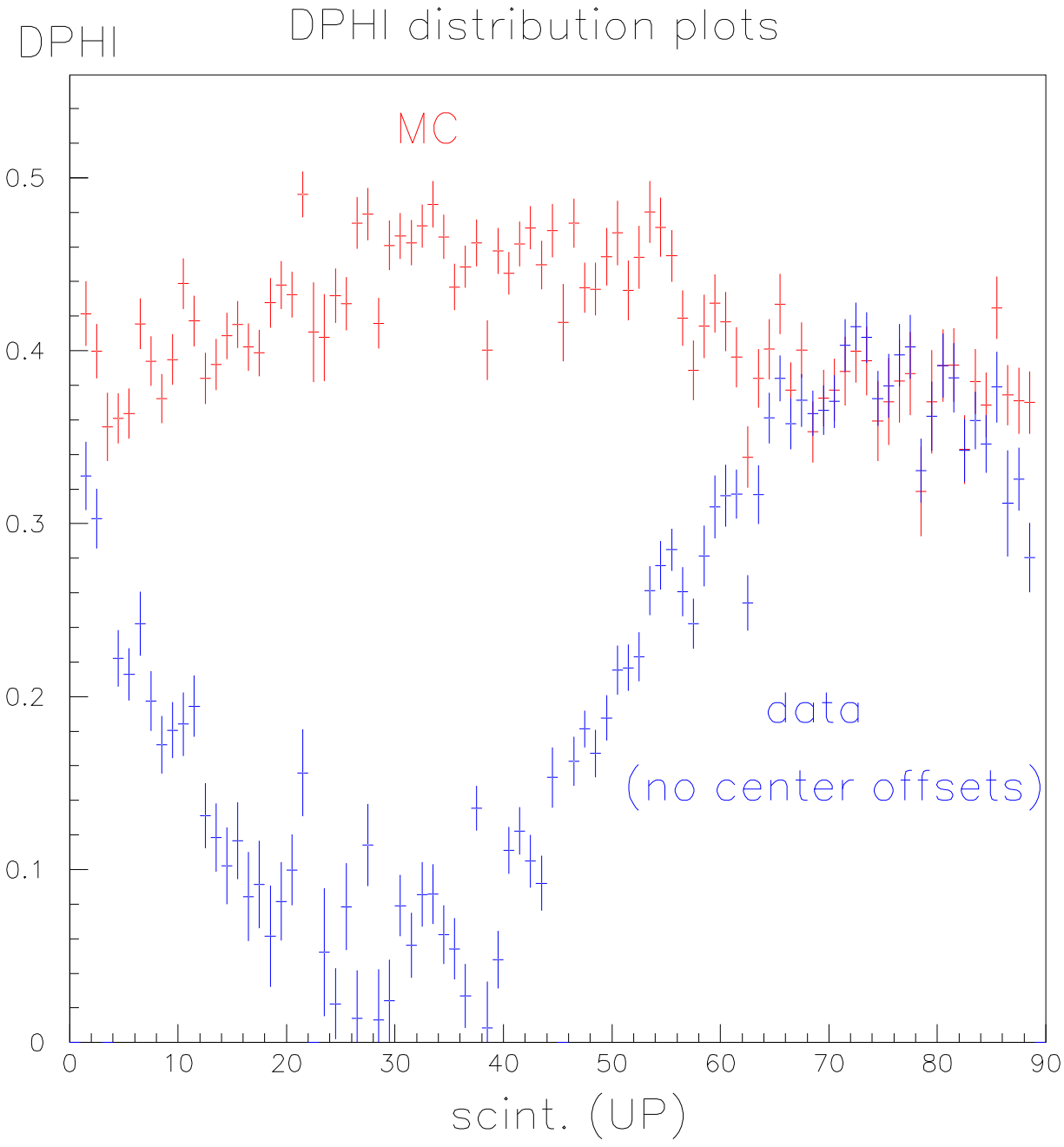

Figure 4.22: Profile plot of DPHI vs. scintillator, showing large disagreement between data and Monte Carlo. Data are analyzed with center at (0,0).

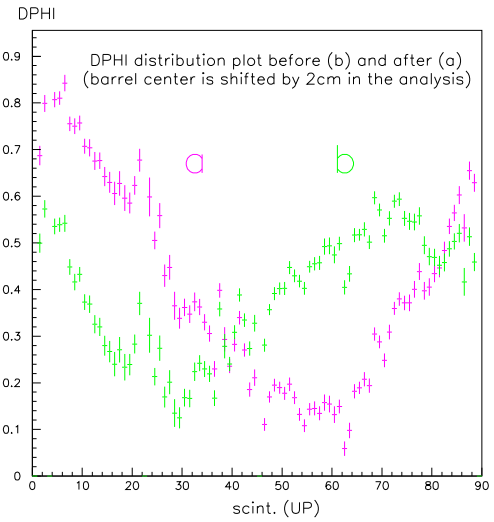

Figure 4.23: DPHI plot before (b, in green) and after (a, in purple) a shift of barrel in x of 2 cm in analysis. The net change a-b due to the shift is shown in the next figure.

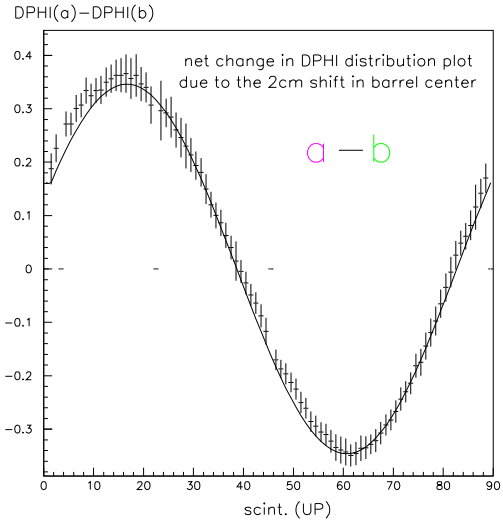

Figure 4.24: The net change of DPHI by shifting barrel in x-axis by 2 cm (from the previous plot), fitted nicely with a sine function.

The procedure to find the center offsets involves the following steps:

- Analyze data assuming perfect center alignment (with centers at (0,0)). This is already shown in Fig. 4.22. Then fit the plot with Asin(ϕ_{sc})+ Bcos(ϕ_{sc}), where ϕ_{sc} is the azimuthal coordinate of each scintillator, and A and B are amplitudes.

- Analyze data with center of barrel at (2,0),(-2,0),(0,2),(0,-2) (all in unit of cm). It is expected that the curve of interest (like the data curve in Fig. 4.22) is shifted in abscissa. An example is shown in Fig. 4.23 for the shift of center from (0,0) to (2,0). The **net change** of the curve (curve a minus curve b), due to the shift of the barrel

Table 4.5: Scintillator barrel offsets

Scintillator Barrel	Offsets
Azimuth: upstream/downsteam	-0.014/-0.030 ±0.0036 rad
Barrel center: upstream x	0.06 ±0.01 cm
upstream y	0.10 ±0.01 cm
downstream x	0.17 ±0.01 cm
downstream y	-0.05 ±0.01 cm

center, is sinusoidal. It is fitted with Csin(ϕ_{sc}). For a shift in y the net change of the curve is fitted with Dcos(ϕ_{sc}). When the same is done to all the four cases, a simple relation between the shift in x (or y) and the amplitude D (or C) is established. Note that it is the **net change** of the curve that corresponds to the shift in x or y, not the curve itself after the shift.

- Interpolate the above relation and get the shift (X_B,Y_A) that corresponds to the fitted amplitutes A and B. The center offset is then (-X_B,-Y_A).

- Analyze data again, this time with (-X_B,-Y_A), we get the curve in Fig. 4.25. It is compared to Fig. 4.22. The wave part in data is gone and data and Monte Carlo agree very well, indicating we now have a good estimate for the barrel center offset.

Note that the azimuthal and center alignment are correlated. We have iterated the two processes, and the numbers converge after two iterations. The final results for the angle and center offsets are shown in Table 4.5.

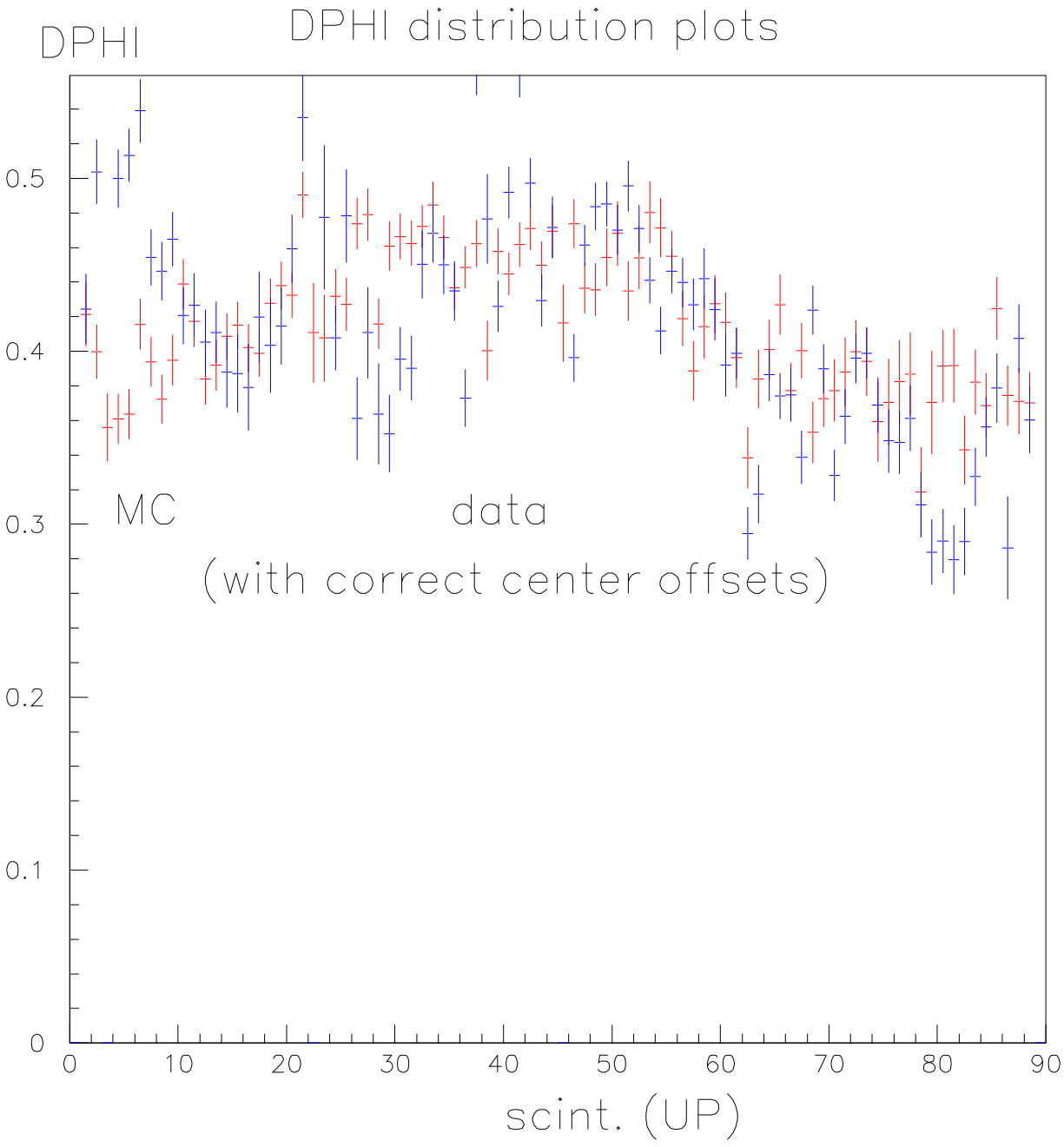

Figure 4.25: With the correct barrel centers in analyzing data, data and Monte Carlo agree much better now, compared to Fig. 4.22.

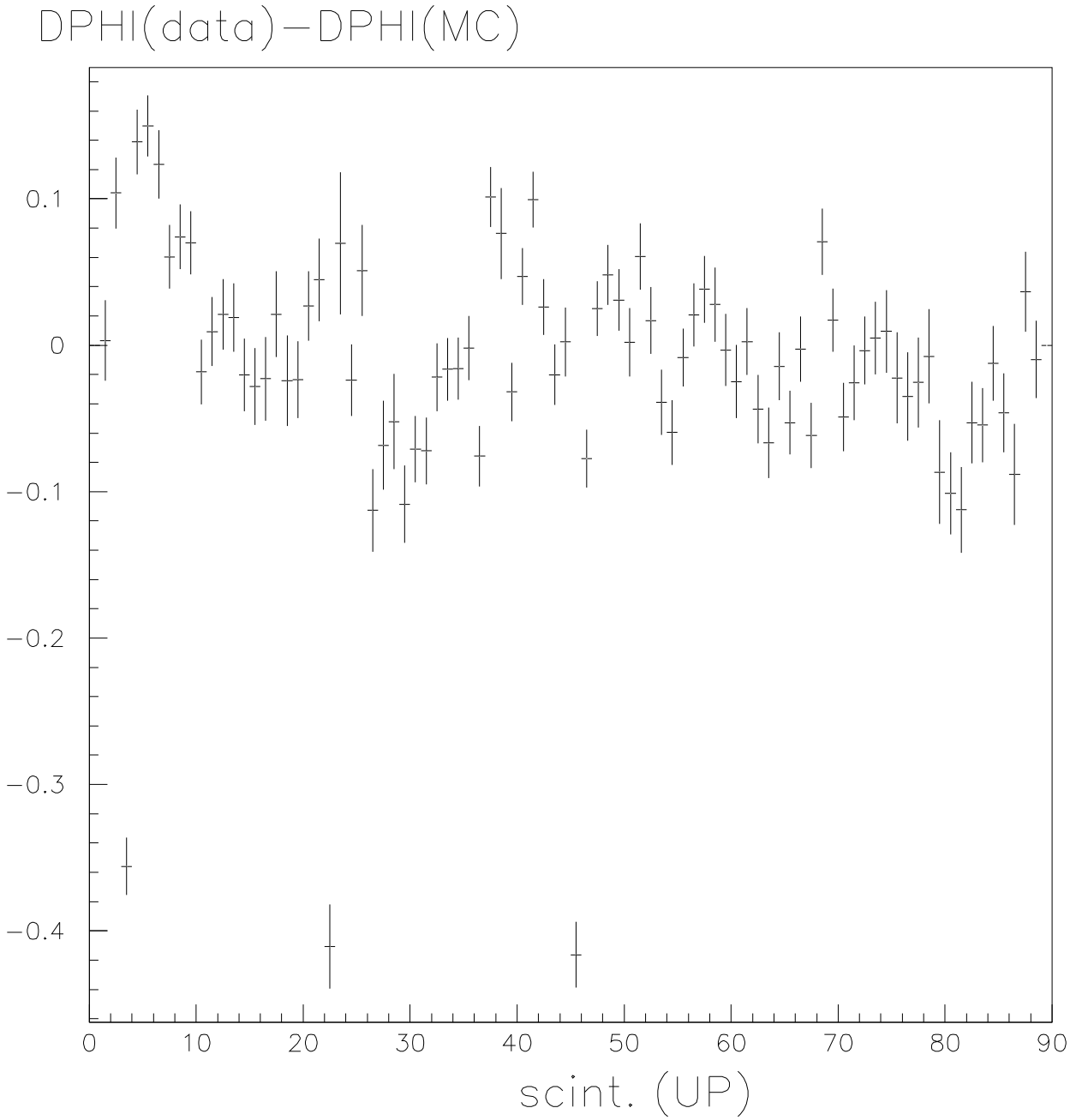

Figure 4.26: The residual difference between data and Monte Carlo from Fig. 4.25.

Also note that there is still some fluctuation left on each scintillator. See Fig. 4.26. A possible cause of this residual fluctuation is discussed next.

4.4.3 Scintillator Uneven Spacing

When 87 scintillators (and 1 hole for gas line) were put together to form a cylinder, there was some space between adjacent scintillators. The scintillators may have shifted slightly since they were originally installed, and this causes an uneven spacing between them. If 4.2.1 and 4.2.2 are done correctly and there is still fluctuation (of DPHI) on each scintillator in Fig. 4.22 then the fluctuation may have come from this uneven spacing. If there are no other sources contributing to the mismatch between data and MC in Fig. 4.22 then the difference between MC and data, Fig. 4.26, is the actual distribution of scintillator uneven spacing. Of course, if the precision in doing 4.2.1 and 4.2.2 is no better than the effect of uneven spacing, then the error being carried over may cause some non-physical effect, i.e., some scintillators overlap slightly. Since this happens to only a few scintillators, the impact of this to our analysis is negligible.

4.4.4 Scintillator z-alignment

Another scintillator alignment we need to check is whether scintillators are aligned along z-axis. See Fig. 4.27.

The plot that is used to check this alignment is DHPI vs. DZ. Fig. 4.28 is an example. Here DZ is the same as the DZ in section 4.2.8. We have made the plot DPHI vs. DZ for each scintillator (upstream and downstream) for DZ from 0 to 20 cm.

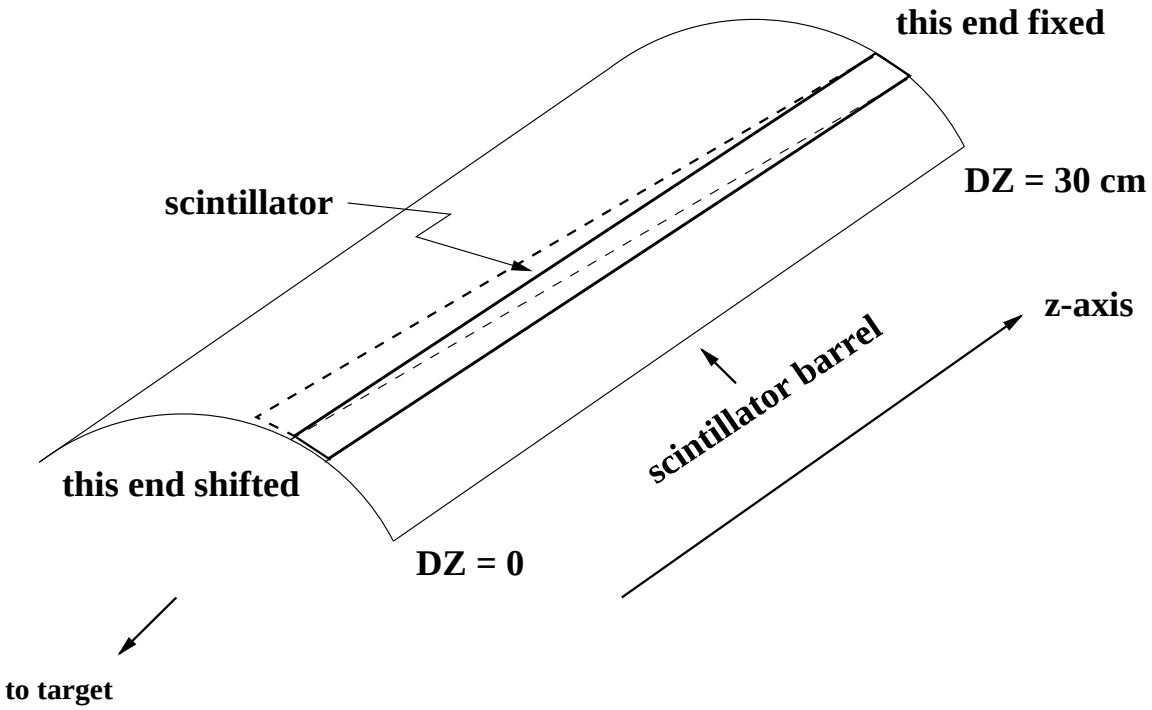

Figure 4.27: Scintillator alignment along z-axis. In this plot the end of the scintillator bar that is near the target is shifted hypothetically by one bar width, while the other end is fixed. This corresponds to a slope of 0.0033 (cm^{-1}).

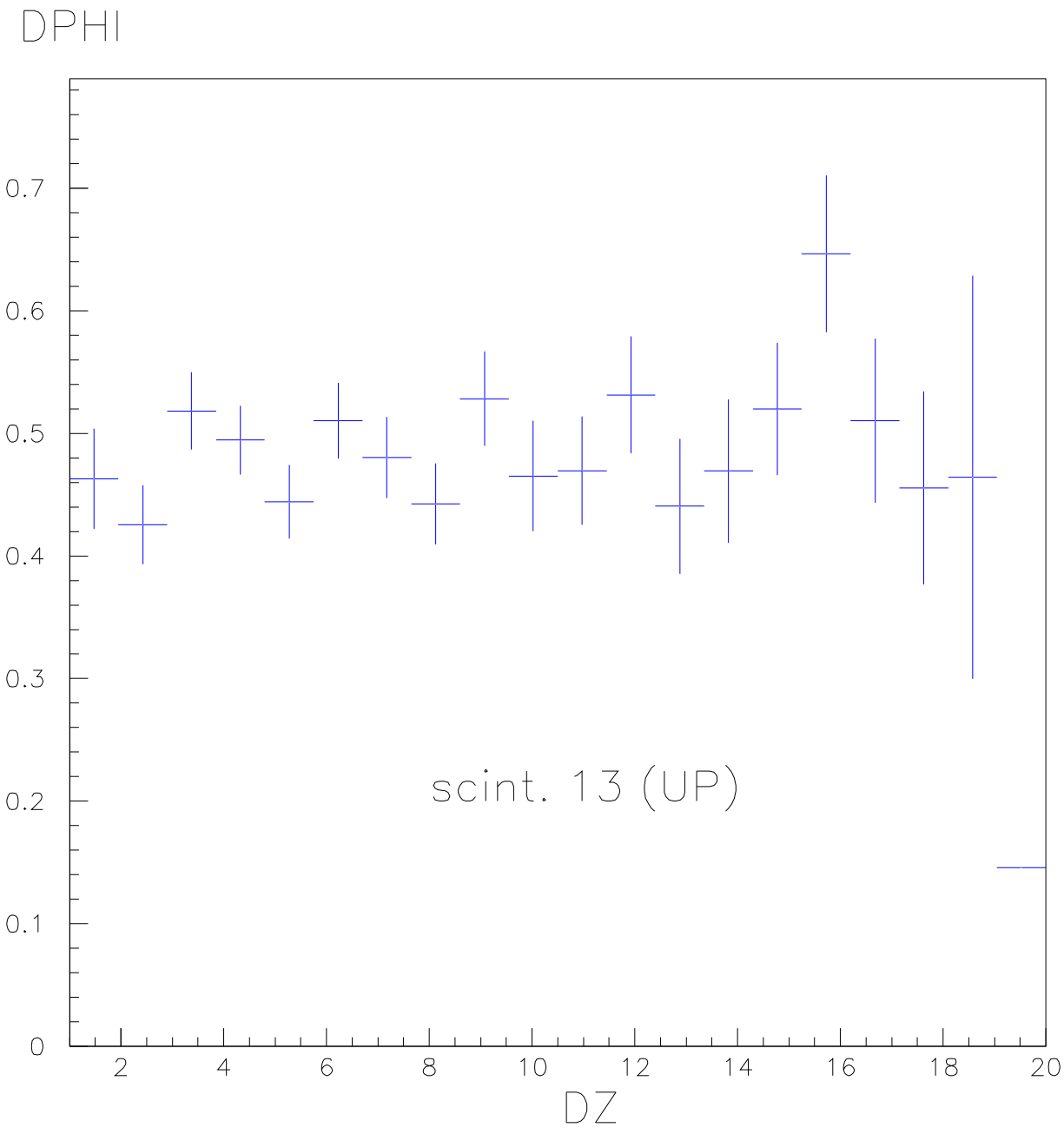

Figure 4.28: DPHI vs. DZ plot for scintillator #13, upstream

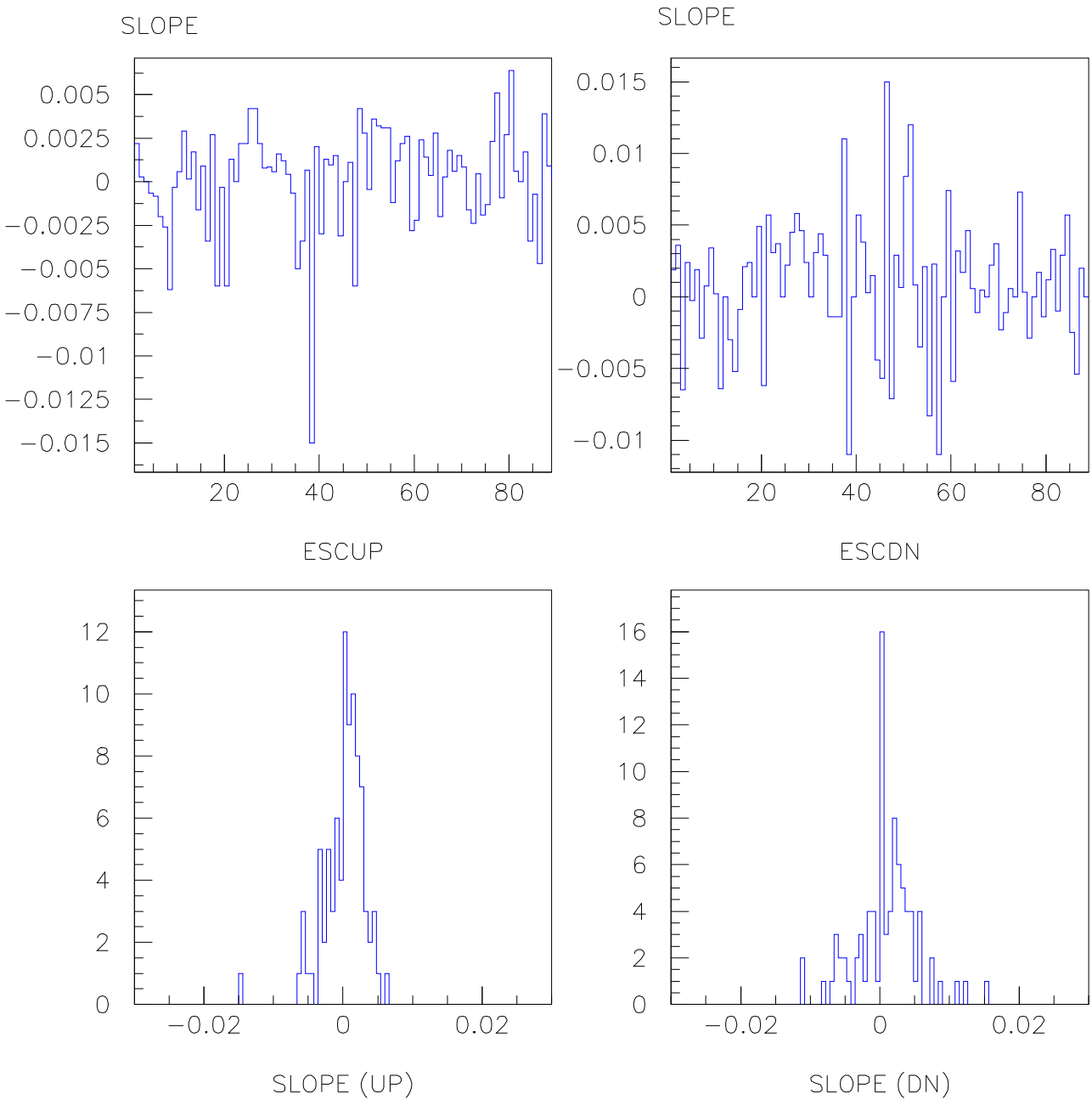

Figure 4.29: The slope distribution over all scintillators. See text for the definition of the slope used here ((S_{scint})). ESCUP: scintillator # for UP, ESCDN: scintillator # for DN.

If a scintillator bar is parallel to the z-axis, then such a plot is flat and the slope is zero. If not, then the slope value tells us how tilted the scintillator is.

The slope here is defined as:

$$S_{scint} = \frac{\Delta DPHI}{\Delta DZ}(cm^{-1}) \tag{4.7}$$

The meaning of this slope is: $\Delta DPHI = 1$ over DZ = 20cm, or $S_{scint} = 0.05\ cm^{-1}$ corresponds to a full scintillator bar width tilt at one end with the other end of the scintillator bar fixed. See Fig. 4.27.

We fit plots like Fig. 4.28 for each of 174 scintillators, get the slope for each and plot S_{scint} vs. ESC. in Fig. 4.29. The FWHM of the distribution is about 0.002 cm^{-1} and 0.004 cm^{-1} for upstream/downstream respectively. The center of the distribution is at 0.002 cm^{-1} and 0.003 cm^{-1}, respectively. This shows that the scintillators are overall very much aligned along the z-axis.

Note that a few scintillators, upstream #38,45, downstream #38, 56 have large slopes, which is almost unphysical. We found this may be actually related to bad phototubes or amplifiers that had low gain. This was discussed in section 4.2.

4.5 Chamber Alignments

Chamber alignments include sideview alignment and endview alignment. We will very briefly describe how they have been done.

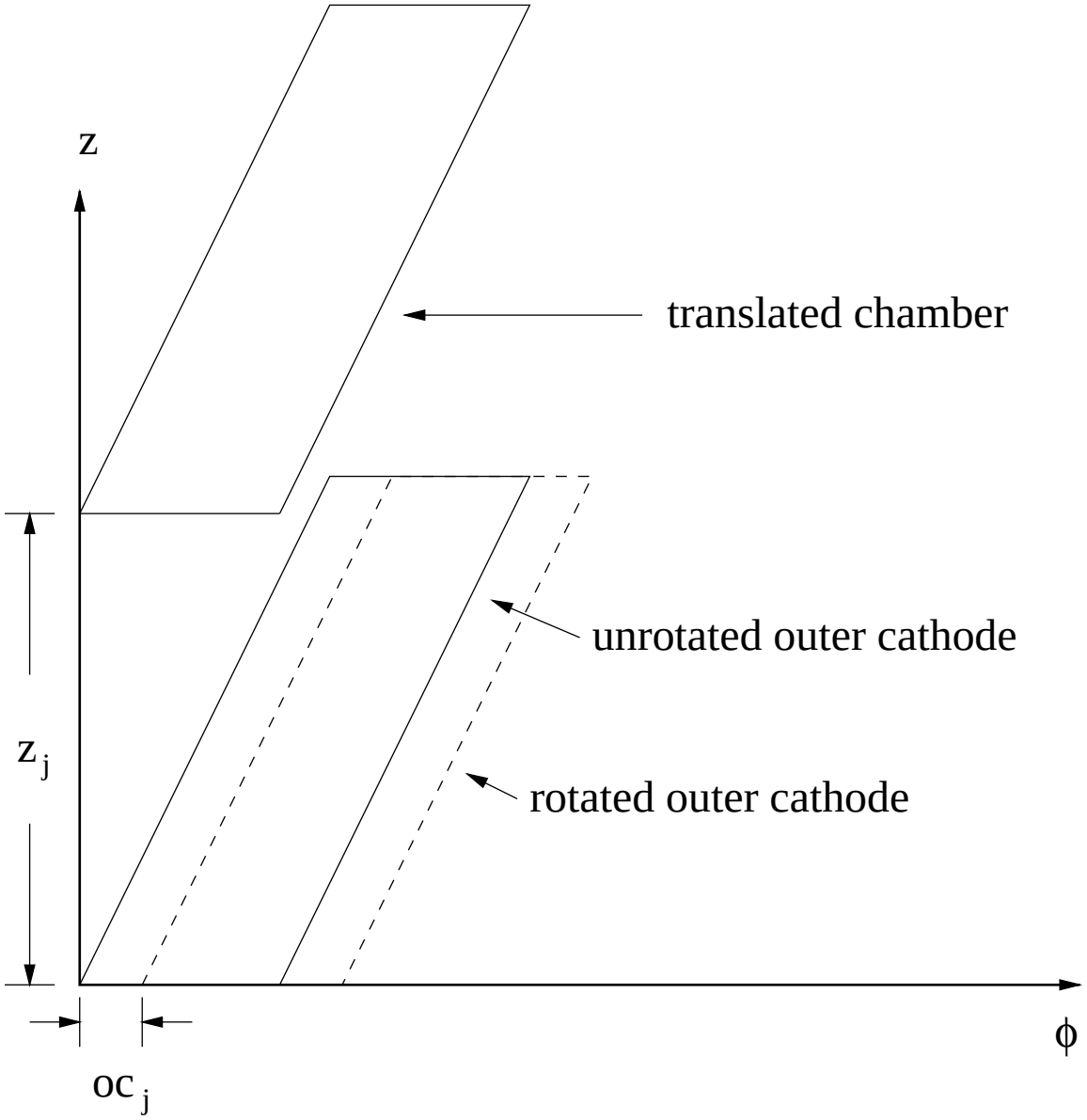

Figure 4.30: Cathode alignment in azimuth and z. ϕ is the azimuthal angle, oc_j is the rotation angle of outer cathode foil of chamber j in azimuth, and z_j is the translation of chamber j along z.

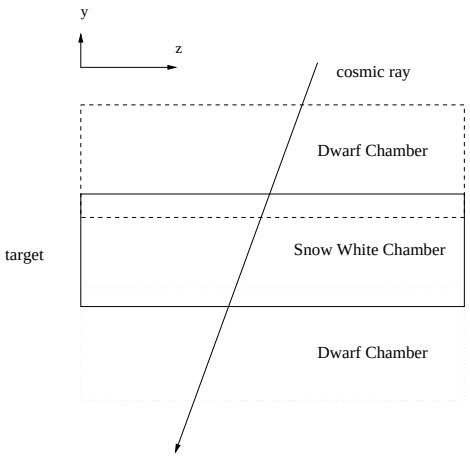

Figure 4.31: Straight cosmic ray tracks crossing chambers. From side view.

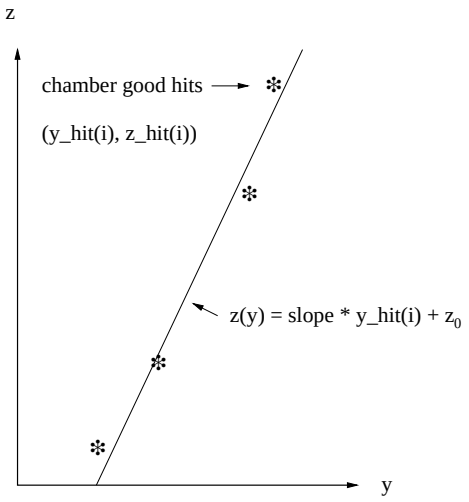

Figure 4.32: The projection of cosmic ray track to the $y-z$ plane, with the least square fit.

4.5.1 Chamber Sideview Alignment

All chambers have an equal length of 126 cm. To determine the z offset of each chamber, cosmic ray data with magnetic field B=0 are used [**?**]. The procedure consists of the following steps:

- selection of good tracks:

  1) Require all chambers turned on

  2) Keep only "good clusters": cathode cluster width < 4 with no gaps between, and anode cluster width < 7 with single gaps assumed to be inefficient hit wires.

  3) Tracks must have two good anode clusters per chamber with two or three such chambers per track.

  4) Keep only "good hits": for chamber z-alignment, they must be triples in both dwarfs

and Snow White, the maximum difference between the z coordinate determined from the intersection of anode wire (cluster) and outer cathode (cluster) and inner cathode (cluster) is $z_{out} - z_{in} = 2.5$ cm.

5) Ignore the chamber in the fit if there are more than three "good hits."

6) Demand 4 to 6 "good hits".

7) Require reduced $\chi^2_{xy} < 2$ and $\chi^2_{zy} < 3$ using linear fit to the tracks with all "good hits."

8) Any triples in any chamber out of the range -33.5 cm$< z <$ 33.5cm are rejected to exclude tracks that pass through and scatter in the lead or heavymet.

- The chambers are first checked to see if the inner and outer cathode foils are rotated relatively in azimuth. The quantity

$$\Delta z^2 = \sum_{i=1}^{n\_hits} (z_{out(i)} - z_{in}(i))^2 \tag{4.8}$$

is minimzed by rotating the outer cathode foil while keeping the inner cathode foil fixed, for each chamber. A set of offsets are obtained for the outer cathode and inner cathode foils.

- Then the chambers are moved along the z-axis to minimize

$$F_z = \sum_{n\_events} (\sum_{i=1}^{n\_hits} ((z(y\_hit(i)) - z\_hit(i))/\sigma)^2/(n\_hits - 2)) \tag{4.9}$$

using MINUIT, where $z(y) = slope * y\_hit(i) + z_0$ is the least square fit to all "good hits," σ is the standard deviation.

4.5.2 Chamber Endview Alignment

The chamber endview alignment was also studied using cosmic ray tracks that were taken with the magnetic field turned off [**?**]. The Snow White coordinate frame is used here. The center of the Snow White chamber is taken as the origin of our coordinate system on the endview plane, and the x-axis is from the center of Snow White to the center of dwarf # 1. See Fig. 4.33. (This is a differnt coordinate frame from the standard one defined in § 4.4).

Each dwarf chamber is aligned with respect to Snow White using three parameters: the rotation angle ϕ about its axis, and the (x,y) location of its center relative to Snow White on the endview plane. See Fig. 4.33. ϕ is defined as the angle between "wire #1" of the dwarf chamber and the x-axis. In the default alignment, ϕ is zero, and (x,y) is (0,0) for all dwarf chambers.

The rotation angles are determine by fitting a straight line to the cosmic ray hits in the chambers when the cosmic ray passes through the chambers and comparing the slope of the straight line measured in the dwarf to the slope measured in the Snow White. Note that if the dwarf chamber is aligned the two slopes should be the same. See Fig. 4.34. The difference of the two slopes is converted to the rotation angle ϕ. See Fig. 4.35. In addition to this, a dwarf-to-dwarf comparison is also done to improve the result. The best rotation angles are then obtained by a linear least squares fit to the full data set.

The (x,y) locations of the dwarfs are determined by the chord distance from a line made by a cosmic ray in Snow White to the center of a dwarf relative to such chord distance within the dwarf for the same cosmic ray. Similar to the case of the rotation angle dicussed above, the difference in the cord distances is converted to the (x,y) of the dwarf by a linear

least squres fit. Using these initial (x,y) coordinates, a second round Snow White-to-dwarf comparisons and dwarf-to-dwarf comparisons are made and a linear least squares fit again used to determine the best set of (x,y) coordinates.

The cuts imposed on the cosmic ray data used for the $x - y$ alignment are:

1) At least two chambers have two anode clusters; at most two anode clusters per chamber.

2) No electron scintilators be hit, to avoid scattering in the lead.

3) Allow hits with and without cathodes but set a limit on the nubmer of cathode clusters that were kept (3 per section).

4) Tagged clusters with a gap of one anode and clusters that ended at a known dead anode.

5) Do not allow cathode clusters with gaps.

These cuts are applied to make sure that only the best tracks are used in determining the alignment parameters.

A more complete study of the alignment involved a check of the sensitivity of alignment parameters to various cuts in the data set. This check led to the finding of uneven azimuthal anode wire spacing in the chambers. When this effect was included in the analysis code, together with the new alignment parameters that were obtained with the uneven wire spacing taken into account, the sensitivity of the alignment parameters to cuts was reduced substantially and the azimuthal variation in the end point energy was removed.

4.6 Beam Spot

The muon beam spot is the muon transverse distribution on the target. It is obtained by reconstructing the positron tracks and extending them back to the target plane. See Fig. 2.3.

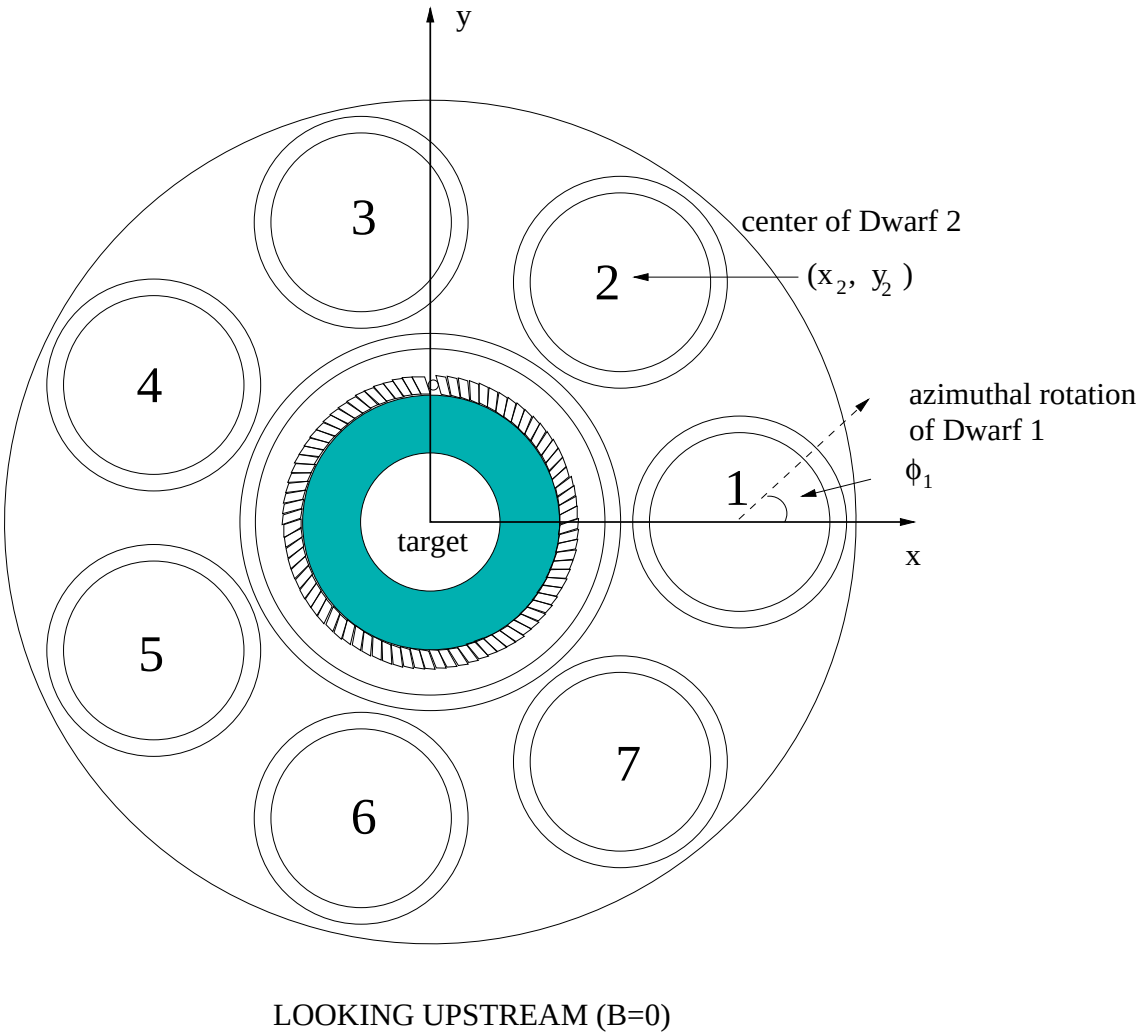

Figure 4.33: Chamber endview alignment: chamber center (x,y) and rotation with respect to its center.

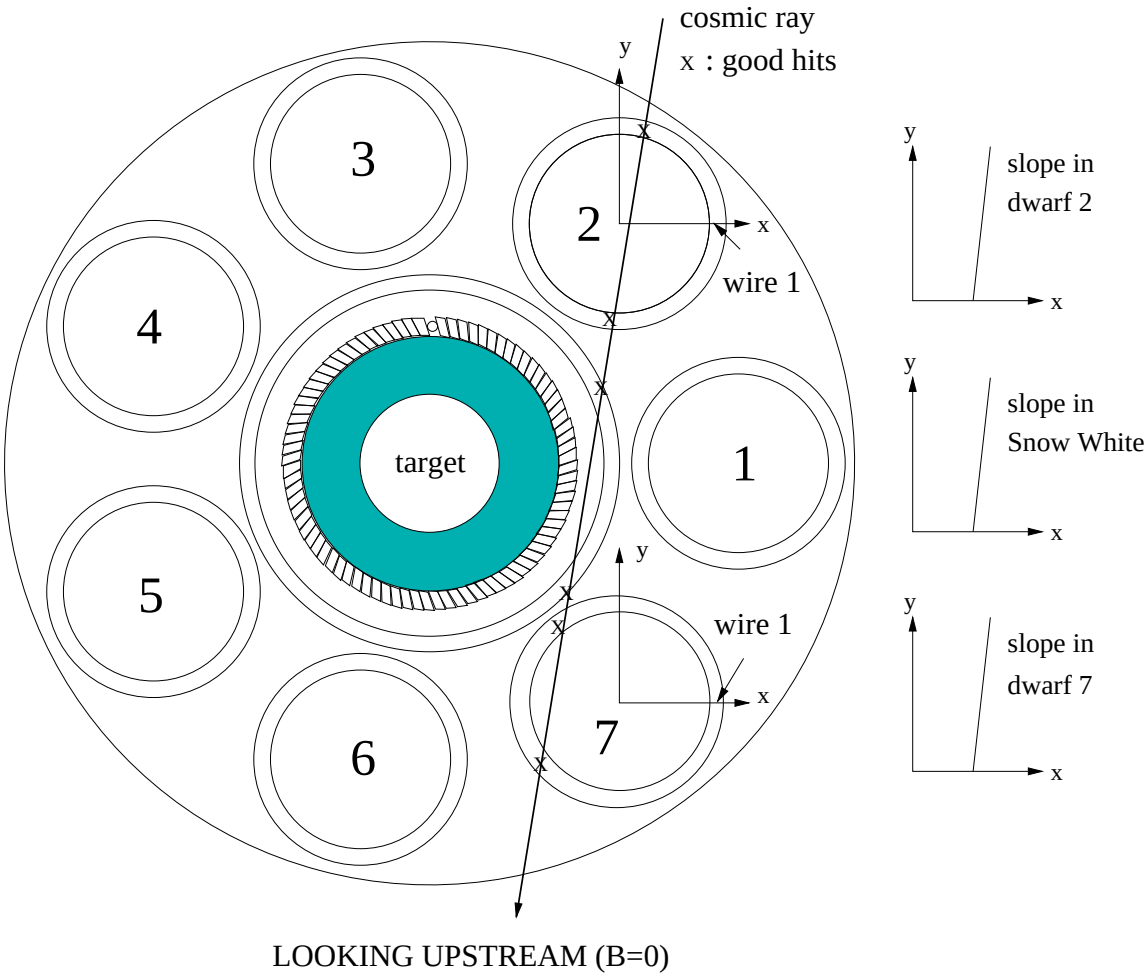

Figure 4.34: For aligned chambers, the slope of the straight line made by a cosmic ray is the same as the slope of the same cosmic ray in Snow White chamber.

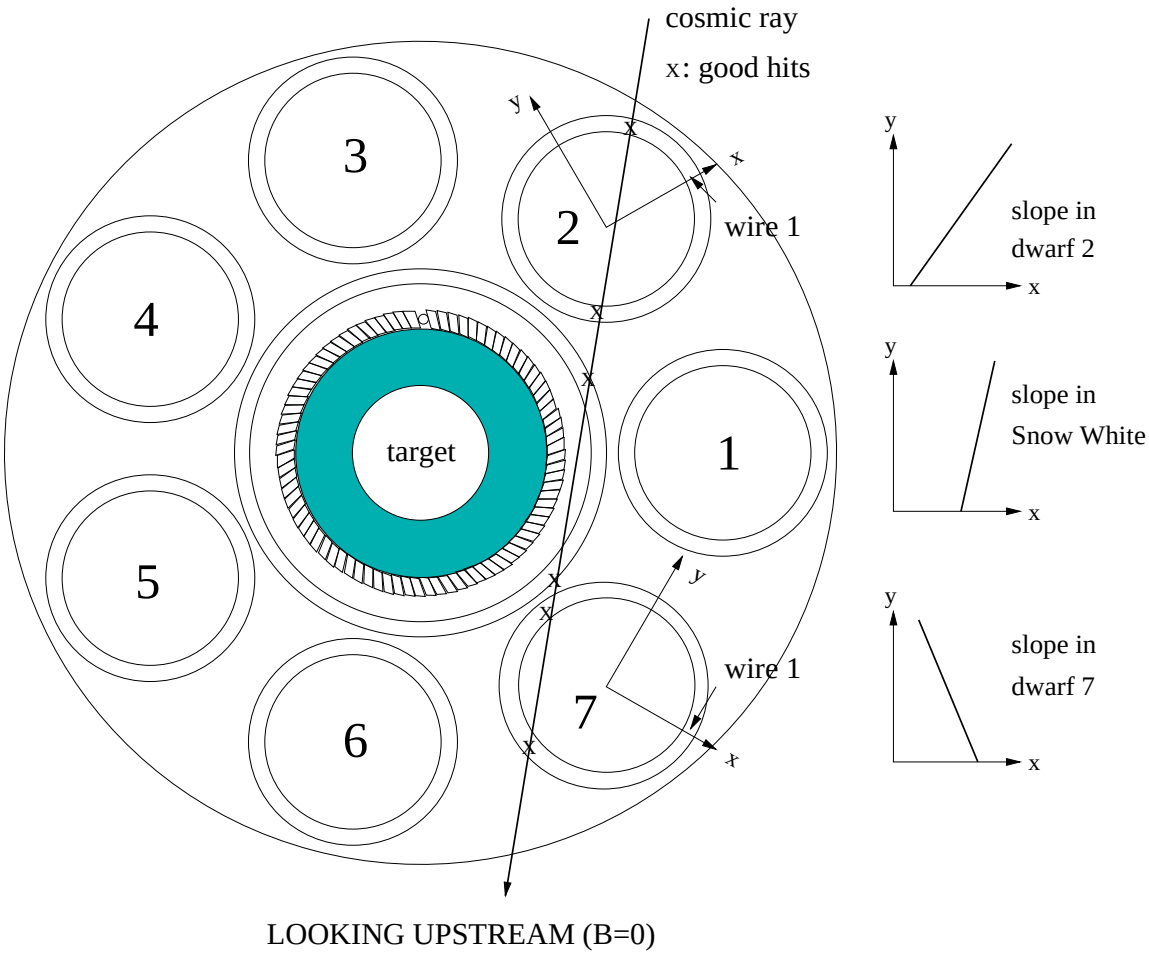

Figure 4.35: For azimuthally misaligned chambers (dwarf 2 and 7 in this example), the slope of the straight line in these chambers are different from that in Snow White.

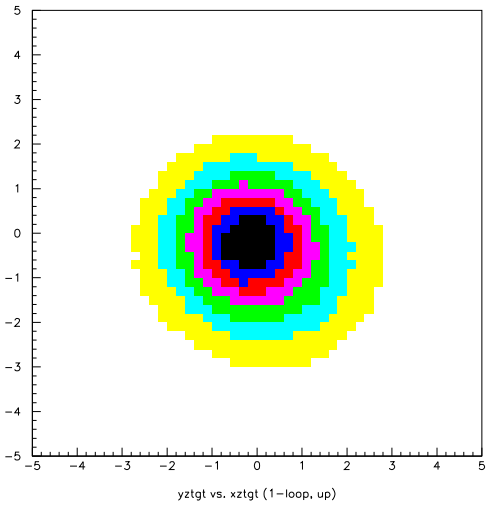

Figure 4.36: The cross section of muon beam (S2 data)

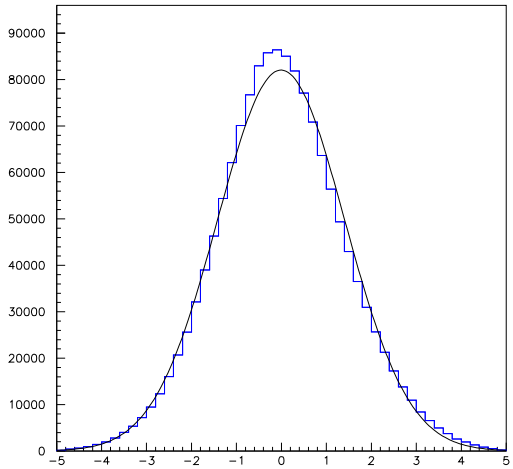

Figure 4.37: Projection of beam cross-section to x-axis and fitted with Gaussian distribution

The beam spot parameters (center and size) are used with other parameters by the Monte Carlo program to simulate the locations of muon decays.

Fig. 4.36 is the reconstructed muon distribution on the target (from data). Fig. 4.37 is its projection on the x-axis. The latter distribution is very close to Gaussian. The projection onto the y-axis is also close to a Gaussian. The fitted mean values and sigmas are taken as the center and the size of the beam spot. If look closely one can find that the distribution is not centered at (0,0). This is a sign that the muon beam may be slightly offset. The beam parameters we want to put into Monte Carlo simulation are the intrinsic beam spot. When they are used, the reconstructed tracks from Monte Carlo simulation *should* give a beam spot that matches the data.

To separate the distortion introduced by the track reconstruction to obtain the intrinsic

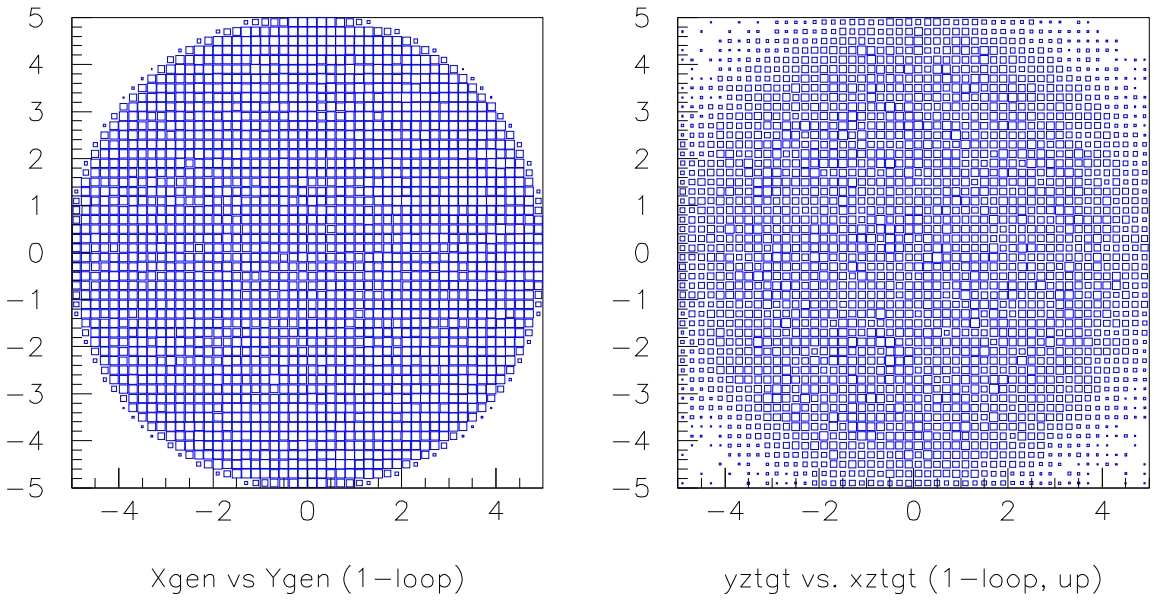

Figure 4.38: Beam spot cross section from Monte Carlo simulation. left: uniform distribution as input; right: after analysis.

Table 4.6: Results for beam spot parameters

source	center $(x, y)cm$	size $(\sigma_x, \sigma_y)cm$
data(S1S2)	-0.088(0.002), -0.492(0.002)	1.417(0.001), 1.381(0.001)
data/MC(Unif.)	-0.106(0.031), -0.500(0.030)	1.130(0.020), 1.080(0.020)
Monte Carlo	-0.089(0.003), -0.492(0.003)	1.414(0.003), 1.380(0.003)

beam spot parameters, the following technique has been applied.

First we analyze data (S2 data was used here), and obtain the measured beam spot parameters shown in line 1 in Table 4.6.

Then we run the Monte Carlo with a uniformly distributed beam spot (Fig. 4.38) and analyze these data to get the reconstruction efficiency for each point on the target.

We then divide this scatter plot by the beam spot (also a scatter plot) that corresponds to line 1, fit the resulting scatter plot with Gaussian, and get the parameters in line 2.

The numbers in line 2 now are the intrinsic beam spot parameters. They are the numbers we put into Mont Carlo. To verify that they do reproduce data beam spot, we run Monte Carlo program again with them and analyze the reconstructed events to get the beam spot parameters, shown in line 3. Numbers in line 3 agree very well with that in line 1.

4.7 Sensitivity Checks

To decide how a particular systematic uncertainty or a specific flaw in the detector system contributes to ρ, we perform a so called "sensitivity check", which estimates the changes in ρ due to given amount of such uncertainty. Sensitivity checks are done by our Monte Carlo program. They are used to generate Table 4.1. They consist of three primary steps (see Fig. 4.39 also):

- run MC reference spectra: normal Michel spectrum with $\rho = 3/4$, and derivative spectrum (see § 5.1), with the quantity of interest at any value (e.g. scintillator efficiency upstream to downstream ratio at 0.931).
- run MC test Michel spectrum with the quantity of interest changed (e.g. the same ratio is changed to 0.838, a 10% change) while keeping all other conditions the same.
- fit the test spectrum and extract a value for ρ using the following formula (the derivation of the formula and the method will be described in Chapter 5):

$$\rho = \frac{3}{4} + \frac{A_D n_D a_N}{A_N n_N a_D}. \tag{4.10}$$

Because in the last step the only running condition that was changed was the quantity of interest, any change in ρ from the expected value of 3/4 must be due to the change in that quantity. In this way a one-to-one correspondence is established. If we repeat this for larger or smaller changes of the same quantity, a trend is established — typically linear. The slope of the linear fit of these points on the sensitivity plot gives us the sensitivity of ρ to this quantity.

In the following subsections, the results for some of the main sensitivity checks will be given.

4.7.1 Scintillator Efficiency Upstream/Downstream Ratio

A sensitivity check on ρ to this ratio is done for a drop of efficiency of 10%, 20% and 30% between upstream and downstream in the Monte Carlo simulations. See Fig. 4.40. There are 7 points on the plot, including the point for no changes in the efficiencies. In this figure, negative values on the abscissa correspond to a drop of efficiency in percentage terms for the downstream scintillators, while positive values correspond to a drop upstream. Because the efficiencies are close to 100%, the percentage drop is equivalent to the change of the ratio in percentage. The slope of the linear fit is 0.0042 ($\delta\rho$ % change), i.e., an uncertainty of 1% in determining the ratio, would correspond to a projected error of 0.0042 in ρ.

4.7.2 Uncertainty in Chamber Wire Efficiencies

Uniform Changes in One Chamber

From the chamber efficiency studies it was found that chamber 6 was extremely noisy. This makes it very difficult to measure its efficiency. A large uncertainty is expected. We have done the following sensitivity checks to see how this can affect ρ.

We did two checks. In both checks we used the best measured efficiencies (corresponding to pulse height discriminator thresholds in the simulation) for all eight chambers. For the first check, the thresholds of the inner cathodes of Dwarf 6 were first increased by 20% and the normal Michel spectrum and derivative spectrum (see § 5.1) obtained under this condition

were used as the reference. Then the thresholds were changed by $\pm 5\%, \pm 20\%$ based on the reference, and ρ was extracted for each case. See Fig. 4.41. A 5% uncertainty in the inner cathode thresholds in chamber 6 gives a change of 0.00035 in ρ. This is within our goal.

We also did the same for all three layers. Instead of checking just one layer (inner cathode), we change thresholds of inner/outer cathodes and anodes all at the same time. The sensitivity of ρ was found to be **twice** the sensitivity in the first case, not three times, because of correlations. An error of 0.0006 corresponds to a 5% uncertainty in determining all three layer thresholds. See Fig. 4.41.

Cathode Efficiency z-dependence

The complexity in determining chamber anode/cathode efficiencies not only makes it difficult to determine efficiencies with a high precision, but also makes it difficult to model it with the Monte Carlo program and perform a sensitivity check. Cathode efficiencies are found to vary along the z-axis [**?**]. There are a few hot anodes in some chambers that may be responsible for this cathode efficiency z-dependence. The possible mechanism is that these hot anodes induce more image charge than usual on the overlapping cathodes of the triple. When a cathode stripe makes a full revolution along a full length of a chamber, it crosses all anodes at different z-locations. When a positron track strikes the cathode stripe at a particular z-location where it crosses a hot anode, the efficiency of this cathode can be higher than at other z-locations.

This provides a model to check the sensitivity. The detail is described in the following.

In order to simulate the real situation as closely as possible, we picked three chambers

Table 4.7: Simulated hot anodes in dwarfs 3,4 and 6 that cause the image charge on the overlapping cathodes to higher or lower than normal. See text for explanation.

chamber	anode range	raise/lower
dwarf 3	205-214(incoming)	raise
	215-224(incoming)	lower
	265-274(outgoing)	raise
	275-284(outgoing)	lower
dwarf 4	200-209(incoming)	raise
	210-219(incoming)	lower
	260-269(outgoing)	raise
	270-279(outgoing)	lower
dwarf 6	279-288(incoming)	raise
	1-10 (incoming)	lower
	50-59 (outgoing)	raise
	60-69 (outgoing)	lower

each of which has ten hot anodes next to each other. When generating an event in Monte Carlo, if the overlapping anode is one of those ten hot anodes, more image charge (5%, 10%, etc) is deposited on the cathode (inner and outer, upstream). This has to be modified to accommodate the fact that the average efficiency of a particular cathode should not be altered. To do so, four groups of ten anodes intead of one are chosen such that they correspond to incoming and outgoing locations of two tracks that are next to each other. If the cathode overlaps a hot anode at the incoming location of a track and the image charge on the cathode is raised by say, 10%, then when the track leaves the chamber at the outgoing location, the cathode image charge is lowered by same percentage. Another ten anodes next to these two locations are also chosen and they do just the opposite: for incoming case, we lower the image charge while for outgoing case we raise the image charge. See Table 4.7.

4.7.3 Uncertainty in Scintillator Barrel Azimuthal Offset

In section 3.4.1 we discussed how the scintillator barrel azimuthal offset was derived. In order to check the sensitivity of ρ to the offset, we have analyzed the same Monte Carlo data with different offsets: 0.4, 0.5, 0.6, 0.8, and 1 unit of one scintillator bar width, and get $\Delta\rho$ for each case and made upper plot in Fig. 4.42. The uncertainty in determining the angle is about 0.05 of a bar, which implies that the projected $\Delta\rho$ is 0.00002. This is negligible.

4.7.4 Uncertainty in Scintillator Barrel Center Offset

For scintillator barrel center offset, we analyzed the same data with different x: $\pm$ 0.1 cm, $\pm$ 0.3 cm, $\pm$ 0.5 cm. The result is in the lower plot of Fig. 4.42. The uncertainty in

determining the center is about 0.01 cm. Projected $\Delta\rho$ is 0.00003. This is negligible too.

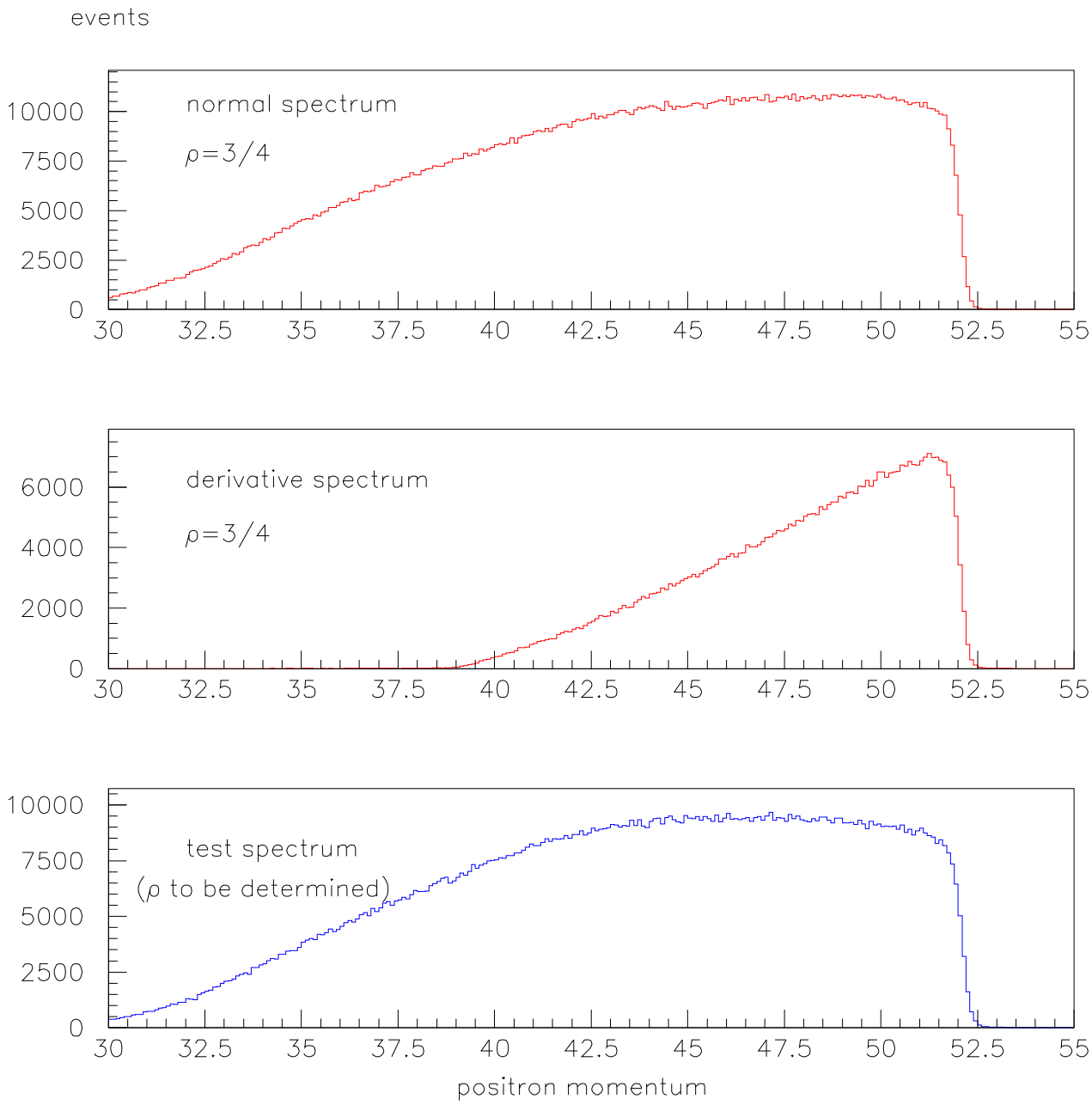

Figure 4.39: Reference spectra and test spectrum for sensitivity checks

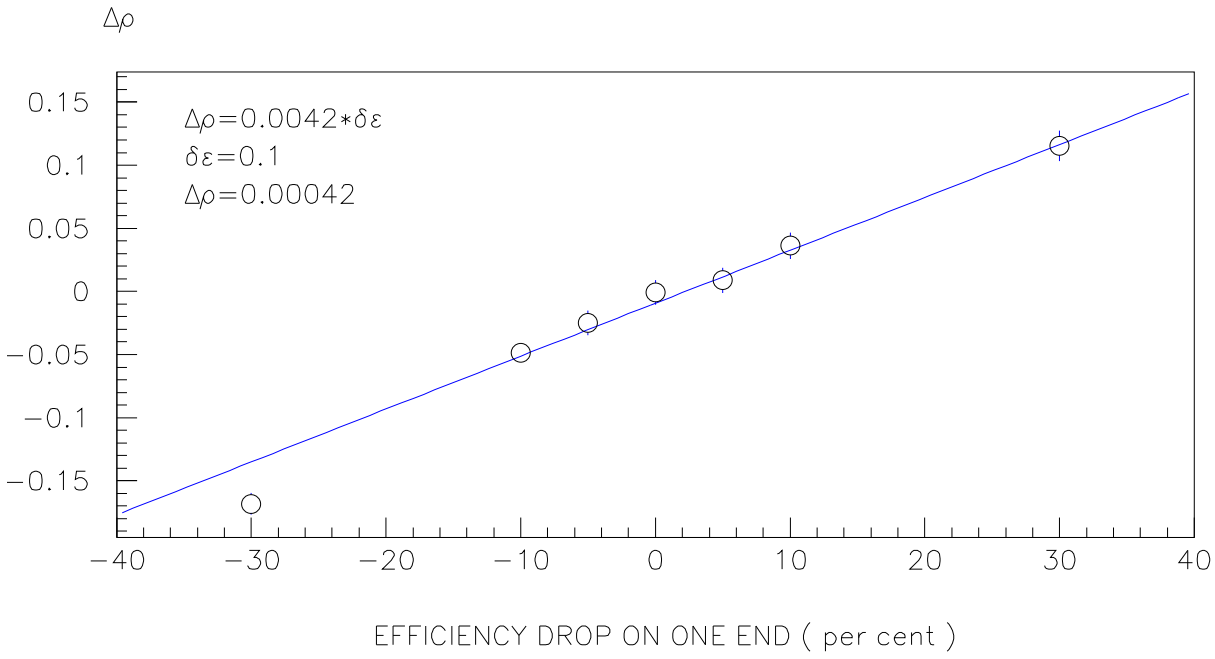

Figure 4.40: Sensitivity of Michel parameter ρ to scintillator upstream/downstream efficiency ratio

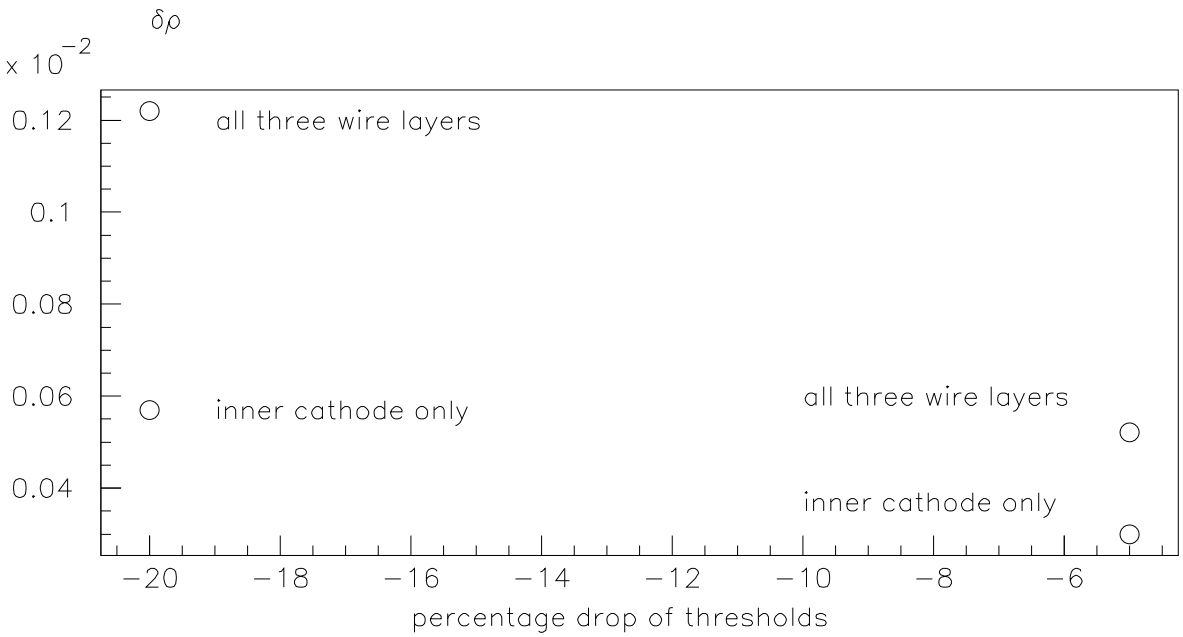

Figure 4.41: Sensitivity of Michel parameter ρ to wire efficiencies (thresholds) uncertainty in one chamber.

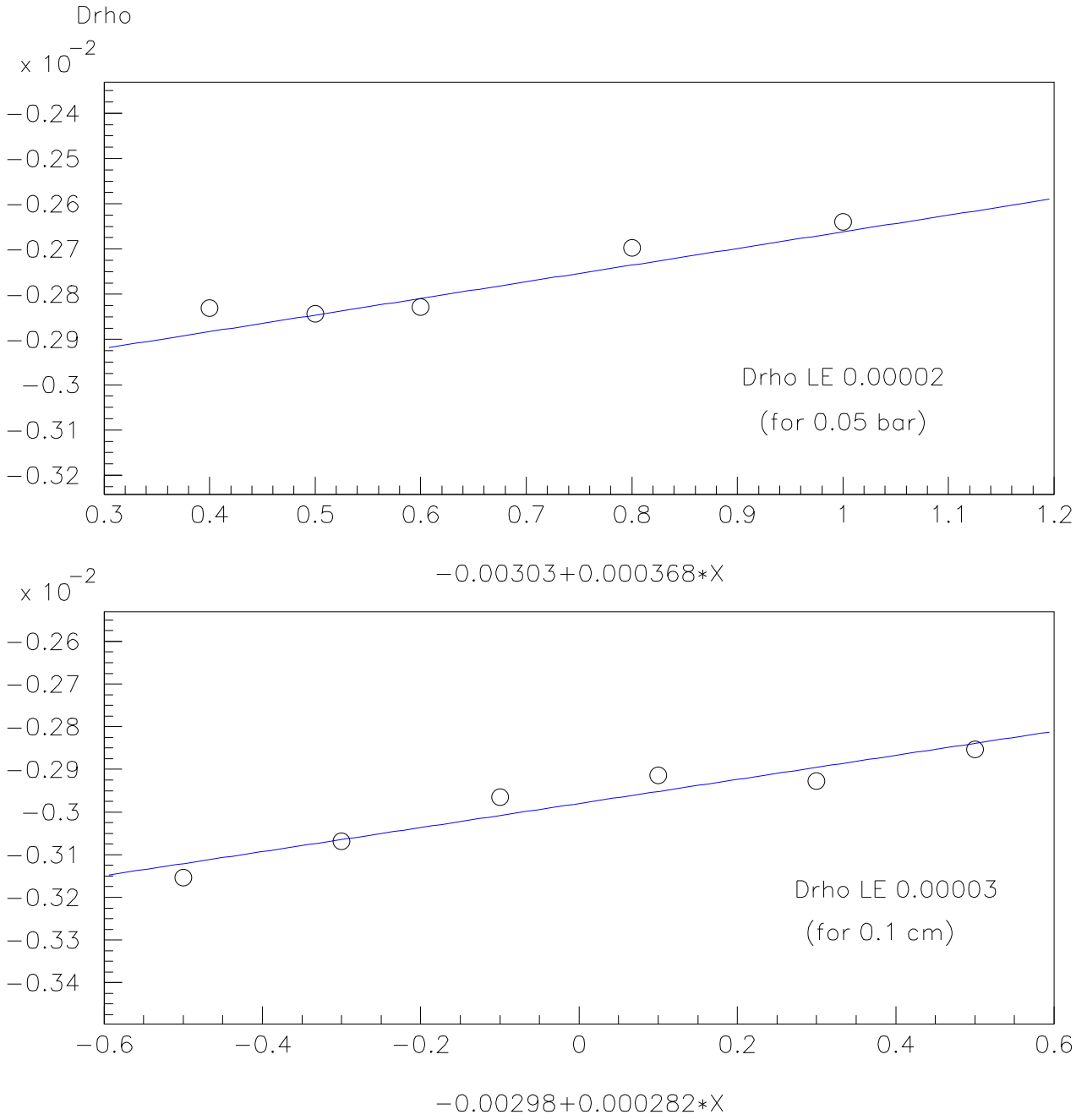

Figure 4.42: Sensitivity of Michel parameter to scintillator barrel azimuthal angle (upper plot) and center (lower plot).

Chapter 5

Results and Conclusions

5.1 How ρ is Extracted

The Michel parameter ρ is extracted by comparing the Monte Carlo spectrum to the data spectrum. The same method was used in the sensitivity checks described in Chapter 4. We will now discuss how Equation (4.10) is derived and how the normalization factors a_N and a_D, particularly their ratio a_N/a_D is estimated.

If we expand the muon differential decay rate (radiation corrected), Equation (1.4):

$$\begin{aligned}\frac{d^2\Gamma}{dxd(\cos\theta)} &\propto x^2\Big\{\Big[6(1-x)+\frac{4}{3}\rho(4x-3)\Big]r_1(x) \pm P_\mu\xi\cos\theta\Big[2(1-x)+\frac{4}{3}\delta(4x-3)\Big]r_2(x)\Big\} \\ &= M(x,\cos\theta,\rho)\end{aligned} \tag{5.1}$$

in Taylor series at $\rho_0 = 3/4$, with $\eta = 0, \xi = 1$ and $\delta = 3/4$, we have:

$$\begin{aligned} M(x, \cos\theta, \rho) &= M(x, \cos\theta, \rho_0)\Big|_{\rho_0=\frac{3}{4}} + (\rho - \rho_0)\frac{\partial}{\partial\rho}M(x, \cos\theta, \rho)\Big|_{\rho_0=\frac{3}{4}} \\ &\quad + (\rho - \rho_0)^2\frac{\partial^2}{\partial\rho^2}M(x, \cos\theta, \rho)\Big|_{\rho_0=\frac{3}{4}} + ... \\ &= x^2\Big[(3-2x)r_1(x) + P_\mu\cos\theta(2x-1)r_2(x)\Big] + (\rho - \frac{3}{4})\frac{4}{3}x^2(4x-3)r_1(x) \\ &\quad + 0 \\ &= M_N + (\rho - \frac{3}{4})M_D \end{aligned} \tag{5.2}$$

where M_N and M_D correspond to the normal decay rate at ρ=3/4 and first order derivative of decay rate at ρ=3/4, respectively:

$$\begin{aligned} M_N &= x^2\Big[(3-2x)r_1(x) + P_\mu\cos\theta(2x-1)r_2(x)\Big] \\ M_D &= \frac{4}{3}x^2(4x-3)r_1(x) \end{aligned} \tag{5.3}$$

The measured positron Michel spectrum (or test Michel spectrum, as in the case of sensitivity checks) S should be proportional to the integral of $M(x, \cos\theta, \rho)$ over positron momentum and solid angle:

$$\begin{aligned} S &\propto \int M(x, \cos\theta, \rho)\epsilon(x, \theta, \phi)dxd(\cos\theta)d\phi \\ &= n + (\rho - \frac{3}{4})d \end{aligned} \tag{5.4}$$

where ϵ is the positron detector system's efficiency as a function of momentum and acceptance, and

$$\begin{aligned} n &= \int M_N\epsilon(x, \theta, \phi)dxd(\cos\theta)d\phi \\ d &= \int M_D\epsilon(x, \theta, \phi)dxd(\cos\theta)d\phi. \end{aligned} \tag{5.5}$$

To extract ρ, the measured (data) Michel spectrum (or test spectrum) S is fitted to the best combination of two Monte Carlo spectra N and D:

$$\begin{aligned} N &= \frac{n_N}{a_N}\int M_N\epsilon(x, \theta, \phi)dxd(\cos\theta)d\phi = \frac{n_N}{a_N}n \\ D &= \frac{n_D}{a_D}\int M_D\epsilon(x, \theta, \phi)dxd(\cos\theta)d\phi = \frac{n_D}{a_D}d. \end{aligned} \tag{5.6}$$

where

$$\begin{aligned} a_N &= \int |M_N| dx d(\cos\theta) d\phi \\ a_D &= \int |M_D| dx d(\cos\theta) d\phi \end{aligned} \tag{5.7}$$

are the normalization constants, N and D are called the 'normal' spectrum and 'derivative spectrum' (or Drho Spectrum) respectively, and n_N and n_D are the number of events in the two Monte Carlo spectra. Note that M_D is negative when $x < 0.75$, and the integration should be done with absolute value of M_D in order to get the total number of events in the derivative spectrum.

The fitting is done using the standard χ^2 minimization for each bin of the spectra:

$$\begin{aligned} S &= A_N N + A_D D \\ &= A_N \frac{n_N}{a_N} n + A_D \frac{n_D}{a_D} d \\ &= A_N \frac{n_N}{a_N} (n + \frac{A_D n_D a_N}{A_N n_N a_D} d) \end{aligned} \tag{5.8}$$

Fitting coefficients (or amplitudes) A_N and A_D are adjusted to minimize χ^2. The measured spectrum (or test spectrum) and the N and D spectra are binned in the same way (250 bins from $x = 0.568$ to $x = 1$, or 54 bins from $x = 0.782$ to $x = 0.985$, for example).

Michel parameter ρ extracted via this method is then expressed in the following by comparing Equation (5.8) to (5.4):

$$\rho = \frac{3}{4} + \frac{A_D n_D a_N}{A_N n_N a_D}. \tag{5.9}$$

In principle, the ratio $\frac{a_N}{a_D}$ is calculated in the entire solid angle and momentum range. However, there are a few modifications that are specific to our spectrometer:

- momentum: the momentum is integrated over the range of the acceptance of the detector system (0.568 to 1.0).

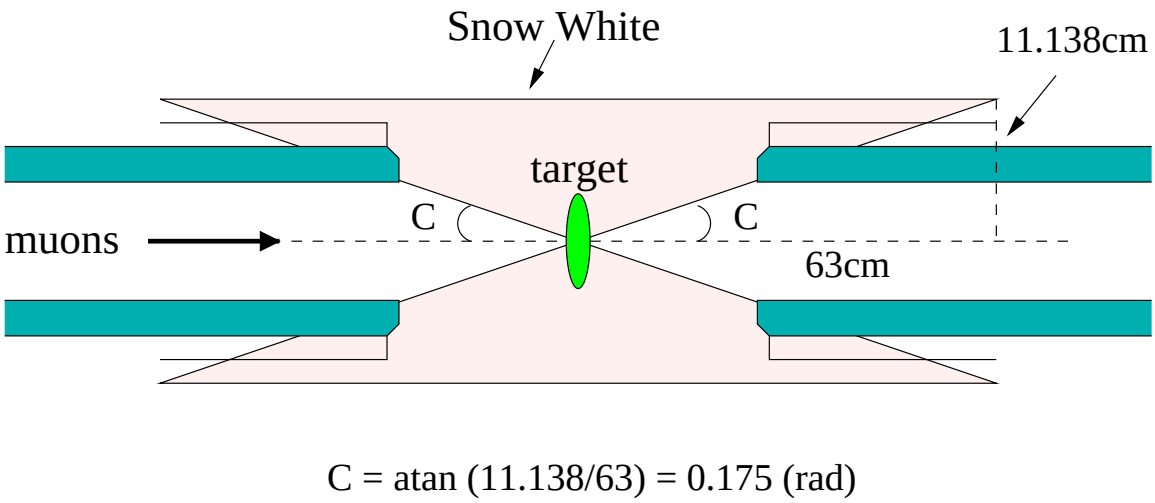

Figure 5.1: Sideview of the covered detector volume by chambers (shaded area).

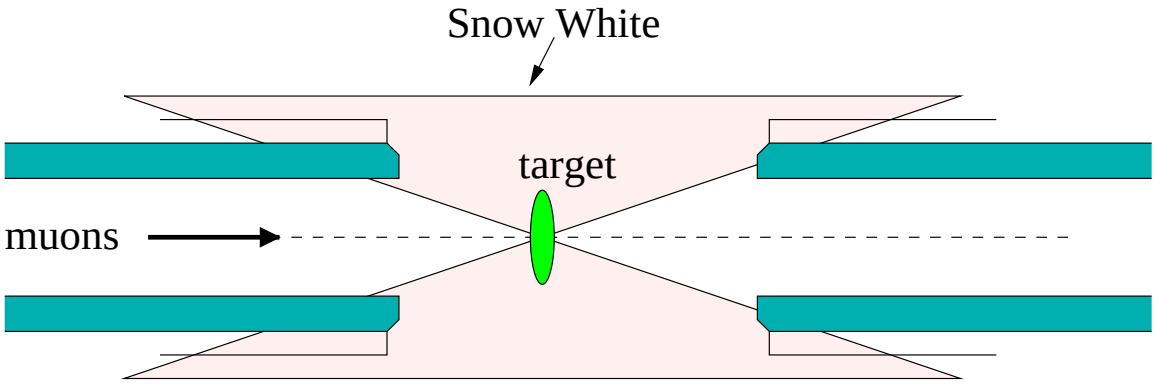

Figure 5.2: Sideview of the covered detector volume by chambers (shaded area), with the target off slightly to the upstream of side of the center.

- polar angle: the polar angle is integrated over the angle covered by our spectromemter. In Fig. 5.1, the polar angle C covered by the chambers in DN is $C = \tan^{-1} \frac{11.138cm}{63cm} = 0.1749$ rad.

- However, an offset in target z-location results in an asymmetry in the integration range of $\cos\theta$ (see Fig. 5.2). The target was determined to be located at about 3 mm off center along z. This is a small displacement compared to the half length of the Snow White chamber (63 cm). Thus, the lower and upper angles are now $\tan^{-1} \frac{11.138}{63+0.3} = 0.1742$ rad and $\pi - \tan^{-1} \frac{11.138}{63-0.3} = 2.966$ rad.

The final result for the ratio a_N/a_D, with the asymmetry taken into account and beam polarization 90% and a flat efficiency function over the restricted acceptance as described above, is $(\int_{-0.568}^{1} dx \int_{-0.9846}^{0.9849} d(\cos\theta) \int_0^{2\pi} d\phi |M_N| \;/\; \int_{-0.568}^{1} dx \int_{-0.9846}^{0.9849} d(\cos\theta) \int_0^{2\pi} d\phi |M_D|) = 2.13$.

5.2 Results

During the RHO data taking in August 1993 approximately 400 million triggers were collected. About 20% of the triggers passed the reconstruction requirements in the early steps of the analysis. In extracting ρ, we only used 1-loop events that were taken by half of the scintillator TDCs, the 'Even' TDCs ('Odd' TDC data were discarded because of operational difficulties), and the fitting range of the spectra is chosen to be between 40.9 MeV and 51.5 MeV to ensure the quality of the fit. The total number of muon decay events that survived all those selections in the analysis is about 9 million. See Table 5.1. The Michel spectrum from these events are then fitted with the Monte Carlo Michel spectrum (normal and derivative spectrum) to extract ρ. Table 5.2 shows the number of Monte Carlo events generated

Table 5.1: RHO experimental data sets.

data set	total triggers	1-loop events (UP,DN)	# events used to extract ρ (UP,DN)*
S1	133 M	6.2 M, 4.2 M	2.0 M, 1.3 M
S2	104 M	5.2 M, 3.5 M	1.6 M, 1.0 M
DY	163 M	4.2 M, 5.3 M	1.3 M, 1.6 M
			* 1-loop,'Even', 40.9-51.5 MeV.

under three different running conditions (S1,S2,DY, for upstream and downstream, normal and derivative spectrum, respectively). Monte Carlo data sets generally have 4-10 times more statistics than experimental data in order to keep the error (statistical) from Monte Carlo negligible compared to that from data. See the last columns of both tables.

The statistical error on ρ, then, is roughly 0.006 for each set. When the final value of ρ is obtained by combining the ρ's from the three sets, the statistical error is about 0.002. This is larger than what we expected, and the reason is obvious: we had to throw away more data in the final extraction of ρ than originally planned, to reduce the large systematic uncertainties.

The Michel parameter ρ is extracted by comparing the Monte Carlo spectrum to experimental spectrum that correspond to the above two tables. Using the χ^2 minimization method described in the first section of this Chapter, with 54 energy bins between 40.9 and 51.5 MeV and with 2 amplitudes (for Monte Carlo 'normal' and 'derivative' spectrum respectively) as parameters to be determined, our fit gives the results of $\Delta\rho$ for each set of data, where

$$\Delta\rho = \rho - \frac{3}{4} = \frac{A_D n_D a_N}{A_N n_N a_D}. \tag{5.10}$$

Table 5.2: RHO Monte Carlo data sets.

data set	1-loop events generated	# events used to extract ρ
S1, UP, normal	28.6 M	20.7 M
S1, UP, derivative	9.5 M	8.7 M
S1, DN, normal	15.9 M	10.9 M
S1, DN, derivative	7.6 M	6.5 M
S2, UP, normal	15.3 M	10.0 M
S2, UP, derivative	9.5 M	8.7 M
S2, DN, normal	9.1 M	5.6 M
S2, DN, derivative	7.5 M	6.6 M
DY, UP, normal	20.7 M	14.0 M
DY, UP, derivative	8.2 M	7.5 M
DY, DN, normal	23.0 M	15.9 M
DY, DN, derivative	6.8 M	5.9 M

Table 5.3: Extraction of $\Delta\rho$

data set	A_D(stat. error)	A_N(stat. error)	reduced χ^2	n_D	n_N	$\Delta\rho$ (stat. error)
S1, UP	.1057(.0002)	-.0217(.0005)	1.8	20.7M	8.7M	-.183(.004)
S1, DN	.1236(.0003)	-.0074(.0005)	1.5	10.9M	6.5M	-.077(.005)
S2, UP	.1661(.0004)	-.0128(.0004)	1.3	10.0M	8.7M	-.142(.005)
S2, DN	.1803(.0005)	.0026(.0004)	4.6	5.6M	6.6M	.004(.005)
DY, UP	.0653(.0002)	-.0094(.0004)	3.0	14.0M	7.5M	-.163(.007)
DY, DN	.0749(.0002)	.0261(.0006)	1.8	15.9M	5.9M	.275(.007)

Table 5.4: The result of the the RHO measurement.

	S1	S2	DY	combined
$\Delta\rho$ (stat. error)	-.1410(.003)	-.0720(.003)	.0830(.005)	-.047(.002)

and A_D and A_N are the fitted values for 'derivative' and 'normal' amplitudes, n_D and n_N are the number of events in the fit range 40.9 - 51.5 MeV for 'normal' and 'derivative' spectrum respectively, and a_N/a_D=2.13. Fig 5.3 shows the Michel spectrum from data (S1) in the momentum range of 30.0 - 55.0 MeV/c, while Figures 5.4, 5.5 and 5.6 show the result of the fit for each set. The fit results are shown in detail in Table 5.3. The weighted average of ρ's for each of three sets of data are shown in Table 5.4, together with the combined ρ.

The final result is plotted in Fig. 5.7.

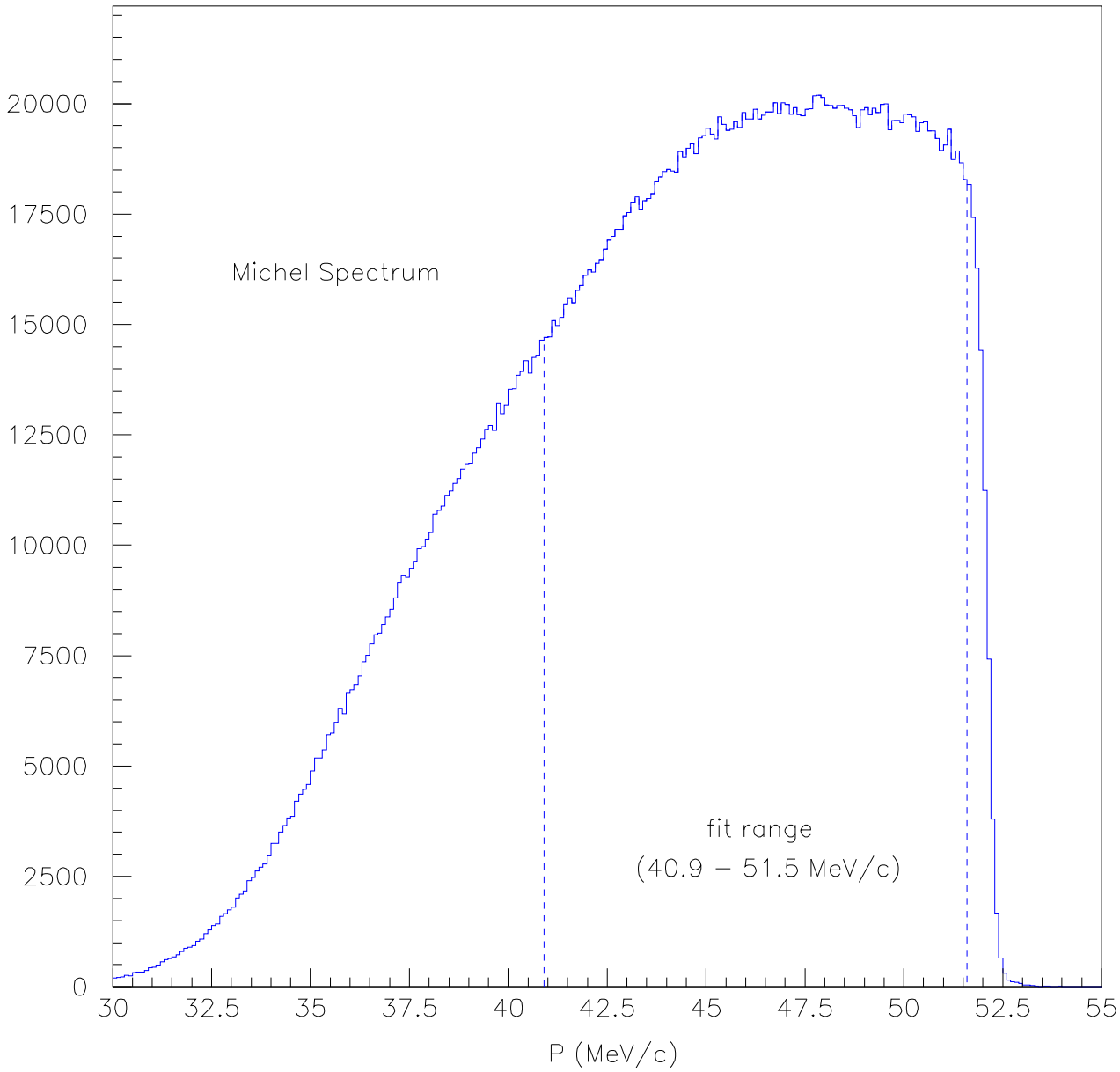

Figure 5.3: Michel Spectrum measured (S1 data,UP)

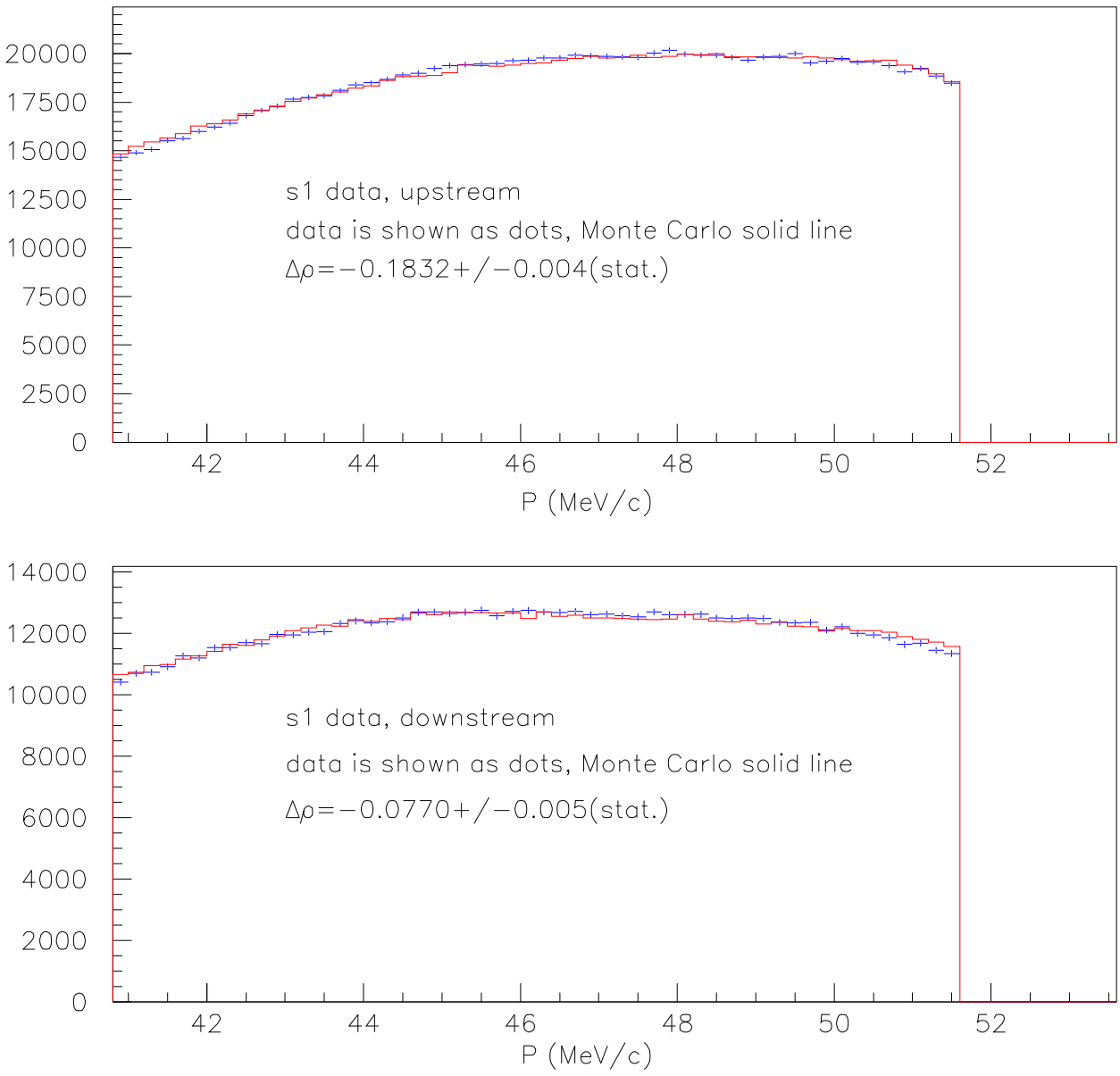

Figure 5.4: χ^2 fit of Monte Carlo to S1 data.

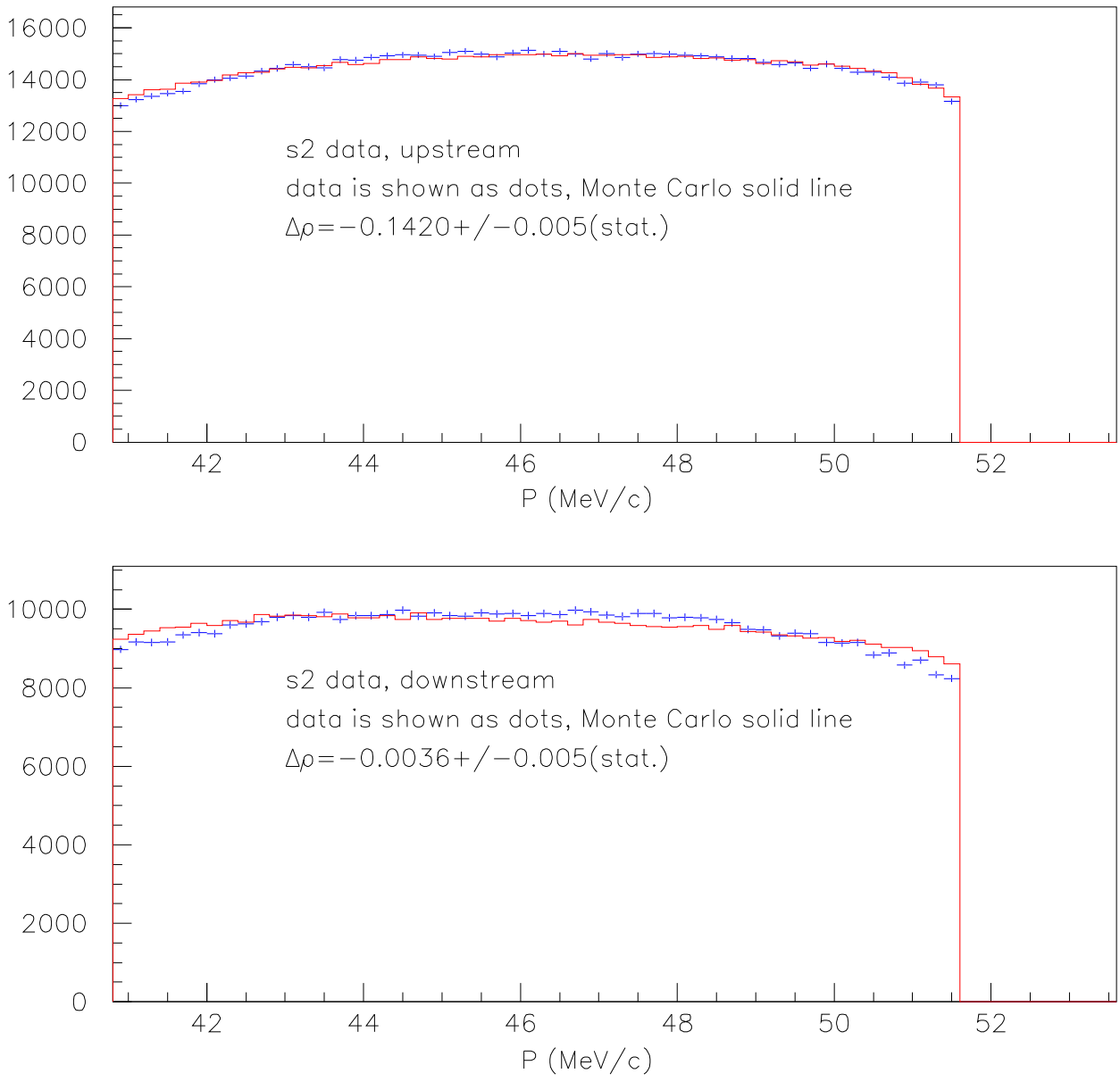

Figure 5.5: χ^2 fit of Monte Carlo to S2 data.

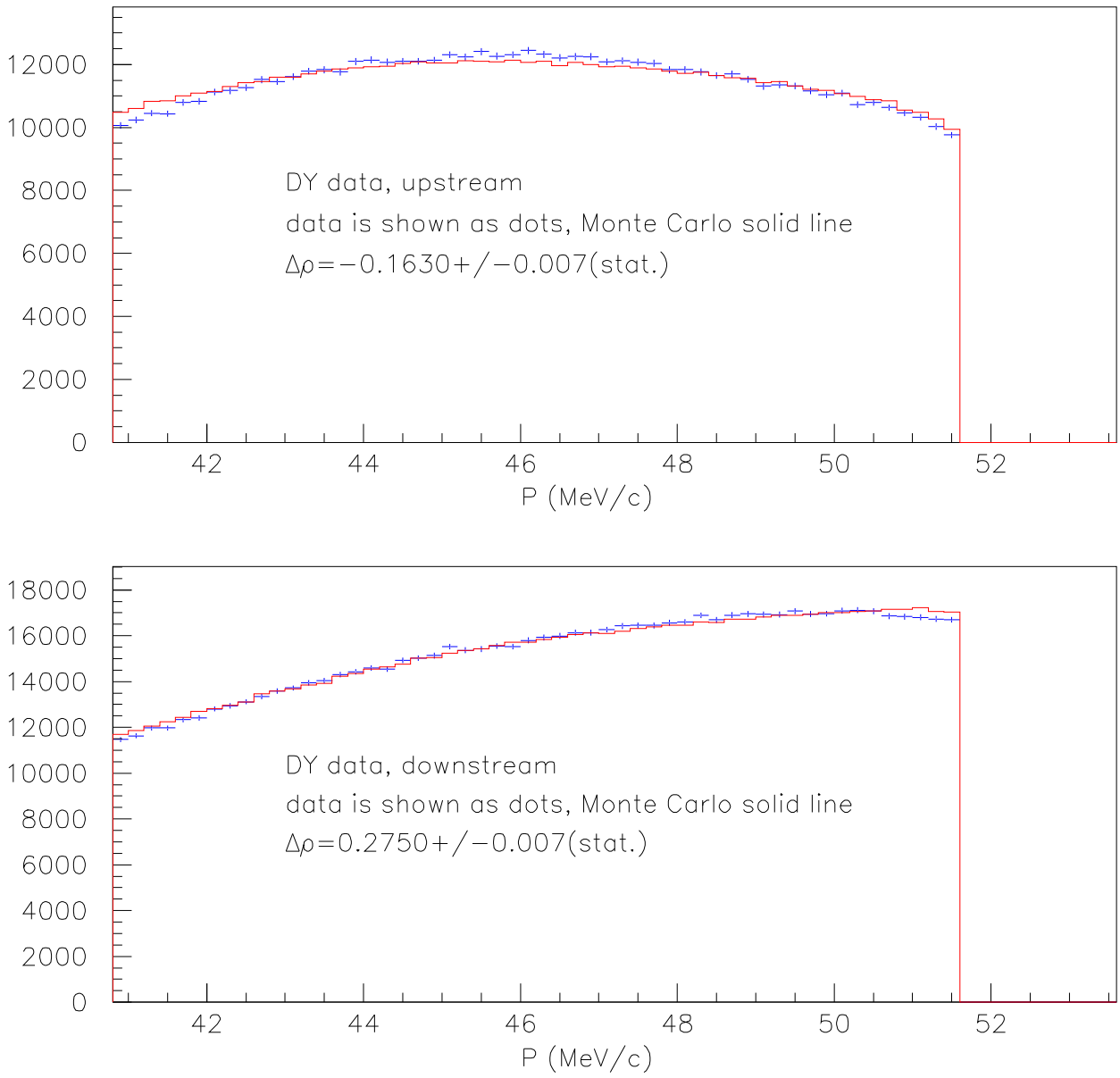

Figure 5.6: χ^2 fit of Monte Carlo to DY data.

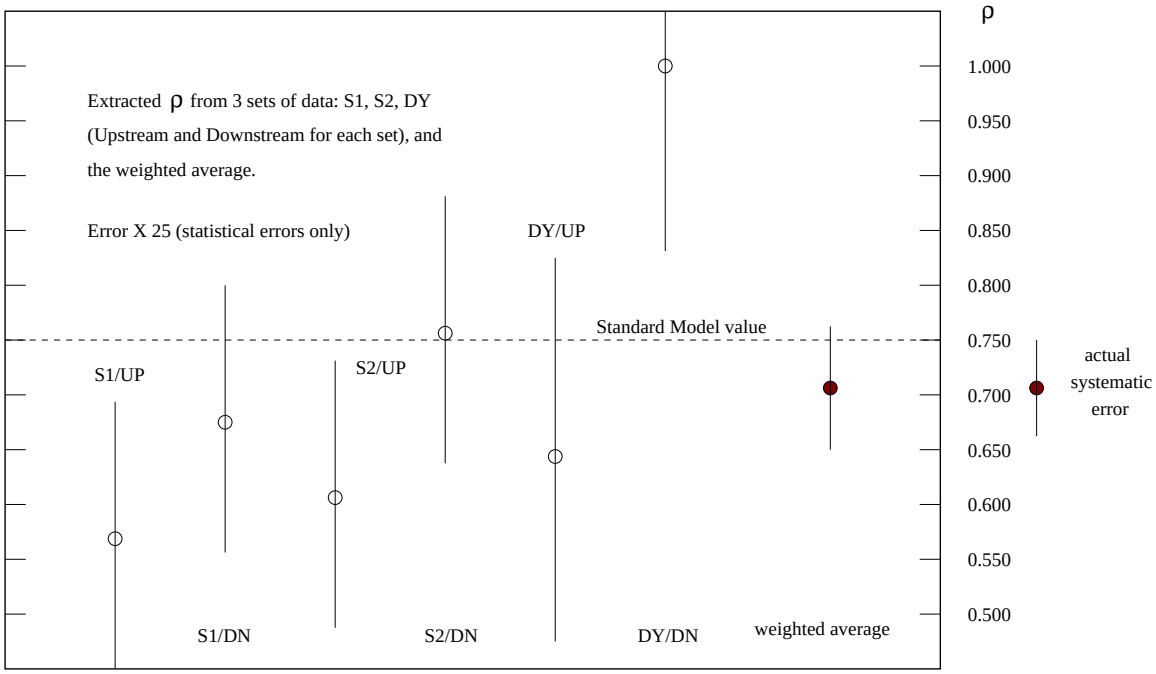

Figure 5.7: The result of RHO measurement.

5.3 Systematic Errors

This experiment is dominated by systematic uncertainties. In Chapter 4 we have demonstrated that the systematic error from chamber wire efficiencies is the dominant contributor. Contribution from scintillators also exceeds the expectation substantially. As stated in previous chapters, the experimental set-up used in this experiment was not designed for ρ measurement but for another experiment (MEGA). Although the overall set-up was well suited for such a measurement, large systematic uncertainties have prevented us from keeping the total error under 0.001.

Because the experimental set-up was dismantled after the MEGA mission was completed in 1995, it was impossible to plan for additional data taking with improved preparation of both hardware and software for RHO measurement. We therefore made every effort trying

to reduce the systematic error by understanding better the relevant experimental elements using existing data. Our final result of systematics study represents our best estimate of those systematic errors. Because it is the same systematic error that is associated with the measurement of ρ for each set of data, the combined value of ρ has the systematic error of 0.045.

5.4 Conclusions

An improved measurement of Michel parameter ρ, both its central value and combined error, provides an excellent test of the V-A characteristics of charged weak interaction described by the Standard Model of particle physics. A deviation of the value from 0.75 set by Standard Model may indicate that, for example, there can be V+A component in charged weak interaction as well. This deviation can then be used to test those theories beyond Standard Model that have included V+A component and set limits on the parameters in those models that are related to non-zero component of V+A. The example we gave in the Introduction for one of those theories is the Manifest-Left-Right-Symmetric Model (MLRSM). A better measurement of ρ can set a more stringent limit on ζ, the mixing angle between W Boson's mass eigenstates and chirality eigenstates in that model, and set a new lower limit on the mass of right-handed W Boson W_R, which does not exist in the current Standard Model due to zero V+A component.

The measurement of RHO experiment, $0.703 \pm 0.002(\mathit{statistical}) \pm 0.045(\mathit{systematic})$ agrees with Standard Model. There is no significant deviation of ρ from 0.75. Unfortunately, the overwhelmingly large systematic error has made it difficult to draw any conclusions that will

challenge the Standard Model.

Vita

Fei-sheng Lee

536 E 79th St.,

New York, NY 10021

Education:

Ph.D., Physics, April, 2001, Department of Physics, Virginia Tech, Blacksburg, VA, U.S.A.

M.S. Computer Science, candidate (1999 - 2000), Computer Science Department, Virginia Tech, Falls Church, VA, U.S.A.

M.S. Physics, December, 1994, Department of Physics, Virginia Tech, Blacksburg, VA, U.S.A.

Graduate study/Engineer: 1989 - 1992, IHEP, Chinese Academy of Sciences, Beijing, China.

B.S. Physics, July 1989, Department of Physics, ECNU, Shanghai, China.

Membership:

Sigma Pi Sigma, Physics Honorary Society, since 1994.